Precision Tuning of Silicon Nanophotonic Devices through Post-Fabrication Processes

Charlton J. Chen

Submitted in partial fulfillment of the
requirements for the degree
of Doctor of Philosophy
in the Graduate School of Arts and Sciences

COLUMBIA UNIVERSITY

2011

ABSTRACT

Precision Tuning of Silicon Nanophotonic Devices through Post-Fabrication Processes

Charlton J. Chen

In recent years, silicon photonics has begun to transition from research to commercialization. Decades of relentless advances in the field of computing have led to fundamental bottlenecks in the design of computers, especially in interconnect bandwidth density. For IBM, silicon photonics has become a potential technological solution for enabling the future of server systems and cutting-edge supercomputers. For Intel, silicon photonics has become a cost-effective solution for supplying the necessary bandwidth needed by future generations of consumer computing products. While the field of silicon photonics is now advancing at a rapid pace there is still a great deal of research to be done.

This thesis investigates ways of improving the performance of fundamental silicon nanophotonic devices through post-fabrication processes. These devices include numerous optical resonator designs as well as slow-light waveguides. Optical resonators are used to confine photons both spatially and temporally. In recent years, there has been much research, both theoretical and experimental, into improving the design of optical resonators. Improving these devices through fabrication processes has generally been less studied. Optical waveguides are used to guide the flow of photons over chip-level distances. Slow-light waveguides have also been studied by many research groups in recent years and can be applied to an increasingly wide-range of applications.

The work can be divided into several parts: Chapter 1 is an introduction to the field of silicon photonics as well as an overview of the fabrication, experimental and computational techniques used throughout this work. Chapters 2, 3 and 4 describe our investigations into the precision tuning of nanophotonic devices using laser-assisted thermal oxidation and atomic layer deposition. Chapters 5 and 6 describe our investigations into improving the sidewall roughness of silicon photonic devices using hydrogen annealing and excimer

laser induced melting. Finally, Chapter 7 describes our investigations into the nonlinear properties of lead chalcogenide nanocrystals.

Table of Contents

1 Introduction **1**

1.1 Introduction 2

1.2 Overview of Thesis 5

1.3 Optical Resonators 6

1.3.1 Microdisks 10

1.3.2 Microrings 10

1.3.3 Asymmetric Resonators 12

1.3.4 Photonic Crystal Ln Cavities 12

1.3.5 Photonic Crystal Heterostructures 13

1.3.6 Photonic Crystal Modegap Cavities 13

1.4 Fabrication 13

1.5 Experimental Setups 16

1.5.1 Lensed Fiber Setup 16

1.5.2 Tapered Fiber Setup 17

1.5.3 Tapered Fiber Pulling 18

1.6 Design Layout 21

1.7 Simulations 21

1.7.1 Frequency Domain Mode Solver - MPB 25

1.7.2 Finite-Difference Time-Domain - MEEP and Fullwave 25

1.7.3 Finite Element - Comsol Multiphysics 26

2 Local Oxidation Resonance Tuning **31**

2.1 Introduction . . . 32
2.2 Local oxidation cavity resonance tuning . . . 33
2.3 Transient effects from oxide surface chemistry . . . 35
2.4 Thermal oxidation . . . 37
2.5 Numerical analysis . . . 38
2.6 Conclusions . . . 39
2.7 Acknowledgements . . . 40

3 Atomic Layer Deposition Resonance Tuning **52**
3.1 Introduction . . . 53
3.2 Design and Fabrication . . . 55
3.3 Experimental Setup . . . 58
3.4 Cavity Resonance Tuning . . . 60
3.5 Selective Tuning . . . 62
3.6 Conclusions . . . 63
3.7 Acknowledgements . . . 64

4 Atomic Layer Deposition Slow-Light Tuning **69**
4.1 Overview . . . 70
4.2 Experimental Setup . . . 70
4.3 Fabrication . . . 74
4.4 Slow Light Tuning . . . 74
4.5 Higher Order Dispersion . . . 77
4.6 Tuning Range . . . 77
4.7 Propagation Losses . . . 78
4.8 Coupling into Slow Light . . . 81
4.9 Conclusions . . . 82
4.10 Acknowledgements . . . 83

5 Hydrogen Annealing and Sidewall Roughness **89**
5.1 Overview . . . 90

5.2 Fabrication . . . 93
5.3 Hydrogen Annealing . . . 93
5.4 Discussion . . . 94
5.5 Conclusions . . . 96
5.6 Acknowledgements . . . 98

6 Excimer Laser and Sidewall Roughness 102

6.1 Overview . . . 103
6.2 Fabrication and Experiment . . . 105
6.3 SEM Image Analysis . . . 107
6.4 Experimental Setup . . . 108
6.5 Excimer Irradiation Results . . . 109
6.6 Analysis and Discussion . . . 111
6.7 Conclusions . . . 115
6.8 Acknowledgements . . . 115

7 Z-scan of Lead Chalcogenide Nanocrystals 120

7.1 Properties of Nanocrystals . . . 121
7.2 Overview of Experiment . . . 122
7.3 The Z-scan Technique . . . 125
7.4 Measurements . . . 127
7.5 Thermal Effects . . . 127
7.6 Discussion . . . 131
7.7 Conclusions . . . 131
7.8 Acknowledgements . . . 132

8 Conclusions 137

Appendices 138

A 140

A.1 List of Publications . . . 140

A.2 List of Conferences 141

List of Figures

1.1 SEM images of different types of silicon optical micro- and nanocavities used in our work. (a) microring (b) microdisk (c) asymmetric resonator (d) photonic crystal defect cavity with 3 missing air-holes (L3 cavity) (e) photonic crystal modegap cavity (f) photonic crystal double-heterostructure cavity . 8

1.2 FDTD simulation of a whispering gallery mode in microdisk. 11

1.3 Photonic crystal structure after buffered oxide etching. 16

1.4 Lensed fiber experimental setup, Inset: Closeup image of lensed fiber made by Nanonics Imaging Ltd. 17

1.5 Tapered fiber test setup. (a) Nitrogen box enclosure of the tapered fiber setup. (b) The tapered fiber is mounted on the holder and used to probe optical devices on the silicon test chip. Positioning is done using precision XYZ translational stages as well as a rotational stage. The fiber and device are imaged using a long working distance objective lens. 19

1.6 Tapered fiber pulling setup. 22

1.7 After pulling the fiber down to an ~ 1 μm diameter taper, it becomes extremely fragile. Here are some common causes of fiber breakage when removing the fiber from the pulling setup. 23

1.8 Improvements to the tapered fiber setup and pulling technique. 23

1.9 Chip layout containing designs from many group members. Such a large chip ($\sim$ 25 x 12 mm) is impractical to fabricate by e-beam lithography due to the long write time. Large numbers of this chip design were fabricated by deep-UV photolithography at IME's research foundry. 24

2.1 (a) Illustration of laser-assisted local thermal oxidation in a silicon double-heterostructure cavity. (b) SEM image of a double-heterostructure cavity. 32

2.2 Experimental setup for local oxidation tuning and cavity resonance measurements. The green laser on the left-hand side is used to assist the thermal oxidation. On the right-hand side are cameras and photodetectors operating at both visible and IR wavelengths. The cameras are used to image the sample. The detectors are used to measure the radiation signal along with the lock-in amplifier and data acquisition system. At the bottom, near-IR light from a tunable laser is coupled onto the device under test by a tapered lensed fiber. 41

2.3 SEM image of a device after local oxidation. The oxidized region is white colored in the SEM because of charging effects in the non-conductive oxide. Note: this is a different device than the one used for cavity measurements in Fig. 2.4. 42

2.4 (a) Experimental results showing the blueshift from tuning using an initial laser power of 19.5 mW (at the device surface). The same device is then further tuned at 22.5 mW. The inset shows measurements of the loaded quality factor as the cavity is tuned. (b) Fitting of the resonant wavelength shift to the square root of oxidation time for incident power of 19.5mW and (c) for 22.5mW. 43

2.5 Radiation measurements at three different tuning increments corresponding to the numbered positions in Fig. 2. Left inset: near-IR radiation pattern for the Fabry-Perot modes on the left. The dotted lines indicate the position of cavity waveguide (upper) and input/output waveguide (lower). Right inset: near-IR radiation pattern for the cavity mode on the right. 44

2.6 Transitory surface chemistry effects. (a) Water molecules absorb onto the oxide surface at room temperature and desorb from the oxide surface at elevated temperatures. (b) During laser irradiation, the cavity experiences a resonance blueshift from oxide dehydration in addition to silicon oxidation. After the cavity cools, water will slowly rehydrate the oxide surface resulting in a gradual redshift. 44

2.7 (a) SEM image of cavity after local oxidation tuning at laser power of 35 mW. The white ring indicates oxide charging effects during SEM imaging. The center region is darker because of slight melting. Inset: Hole melted through the silicon membrane after irradiation at $\sim$ 35 mW for several minutes (different device from the main figure). (b) Local oxidation tuning over a larger wavelength range. The blue region (upper-left) corresponds to the data shown in Fig. 2(a). The upper arrow corresponds to the SEM image in Fig. 1(b). The lower-right arrow corresponds to the SEM image in Fig. 5(a). 45

2.8 (a) Finite-element simulation (COMSOL Multiphysics) of temperature distribution across silicon double-heterostructure cavity during green laser irradiation at 35 mW. (b) Solid lines represent the temperature distribution as a function of distance from the center of the laser beam. Dotted lines represent the intensity profile of the laser beam. (c) Simulation results of local maximum temperature versus laser power. Temperatures range from room temperature to the melting point of silicon. 46

2.9 (a) Calculated electric field E_y profile of high-Q mode supported by double-heterostructure cavity. (b) Calculated wavelength shift of the resonant mode due to local oxidation of the silicon photonic crystal membrane. 46

3.1 Steps in the ALD process involved in depositing a single monolayer of HfO_2. (a) A pulse of $Hg(DEA)_4$ precursor flows into chamber. (b) Unreacted $Hg(DEA)_4$ precursor is flushed out of chamber. (c) A pulse of oxidant flows into the chamber. (d) Unreacted oxidant is flushed out of chamber. 54

3.2 ALD surface quality resulting from different post-fabrication processes. AFM images of ALD surface resulting from (a) initial post-fabrication method and (b) modified post-fabrication method. SEM images of ALD surface resulting from (c) initial post-fabrication method and (d) modified post-fabrication method. 56

3.3 Top-view SEM images of airbridged L5 nanocavity (a) before ALD (b) after 140 ALD cycles of HfO2 (c) angled view before ALD (d) angled view after ALD (e) schematic of PhC cross-section before ALD (f) cross-section after ALD 57

3.4 Test setup for taking radiation measurements from on-chip PhC nanocavity devices. 59

3.5 (a) FDTD calculated electric field E_y profile of the high-Q mode supported in the L5 nanocavity. (b) The tuned resonant wavelength scales linearly with the number of deposition step for all three L5 cavities under investigation. Inset: 3D FDTD calculated wavelength shift ($\Delta\lambda$) for increasing thicknesses (Δt) of HfO_2 deposited for all three cavities studied. (c) The wavelength increment $\delta\lambda$ for each deposition step. (d) The variation of the quality factor Q with the number of deposition steps for all three L5 cavities. (e) Measured cavity resonances after each deposition step (”1” to ”7” in legend; ”0” is unperturbed) for L5 cavity with S_1=0.02a. 61

3.6 Selective ALD (a) process steps (b) selective resonance tuning of a single high-Q cavity. Inset: the left cavity is tuned while the right cavity is unperturbed 63

3.7 SEM image of L3 nanocavity coated with PMMA. A 250 nm diameter hole has been patterned in the center of the cavity for selective ALD tuning. . . 64

4.1 Test setup for ALD dispersion tuning studies. Polarization of light from the laser source (supercontinuum / tunable laser) is controlled by a polarizer and waveplate and coupled to the photonic crystal chip with a polarization maintaining lensed fiber. The output light is sent to a photodetector or optical spectrum analyzer. The chip is imaged with a 40X objective lens and IR camera. 71

4.2 SEM image of (a) PhC waveguide and strip waveguide interface (b) MZI structure with PhC waveguide on upper section and strip waveguide on lower section. (c) PhC before deposition (upper image) and after 160 ALD layers of HfO_2. 72

4.3 Band structures calculated using plane-wave expansion method. Solid-lines correspond to no HfO_2 deposition. Dotted-lines and dashed-lines correspond to 80 and 160 atomic layers of HfO_2 deposition, respectively. (a) Projected band diagram for TE-like W0.9 waveguide modes (b) Corresponding TM band diagram. Note that the vertical and horizontal ranges are different than in (a). 73

4.4 (a) TE transmission measurements for different ALD tuning steps. The different colors denote the various ALD layers. (b) Corresponding TM transmission measurements. 76

4.5 (a) Group-index measurements from MZI devices. The number of atomic layers deposited is indicated by the color of the circles. Refer to the color code described in Figure 3(a). The solid lines are provided for clarity. Inset: measured slow-light (SL) mode onset (red circles) and numerical simulations (blue dashed line). (b and c) Measured group-velocity dispersion and third-order dispersion for the different ALD tuning steps. 78

4.6 TE transmission measurements before HfO_2 ALD and after deposition in increments of 150 atomic layers. The slow-light mode onset edge is tuned across the C-band and also across part of the L-band. 79

4.7 (a) Average effective area of PhC waveguide slow light modes with ALD deposition at group-index of 50 (red line) and group-index of 6 (blue line). Calculated modes of W0.9 waveguide at (b) group-index of 50 (c) group-index of 6. The blue dotted line indicates where the cross-sections are taken perpendicular to the Y-Z plane. The resulting Y-X cross-sections before and after 160 atomic layers of HfO_2 have been deposited are shown below the Y-Z figures. 80

4.8 (a) SEM images of different PhC terminations at the interface between the PhC lattice and strip waveguide. From left to right: $\tau = 0$, $\tau = 0.5$ and $\tau = 0.75$. (b) Experimentally determined coupling coefficients as a function of group index (log-log scale) before ALD. Points correspond to the following surface terminations: $\tau = 0$ (red), $\tau = 0.5$ (green), and $\tau = 0.75$ (blue). c) Coupling coefficients after 160 atomic layers of HfO_2 deposited. 82

5.1 Silica microtoroid fabricated by laser induced thermal reflow. The pedestal is single-crystal silicon. 91

5.2 SEM images of silicon microdisk surface and edge; (a) before hydrogen annealing (b) after hydrogen annealing. Scale bar in both images represents 500 nm. 95

5.3 SEM images of silicon surface after hydrogen annealing. Pitting, dislocations and carbon nanotube contamination can be seen. The region in (a) enclosed by the dotted line is magnified and shown in (b). The scale bar in (a) is 10 μm and in (b) is 1 μm. 97

6.1 Comparison between the coupling depth of the green laser and excimer laser in SOI substrates. Not drawn to scale. The top silicon layer is 250 nm, the oxide layer is 3 μm, and the bulk silicon substrate is $\sim$ 750 μm. 104

6.2 Dark-field optical microscope image of highly non-uniform silicon surface morphology after excimer exposure if BOE dip prior to exposure is not performed. 105

6.3 SEM image analysis of a line edge prior to excimer exposure. The RMS roughness is 2.8 nm. 108

6.4 (a) Dark-field optical microscope image of excimer irradiated ($\sim$ 300 mJ/cm^2) and unirradiated regions. The irradiated region is brighter, indicating increased light scattering and roughness. (b) Optical microscope image of tapered fiber to microdisk coupling for optical measurements. 110

6.5 SEM image of silicon microdisk after excimer laser irradiation. 111

6.6 SEM image of edge of silicon edge region that has been half excimer laser irradiated (right) with an energy density of 1200 mJ/cm^2. The silicon is 250 nm thick. Note that in this case the oxide underneath has not been removed. 111

6.7 SEM image of edge of silicon edge region that has been half excimer laser irradiated (left) with an energy density of 240 mJ/cm^2. The silicon is 250 nm thick. The oxide underneath has been isotropically etched by several microns. 112

6.8 SEM image of undercut silicon edge region that has been excimer laser irradiated at an energy density of 370 mJ/cm^2. 112

6.9 SEM image of undercut silicon edge region that has been excimer laser irradiated at an energy density of 460 mJ/cm^2. 113

6.10 (a) SEM image of 15 μm diameter silicon microring on top of oxide. (b) Transmission measurements from 15 μm diameter silicon microring after excimer irradiation. 114

7.1 Diagram of the Z-scan test setup used in this experiment. 125

7.2 (a) Closed aperture Z-scans of colloidal PbS nanocrystal solution. (b) Open aperture z-scan of colloidal PbS nanocrystal solution at 1240 nm. (c) Time-resolved photoluminescence used to determine the $\sim$ 930 ns radiative lifetime (T_1) for the colloidal PbS nanocrystals. 128

7.3 Measured linear absorption and nonlinear refractive indices for the colloidal PbS nanocrystals studied. 130

7.4 Measured linear absorption and nonlinear refractive indices for the colloidal PbSe nanocrystals studied. 130

List of Tables

1.1 Silicon photonic resonators 9

2.1 Passive post-fabrication photonic-crystal cavity tuning techniques. 34

5.1 Thermal reflow on amorphous and crystalline optical materials 92

7.1 Properties of lead chalcogenide nanocrystals investigated. 124

List of Acronyms

AFM	atomic force microscope
ALD	atomic layer deposition
ASE	amplified spontaneous emission
BNL	Brookhaven National Laboratory in Upton, NY
BOE	buffered oxide etch
CFN	Center for Functional Nanomaterials at BNL
CMOS	complementary metal-oxide-semiconductor technology
CNF	Cornell Nanofabrication Facility in Ithaca, NY
EIT	electromagnetically-induced transparency
FEM	finite-element method
FOM	figure-of-merit
FDTD	finite-element time-domain method
GVD	group-velocity dispersion
HF	hydrofluoric acid
HMDS	hexamethylsilazane, an adhesion promoter for photoresist
IME	Institute of Microelectronics in Singapore
IPA	isopropyl alcohol
IR	infrared
L3	photonic crystal defect cavity with three air-holes removed
NIR	near-infrared
NSEC	Nanoscale Science and Engineering Center
MEEP	FDTD software package from MIT
MIT	Massachusetts Institute of Technology

MPB	MIT Photonic Bands software package
MRSEC	Materials Research Science and Engineering
MZI	Mach-Zehnder interferometer
NIST	National Institute of Standards and Technology
NPGS	Nabity Pattern Generating System
OSA	optical spectrum analyzer
PhC	photonic crystal
PMMA	polymethyl methacrylate electron-beam resist
PWE	plane wave expansion method
Q	quality factor (optical)
QED	quantum electrodynamics
SEM	scanning electron microscope
SMF	single-mode fiber
SOI	silicon-on-insulator
TE	transverse-electric polarization
TM	transverse-magnetic polarization
TIR	total internal reflection
TOD	third-order dispersion
UV	ultraviolet
WGM	whispering-gallery mode

Acknowledgments

I would like to sincerely thank my advisor, Chee Wei Wong for all of his encouragement and support over the past few years. Endowed with enormous ambition, ability and aggressiveness he has worked tirelessly to recruit the best and brightest and build a research group engaged in a wide range of photonics research. Working with Chee Wei has not come without hardships. The bar is always set high and the challenges are always more difficult then they first appear. But hard work and perseverance are requisite traits shared by all Ph.D. students. As Benjamin Franklin once said: there are no gains without pains.

I would also like to thank the group members who have contributed to this work. I thank Chad Husko for his gifted ability to teach as well as his many meaningful contributions despite a relentlessly hectic schedule. I thank James McMillan for his brilliant insights and technical genius. I thank Jiangjun Zheng for his endless scientific curiosity, which has often led me to ask questions I would not have otherwise. I also thank Xiaodong Yang for his sharp intellect and attention to fine details. Other group members who have contributed to this work include Ranojoy Bose, Jie Gao, Kai Liu, Felice Gesuele, Mehmet Aras and Tingyi Gu.

Prior to joining the Optical Nanostructures Laboratory, my Master's research, in the field of fabrication and surface chemistry of nanoscale bioarrays, was in the group of James Hone. I am very grateful for his hands-on involvement in my research. In addition, I would also like to sincerely thank Shalom Wind for sharing his deep knowledge, experience and insights. Lastly, I thank Oksana Cherniavskaya for working tirelessly to obtain the experimental results.

I would also like to thank the professors of the Materials Science Department at Columbia where I took many classes and worked as a teaching assistant. My thanks to James Im, Siu-Wai Chan, Daniel Beshers, Paul Duby, William Bailey, Cevdet Noyan, Stephen O'Brien

and Chris Marianetti.

This work would not have been possible without the help of a large number of professors, researchers, students, technicians, machinists, and administrators, all of whom deserve credit and thanks. Thank you to: Richard Osgood, Ken Shepard, John Kymissis, Irving Herman, Michael Sheetz, Dim-Lee Kwong, Chris Murray, Lawrence Yao, Lan Yang, Zhisheng Shi, Solomon Assefa, Yuri Vlasov, Kartik Srinivasan, Aaron Stein, Ming Lu, Jerry Dadap, Jeffrey Urban, Limin Huang, Pascal Heider, Yikang Deng, Alexander Limanov, Paul van der Wilt, Inanc Meric, Joan Raitano, Fanghai Zhao, Yun-Feng Xiao, Changgu Lee, Jeffrey Driscoll, Rob Ilic, Mingbin Yu, Guo-Qiang Lo, Gen Satoh, Yuan Zhang, Walter Khan, Robert Stark, Richard Harniman, Geoff Goold, Linus Fetter, Montserrat Fernandez-Pinkley, Xiomara Perez-Betances, Chad Gurley, Wesley Hattan, Feben Getachew, Clarissa Marino and Sandra Morris. Undoubtedly, there are others I have missed. Thank you for all of your help. Finally, I would like to thank Yikang Deng and Jerry Dadap once again for their generous and meaningful contributions.

Dedicated to my parents, James and Therese, for their infinite and unconditional support.

Chapter 1

Introduction

1.1 Introduction

In 2009, the Royal Swedish Academy of Sciences awarded the the Nobel Prize in Physics to Charles Kao for the discovery of low-loss optical glass fiber for transmitting information using light [1]. In the decades following the discovery in 1966, fiber optics became the standard medium for transmitting ever larger amounts of information over long distances. At first, fiber optics was used to carry primarily voice data by telecommunications companies. But the rise of the internet in the 1990s, resulted in an enormous increase in both the diversity and volume of digital data. Fiber optic communications became increasingly important for ever shorter distance applications, which were traditionally served by copper wire and coaxial cable. Optical communications was able to deliver much higher bandwidths at lower costs, lower powers and with lower heat generation. The progression of length scales spanned from ultra-long transoceanic distances to much shorter inter-city distances. Later, distances within metropolitan areas also became economically favorable for fiber-optics. Each distance range required new technologies, often smaller in size, lower in cost and larger in volume [2]. But the relentless progression of photonics to smaller length scales did not stop at what is commonly referred to as the "last mile" with the realization of fiber-to-the-home. This is where silicon photonics entered the picture with the promise of reaching for "the last micron" and perhaps even "the last nanometer".

The field of silicon photonics aims to reuse the same material which has been so successful in the microelectronics industry. But instead of being used to manipulate the flow of electrons, here it is used to manipulate the flow of photons at the chip level. The band gap of silicon is 1.11 eV, therefore near-infrared light with wavelengths above $\sim$ 1200 nm will not experience band-to-band absorption and silicon will be transparent. This makes silicon compatible with fiber optics which typically operate at wavelengths of 1.3 μm and 1.55 μm which correspond to the attenuation minimums in silica glass. Work began in this field in the mid-1980s by researchers such as Richard Soref at the Air Force Research Laboratory. But only in the past decade has research in this field really taken off due to the enormous increase in bandwidth demand created by the internet revolution of the previous decade. Additionally, the 130 nm CMOS semiconductor process node was reached around the year 2000. At that technology node, silicon photonic structures start becoming feasible using photolithography.

The driving force behind silicon photonics has been industrial economics. Silicon is a widely available material, comprising 26% of the earth's crust. Forty years of continuous investment in silicon processing technology for the microelectronics industry and more recently the solar power industry has made silicon one of the most extensively studied materials. It has also resulted in a technologically advanced industry that can produce very high quality silicon wafers and process those wafers with high fabrication yields and economies of scale. No other material is comparable from an economics standpoint. Especially after integrating low-cost photonics alongside low-cost electronics on the same chip.

But from a technical standpoint, the feasibility of using silicon as the platform for large-scale integrated photonics has not been so obvious. As recent as a few year ago, the future of silicon photonics was highly uncertain and many skeptics doubted work in this area would ever escape the confines of research laboratories and lead to viable commercial technologies [3].

Single-crystal silicon is a semiconductor with an indirect minimum-energy bandgap and is therefore inefficient at emitting light. This makes it a seemingly unsuitable material for lasers. But in 2005, researchers at Intel demonstrated the first all silicon laser by utilizing the Raman effect for optical gain [4]. Another shortcoming of single-crystal silicon is its centrosymmetric crystal structure which does not allow for the Pockels effect, a linear electro-optic effect used for building optical modulators in materials such as lithium niobate. But once again, the technical hurdle was overcome by using a clever alternative approach. A group at Cornell University demonstrated a compact silicon electro-optic modulator operating on the Kerr effect, a quadratic electro-optic effect which is much weaker than the Pockels effect. The refractive index change was enhanced using a ring resonator [5].

Silicon is a good material for photodetectors operating at visible wavelengths but it is no longer effective at wavelengths beyond ~ 1200 nm as the silicon bandgap is too large. To overcome this problem, researchers have looked to depositing layers of silicon germanium. Another approach is to utilize two-photon absorption, where the combined energy of two photons is enough to overcome the energy bandgap. But such detectors operate at low speeds [6].

Even though silicon is transparent at wavelengths of the telecommunications wavelengths of 1.3 μm and 1.55 μm, propagation losses in waveguides due are still quite high in comparison to fiber optics. For example silicon waveguides have been reported with losses of 0.3 dB/cm compared to 0.15 dB/km for optical fiber losses [7, 8]. While the 5 orders of magnitude difference seems formidable, silicon photonics operates at the chip scale rather than over ultra-long distances. Hence these losses might be acceptable for simple photonic devices but lower losses will likely be needed as photonic circuit complexity increases. The issues discussed above are just some of the problems faced as researchers worldwide have been racing to "siliconize" photonics [1].

Recently, the outlook for silicon photonics has become clearer as start-up companies focusing on silicon photonics have emerged from stealth-mode and Intel corporation, the world's largest supplier of silicon products, is currently beginning production of a silicon photonics product [9]. Intel's Light Peak continues the trend to shorter and shorter optical transmission distances, this time connecting board-to-board. Light Peak is a universal high-speed data cable (50 gigabits per second) that is intended to replace the USB and monitor cables on computers and consumer electronic devices. Each of these cables contains two silicon photonic chips for electrical-to-optical signal conversion. This is an example of how silicon photonics is now beginning to enable smaller form factors and lower costs in order to address a mass consumer market where previously conventional photonics had been too expensive.

In the years to come, photonics will likely continue it's trend towards shorter distance applications. Recent data has shown the number of components on integrated silicon photonic chips has been steadily increasing since 2002 [10]. This trend appears similar to Moore's Law for integrated semiconductor components where the number of components doubles every 18 months. Photonics will no longer be confined to the function of data transmission but also play a role in data processing. Recent advances in nonlinear optics

---

[1] Many of the largest technology corporations today have active research and development programs in silicon photonics. These include Intel, IBM, NTT, HP and Oracle (Sun Microsystems), BAE Systems. In addition many smaller companies and startups are also very active, including Luxtera, Avago, Lightwire, Kotura.

in silicon has made this all the more likely [11].

> *"A CMOS transistor is not known to be a particularly high-performance transistor, but the ability to manufacture large numbers of them integrated on a single substrate has undoubtedly changed the course of technology. Similarly, most silicon photonics optical devices don't perform as well as they might in another material system, but the ability to integrate them in large numbers alongside CMOS circuitry holds great promise."*
>
> \- Cary Gunn, Luxtera

1.2 Overview of Thesis

This thesis describes our investigations into new fabrication processes with the potential of improving the performance of silicon photonic devices. The key issues addressed are cavity resonance tuning, slow-light tuning, surface roughness modification and nonlinear properties. The devices we focus on are optical resonators and photonic crystal waveguides.

In Chapter 2 we investigate using laser-assisted local oxidation to finely tune the post-fabrication resonance of ultra-high Q nanocavities. Chapter 3 continues the work with resonance tuning. Atomic layer deposition is used to globally compensate for wafer- or chip-wide fabrication errors. The same monolayer deposition technique is then applied to the tuning of slow-light waveguides in Chapter 4. The next two chapters discuss our investigations into improving sidewall roughness. Chapter 5 deals with our studies of hydrogen annealing, a wafer-wide technique for achieving atomic-scale roughness as well as for fabricating rounded geometries. Chapter 6 discusses our studies of excimer laser for sidewall roughness modification. This technique can be used both locally as well as globally. The final chapter discusses our investigations into the nonlinear properties of chalcogenide nanocrystals with the intention of incorporating these materials into silicon photonic devices. A number of other investigations were also pursued but not discussed in this thesis due to the nature of the projects and the relevance of the results to this thesis

In the following sections of this introductory chapter basic concepts of nanophotonic devices are discussed. This is followed by discussions on the general design and fabrication tools we employ, including numerical simulations. Finally optical testing and analysis tools are examined. The technical improvements we have made in each of these fields are also discussed.

1.3 Optical Resonators

Optical resonators or cavities are used to confine light both spatially and temporally. They are fundamentally important to a large range of devices such as lasers, modulators, filters, optical switches and optical memory. Unlike electrons, photons have no rest mass and cannot be confined by electric and magnetic fields. Instead photons are trapped in optical cavities by multiple reflections which result in standing waves. These resonant frequencies are also known as the cavity modes. But over time, the number of photons trapped in these cavities will decrease. Optical losses can be attributed to many mechanisms including material absorption, scattering losses and evanescent field decay.

A measure of the temporal confinement of light in an optical resonator is the quality factor or Q. Eqn. 1.1 describes the Q factor as the product of the resonant frequency (ω) and the photon lifetime (τ_{ph}) in a cavity. The inverse of the Q factor can be interpreted as a measure of the lossiness of a cavity as seen in Eqn. 1.2 where Q is described by the number of cycles needed for all the light stored in an optical cavity to escape:

$$Q = \omega \tau_{ph} \tag{1.1}$$

$$Q = 2\pi \left(\frac{\text{stored energy}}{\text{energy loss per cycle}} \right) \tag{1.2}$$

Yet another way to think about Q is in terms of the spectral width of the resonance. In

Eqn. 3, the resonance wavelength is λ and the full-width half-maximum (FWHM) of the resonance is $\Delta\lambda$:

$$Q = \frac{\lambda}{\Delta\lambda} \tag{1.3}$$

A measure of the spatial confinement of light in an optical resonator is the modal volume V_m. The modal volume can be calculated from the distribution of the electric field (E) and index of refraction (n) using Eqn. 1.4. There are different definitions for modal volume under different conditions, for example the definition for modal volume in the presence of nonlinear effects will be different. The values for E(x,y,z) and n(x,y,z) can be calculated using numerical simulations which will be discussed later in this chapter.

$$V_m = \frac{\int n^2 |E|^2 \,\mathrm{d}v}{(|nE|_{max})^2} \tag{1.4}$$

The temporal confinement (Q) and spatial confinement (V_m) are often combined into the ratio: Q/V_m. A high Q/V_m means that light is trapped in a very small volume for a long period of time. The longer light bounces around in this cavity, the higher the probability that the photons will interact with the material of the cavity. Hence, Q/V_m is associated with enhanced light-matter interaction and this is important for nonlinear effects in photonic crystal cavities [12]. High Q/V_m can also be exploited to make devices smaller. For example, traditionally, silicon optical modulators are quite large and unsuitable for integrated silicon photonics. But by utilizing high Q/V_m, micrometer-scale silicon modulators have been realized [5].

In recent years, a large number of different silicon-on-insulator (SOI) based optical resonator designs have been proposed and investigated. Table 1.1 lists the silicon micro- and nanocavities that we have used in this this current work, along with the the notable characteristics of each of these designs.

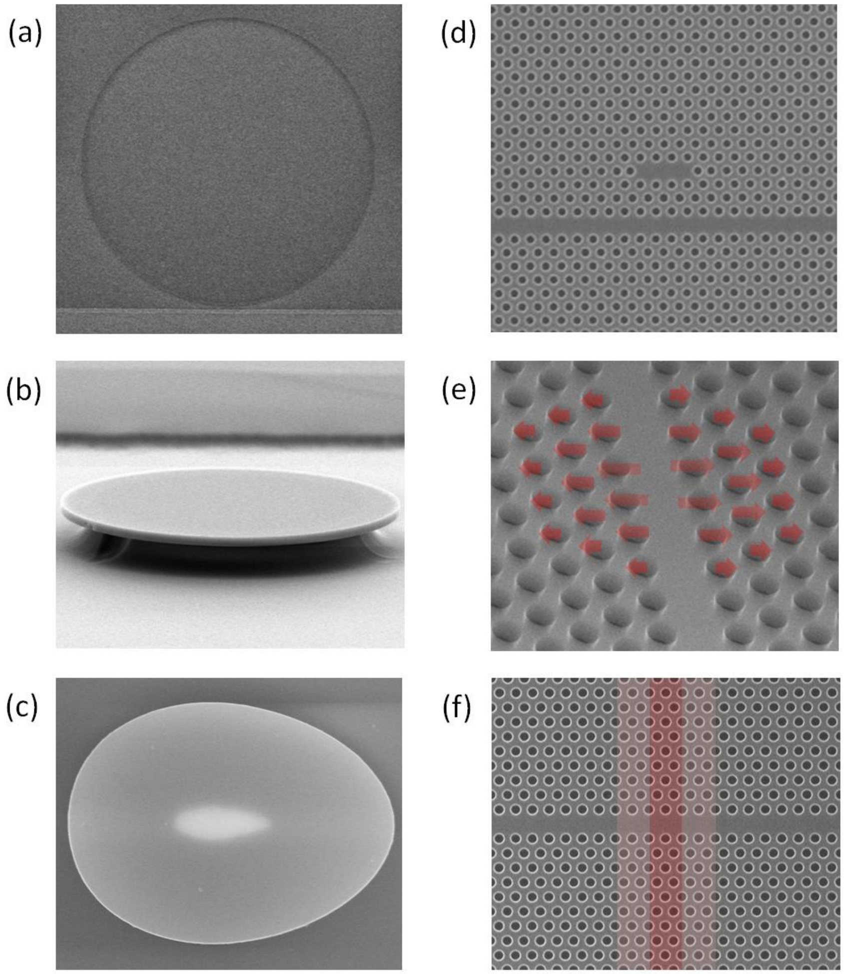

Figure 1.1: SEM images of different types of silicon optical micro- and nanocavities used in our work. (a) microring (b) microdisk (c) asymmetric resonator (d) photonic crystal defect cavity with 3 missing air-holes (L3 cavity) (e) photonic crystal modegap cavity (f) photonic crystal double-heterostructure cavity

Table 1.1: Silicon photonic resonators

Resonator	**Q factor**	**Modal Volume**	**Refs.**
Microring ($r = 20\ \mu m$)	10^5		[13]
Microring ($r = 1.5\ \mu m$)	10^4	$12\ (\lambda/n_{Si})^3$	[14]
Microdisk ($r = 20\ \mu m$)	10^6	$65\ (\lambda/n_{Si})^3$	[15, 16]
Microdisk ($r = 1.5\ \mu m$)	10^5	$6\ (\lambda/n_{Si})^3$	[16]
Asymmetric Resonator	10^4	$10\ (\lambda/n_{Si})^3$	[17, 18]
PhC Ln	10^5	$0.7\ (\lambda/n_{Si})^3$	[19, 20]
PhC Modegap	10^6	$1.5\ (\lambda/n_{Si})^3$	[21]
PhC Heterostructure	10^6	$1.5\ (\lambda/n_{Si})^3$	[22, 23]

1.3.1 Microdisks

Optical microdisks made of semiconductor material were first studied by McCall at Bell Laboratories in the early 90's [24]. Unlike Fabry-Perot cavities which have standing wave modes, microdisks belong to a class of traveling wave resonators known as whispering-gallery mode (WGM) resonators. The first few cavity designs in Table 1.1 (microdisks, microrings and asymmetric resonators) have WGMs. Whereas the later designs are all photonic crystal based nanocavities with standing-wave modes.

Whispering-gallery is an analogy to the dome-like architectural structures where sounds as faint as a whisper can travel unusually long distances because the acoustic wave is guided along the smooth surface of the dome with little attenuation [2]. Fig. 1.1 (b) shows an SEM image of a silicon microdisk. Fig. 1.2 shows a microdisk WGM as calculated by the 2-D finite-difference time-domain method. In plane, the optical mode travels along the disk periphery due to total internal reflection (TIR). TIR is also responsible for confining the mode in the out-of-plane direction.

McCall's WGM microdisk was made of InP/InGaAsP which, unlike silicon, is an active gain material. He was able to optically pump the microdisk and achieve ultralow threshold lasing at telecom wavelengths of 1.3 and 1.5 μm [24]. More recently a number of groups have incorporated gain material onto silicon microdisks to enable lasing [25, 26]. Because of their simple design and ease of fabrication, microdisks have also been used in numerous photonic studies in recent years, including self-induced optical modulation [27] and cavity quantum electrodynamics [28].

1.3.2 Microrings

The microring consists of a narrow strip waveguide in an enclosed circular pattern as shown in Fig. 1.1(a). A variation of this design is the racetrack resonator which is a microring elongated in one direction. Silicon microrings are generally fabricated on SOI substrates without removing the underlying oxide. This is one reason why the Q of microrings is lower than the Q of microdisks as seen in Table 1.1. The experimentally measured Q of

---

[2] One such whispering gallery can be found adjacent to the Oyster Bar at Grand Central Station in New York City where it is occasionally used by mischievous individuals to spook unsuspecting passers by.

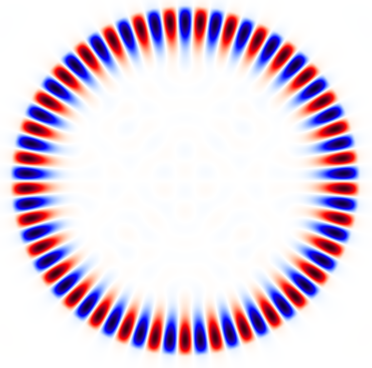

Figure 1.2: FDTD simulation of a whispering gallery mode in microdisk.

a 20 μm radius microdisk is $\sim 10^6$ whereas the experimentally measured Q of a 20 μm radius microring is $\sim 10^5$. A second reason why the Q of the microring is lower is because it has two sidewall surfaces, outer and inner, whereas the microdisk has only one sidewall surface. In silicon photonics, sidewall roughness is more problematic than surface roughness. Wafers are chemically mechanically polished and have very smooth top surfaces. During fabrication, the silicon is dry etched and this process introduces significant sidewall. This is a topic we will explore in more detail later in this thesis.

An important attribute of ring resonators is the free spectral range (FSR), also known as the mode spacing. It is defined in Eqn. 1.5. Conversely it can also be defined as a frequency spacing, Eqn. 1.6

$$\delta\lambda_{FSR} = \frac{\lambda^2}{n_{eff}L} \tag{1.5}$$

$$\delta\nu_{FSR} = \frac{c}{n_{eff}L} \tag{1.6}$$

Where λ is the wavelength, ν is the frequency, n_{eff} is the effective index and L is the round-trip distance of the cavity, i.e. $L = 2\pi R$ for microrings and microdisks.

1.3.3 Asymmetric Resonators

Due to radial symmetry, microdisk lasers do not have a directional preference for light emission. The lack of directionality is also the reason evanescent waves must be used to couple to these cavities. Recently, there has been interest in cavity geometries that break rotational symmetry and allow directional emission [17, 29, 18]. This was the motivation for our collaboration with Pascal Heider, a mathematician and visiting scholar from the University of Cologne in Germany. Pascal had previously been studying asymmetrically shaped resonators from a purely theoretical perspective.

My role in the collaboration was to take his theoretically derived designs and turn them into actual silicon photonic devices for the purpose of experimental investigations. The fabrication was performed using e-beam lithography at Columbia University. An SEM image of this egg-shaped cavity is shown in Fig. 1.1 (c). The optical experiments were done by Jie Gao and Xiaodong Yang [17] at wavelengths ranging from 1530 to 1560 nm.

1.3.4 Photonic Crystal Ln Cavities

The SEM image in Fig. 1.1 (d) shows a PhC defect cavity with 3 missing air-holes. Such a cavity is commonly referred to as a L3 cavity. In our work, we have also used many L5 cavities.

Table 1.1 shows that as microdisks and microrings become smaller, their Q factor will also drop. This can be attributed to increased bending losses. This phenomenon limits the maximum Q/V$_m$ ratios that WGM resonators can achieve. The quest for ever higher Q/V$_m$ has lead researchers to photonic crystal (PhC) nanocavities. In the mid-2000's a number of breakthroughs came from researchers in Japan. PhC cavities have generated much interest because high Q/V$_m$ also comes with a decrease in device dimensions and is therefore favorable for higher component integration density.

PhCs were first proposed by Eli Yablonovitch and Sanjeev John in 1987. Initial studies were conducted at microwave wavelength scales. Only more recently has the field moved to optical wavelengths and semiconductor materials such as silicon. In planar PhC cavities, light is confined in-plane by the photonic bandgap of the surrounding periodic dielectric structures, i.e. by Bragg reflections. Light is confined out-of-plane by total internal reflection or Snell's law.

In 2003, the group of Susumu Noda at Kyoto University discovered it was possible to increase the Q of a PhC defect cavity by a factor of 20 to 100,000 by carefully shifting the nearby air-holes. Additionally, this did not affect the modal volume of the cavity [19]. The fine tuning increased the magnitude of the Bragg reflection by creating a mode profile closer in shape to a gaussian function. As a result, the 2D fourier transform of the spectrum showed less k-vector components inside the leaky region after this air-hole tuning.

1.3.5 Photonic Crystal Heterostructures

In 2005, Noda's group once again made a leap foward by achieving experimental Q's of 600,000 using a double-heterostructure design [22]. Theoretical calculations of these cavities showed Q's of over 20,000,000. Through improved fabrication the experimentally achievable Q was soon increased by over 60% to 1,000,000 [23]. An SEM image of a PhC double heterostructure cavity is shown in Fig. 1.1 (f).

1.3.6 Photonic Crystal Modegap Cavities

In 2006, the group of Masaya Notomi at NTT Research Laboratories outside of Tokyo reported a cavity design based on mode-gap confinement that achieved Q's of ~800,000. The cavity had an ultrasmall modal volume of $1.5(\lambda/n_{Si})^3$ [21]. The theoretical Q for these cavities was as high as 7×10^7 as calculated by numerical simulations. An SEM image of a PhC modegap cavity we have used is shown in Fig. 1.1 (e).

1.4 Fabrication

All of the devices used in our studies (shown in Fig. 1.1) have been fabricated on silicon-on-insulator wafers. Our wafers are obtained from wafer manufacturer Soitec Inc. of France. The SOI wafers are manufactured using wafer bonding followed by an ion implantation assisted cleaving process to remove most of the top wafer. The wafer then goes through annealing and chemical mechanical polishing (CMP). Wafers generally have a p-type doping concentration of 10^{16} cm^{-3}.

SOI is a standard platform used in CMOS fabrication because it allows isolation of transitor devices and improved electrical performance but at increased wafer costs. SOI is used in the field of silicon photonics because of the large refractive index difference between Si to SiO_2, 3.5 to 1.5 respectively. The high index contrast allows for better confinement of optical modes. This is advantageous for compact devices and highly integrated systems. Additionally, the oxide beneath silicon structures can be locally removed to further improve the optical confinement. This is done through resist patterning and oxide etching, resulting in suspended membranes with air cladding both above and below.

Despite SOI's widespread use, the exact specifications needed for our wafers are generally only used by the silicon photonics community. Hence, such wafers can sometimes be difficult to obtain. Our device layer consists of 250 nm of high quality (100) single-crystal silicon. Beneath this is a thermal oxide layer, 2-3 μm in thickness. The bulk substrate is also single-crystal silicon, with thicknesses ranging from 500 μm to 750 μm. Larger wafers (300 mm) have thicknesses that are on the higher end of this range. This is necessary to ensure wafer planarity. But thinner substrates are favorable because they can be more easily cleaved. This is important for achieving good edge facets for coupling to on-chip waveguides. To get a thinner substrate, CMP can be used on the back surface of the wafer after device fabrication.

Most research groups fabricate their photonic devices using electron-beam (e-beam) lithography because of its high resolution and direct-writing capability. Our group has been using a combination of e-beam lithography and high-resolution optical lithography. During my time at Columbia, our facilities did not have a high-end e-beam lithography system. Our resources were limited to a Scanning Electron Microscope (SEM) modified with a JC Nabity Lithography System for e-beam writing. The system was limited to a writing field of $\sim$ 1 mm. Lacking interferometric stages, stitching error between writing fields was several microns, unacceptably large. Because of this, it was impractical to write structures requiring waveguides. This was one of our motivations for pursuing deep- UV optical lithography as an alternative fabrication method.

From a manufacturing point of view, optical lithography is essential to the future of silicon photonics. As a researcher, optical lithography can have both advantages and disadvantages. The advantage is an extremely large number of test structures can be printed quickly as opposed to the very slow raster-scanning speeds of the e-beam lithography. The disadvantages include increased turn-around time for mask making and fabrication runs. Optical lithography also has lower resolution, limited by diffraction effects. This can be problematic for photonic devices with many nanoscale features.

Some of the photonic chips used in my work were designed and fabricated by the Silicon Integrated Nanophotonics Group at IBM Research in Yorktown Heights, New York. This was done using e-beam lithography in their research fab. More recently, the Center for Functional Nanomaterials (CFN) at Brookhaven National Laboratory (BNL) installed a JEOL JBX-6300FS electron beam lithography system. The facilities are within convenient travel distance from New York City and our group had prior collaborations with Aaron Stein, CFN's resident e-beam expert. I was able to quickly receive training on the tool and have used it to fabricate a number of high-quality devices.

After fabrication most of our devices were airbridged, i.e. the oxide underneath was removed. This was always done using the cleanroom at Columbia University. The airbridging process involves a number of fabrication steps. First the chip is cleaned in acetone, isopropanol and water along with ultrasonic agitation. Next the chip is dehydrated on a hotplate at 180 °C for 5 minutes. Then the chip is spin-coated with HMDS, an adhesion promoter. A thick photoresist is spin-coated over the chip and soft-baked. A contact aligner is used to pattern transfer a series of large low-resolution windows around the devices where the oxide is to be removed. The resist is then developed and hard-baked. The resulting resist mask is used to prevent the waveguides on the chip from lifting off in the subsequent buffered oxide etching (BOE). After BOE, the chip is rinsed in water and then put into either Nanostrip or Piranha to remove the resist mask. The chip is then rinsed again in water and transferred to acetone to remove any residual organics. Finally, the chip is transferred to hot methanol at 60-80 °C before being removed into air. Hot methanol has low surface tension when evaporating and is less likely to cause waveguide collapse during drying. An alternative to hot methanol is supercritical drying. But the process is more time consuming and I found it unnecessary for my particular devices. After all these steps have been performed, the chip is ready for SEM imaging (Fig. 1.3) and optical testing.

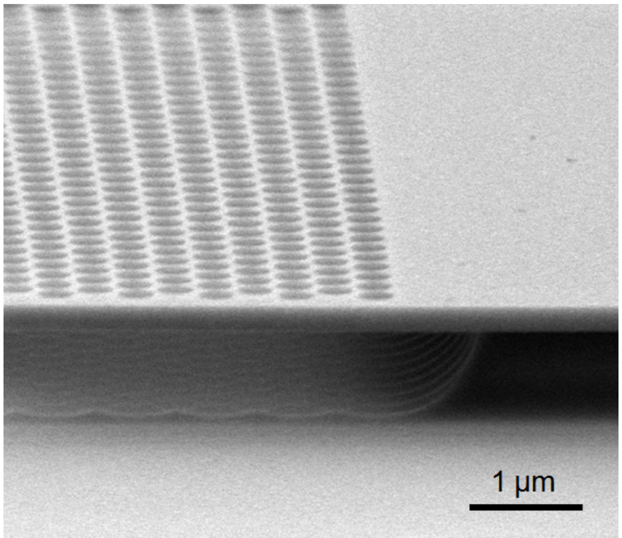

Figure 1.3: Photonic crystal structure after buffered oxide etching.

1.5 Experimental Setups

In order to perform the optical measurements in this thesis, I built several different experimental test setups. For chip based measurements, I used two different approaches to couple light to on-chip devices. For WGM cavities, laser light was coupled evanescently using a single-mode optical fiber which had been pulled under a hydrogen flame to a diameter of ~ 1 *mu* m. We had to fabricate the tapered fibers ourselves. The process is discussed later. For PhC cavities light was coupled onto the chip using lensed fibers. Several kinds of single-mode lensed fibers were used including tapered lensed fibers from Nanonics Imaging and laser etched lensed fiber from Oz Optics. Polarization maintaining lensed fiber was also used.

1.5.1 Lensed Fiber Setup

Fig. shows the basic components of the lensed fiber coupling test setup. The other components of the setup will depend on the specific experiment and will therefore be described in later chapters. The test chip is mounted on the central 4-axis stage. Lensed fibers are positioned on both sides of the chip by high precision XYZ translational stages. The stages

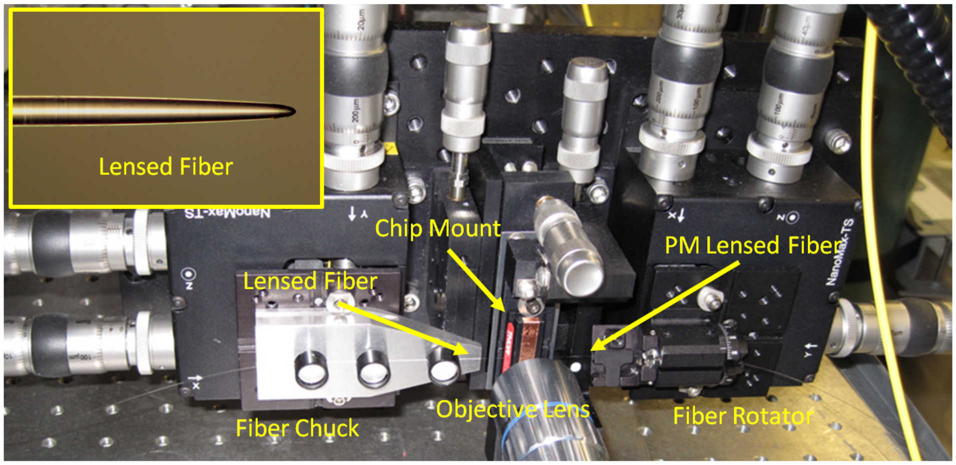

Figure 1.4: Lensed fiber experimental setup, Inset: Closeup image of lensed fiber made by Nanonics Imaging Ltd.

have optional piezoelectric actuators.

Laser light was sent through single mode optical fiber and coupled to strip waveguides on the test chip using the lensed fiber shown in the inset to Fig. . Sometimes spot-size coverters (made of either polymer or oxide) were used to reduce the coupling loss to ∼ 1 dB for TE polarized light [30]. The strip waveguide is then butt-coupled to a suspended PhC line defect waveguide. Light is coupled to the PhC cavity by tunneling through several layers of air-holes. Due to the number of coupling interfaces, as well as waveguide propagation losses, the total losses experienced when using the lensed fiber test setup are higher than the total losses when using the tapered fiber coupling setup.

1.5.2 Tapered Fiber Setup

The tapered fiber test setup shown in Fig. is similar to the design used by Kartik Srinivasan at the National Institute of Standards and Technology (NIST). Kartik provided us with generous help, both with this test setup as well as the accompanying tapered fiber pulling setup.

I worked with Felice Gesuele, a postdoc in our group, to build this test setup. Later the test setup was also used by other group members for numerous experiments. The sample is mounted on a stage with both XYZ translational movement as well as complete rotational movement. The tapered fiber is mounted on an adjacent XYZ translational stage with piezoelectric actuators which can be used to scan the tapered fiber with 5 nm resolution across a range of 20 μ m. A long working-distance objective lens is used to image the test sample and tapered fiber. The objective lens is connected to an ultra zoom system and images are captured using a CMOS video camera.

For certain experiments, an oxygen-free environment is necessary. Hence, the test setup is enclosed in a nitrogen box. Even when nitrogen is not used, the enclosure serves to minimize air flow thereby improving the stability of the tapered fiber. There were actually several alternative gases to nitrogen we considered. Both argon and sulfur hexafluoride are inert, non-toxic gases with higher densities than nitrogen. Argon is 40% denser and sulfur hexafluoride is 483% denser. Denser gases will stay in an enclosed area for longer periods of time. While we found this to be highly advantageous, our setup happened to be located in small room with no ventilation [3]. Additionally, both gases are colorless and odorless. In the end we decided nitrogen was the wiser choice.

The front panel of the nitrogen box is similar to a glove box, thereby allowing access to the manual stage controls even when the box is filled with nitrogen gas. The box was not designed to have a perfect air-tight sealing. Instead, nitrogen is flowed into the chamber on one side and flowed out of the chamber on the other. Flow meters at both the input and output are used to ensure the pressure inside of the box is higher than outside.

1.5.3 Tapered Fiber Pulling

Tapered fibers are pulled using a hydrogen flame setup shown in Fig. 1.5. The setup was built by Xiaodong Yang, a previous doctoral student in our group.

The procedure is as follows: A length of fiber is cut from a spool of Corning SMF-28e single mode optical fiber. Next, the polymer coating is stripped from both ends as well as in the center. These areas are then cleaned with isopropanol. The ends are cleaved and inserted into bare fiber connectors which are then connected to an ASE laser and optical spectrum analyzer (OSA) as shown in Fig. 1.5 (a). The fiber is then clamped down onto

---

[3] Argon is commonly used in the poultry industry as an asphyxiant.

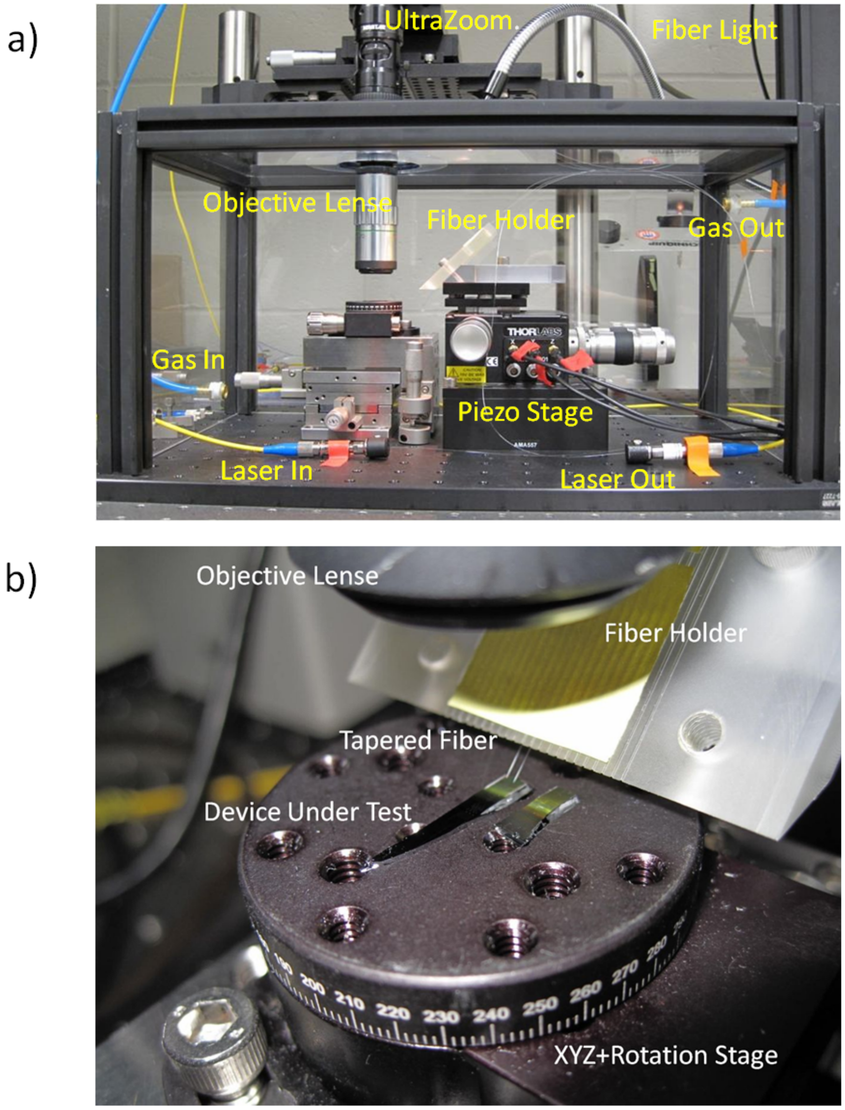

Figure 1.5: Tapered fiber test setup. (a) Nitrogen box enclosure of the tapered fiber setup. (b) The tapered fiber is mounted on the holder and used to probe optical devices on the silicon test chip. Positioning is done using precision XYZ translational stages as well as a rotational stage. The fiber and device are imaged using a long working distance objective lens.

stages attached to two linear motors. The hydrogen gas is turned on and the hydrogen flame is ignited using a flint lighter. Next, the linear motors slowly pull on two ends of the fiber while a small cladding-stripped region along the mid-length of the fiber is exposed to the hydrogen flame. The hydrogen flame in air has a blue color and a temperature of 2100 °C. This is higher than the melting point of silica, so the flame needs to be kept small and stable. The optical transmission is monitored on the OSA to determine the stop point whereupon the minimum fiber diameter has decreased from 9 μm to approximately 1 μm. The taper is then bent, with a resulting bend radius of approximately 0.5 mm, and attached with adhesive tape to a fiber mount. A high quality tapered fiber can have losses as low as 2 dB. Over long periods of time, the lossiness of the fiber steadily increases due to environmental contamination.

In actuality, pulling a good fiber is harder than it seems. In our group, this setup has long been akin to a medieval torture device [4] due to the long hours of frustration endured by helpless graduate students trying to pull a single tapered fiber, so that they could carry on with their experiments. Having suffered through this inhumane torture, I decided to carefully study the causes of fiber breakage so that I could improve the setup.

The overwhelming majority of fiber breakages occur after the fiber has already been pulled and is being removed from the setup. Fig.1.7 shows two common causes of breakage. In Fig.1.7 (a) the fiber breaks as the fiber clamps are lifted. This is generally due to tension in the fiber line. In Fig.1.7 (b) the fiber breaks as the fiber is lifted off of the fiber mounts. This is due to forces exerted by the person's hands. Sadly, most engineers lack the fine motor skills of a neural surgeon.

After some experimentation, I found solutions to both of these problems. Fig. 1.8 (a) shows how long tubes for holding the fiber are added to both stages. The tubes serve to remove tension in the fiber line which is caused by bends in the fiber. In Fig. 1.8 (b) the clamps holding the fiber down can be removed without any risk of fiber breakage. The solution to the second problem is shown in 1.8 (c). Instead of using both hands to remove the fiber, simply use one hand. The same hand bends the fiber and grabs the other end. Then the fiber is then mounted onto the fiber holder. As simple as this procedure now

---

[4] The rack was a medieval contraption for pulling people rather than optical fibers.

appears, it was quite unexpected when it worked the first time due to the extreme fragility of the fiber taper. These improvements made it much easier for our group to pull high quality tapered fibers.

1.6 Design Layout

All of the early chip layout in our group was done using AutoCAD. This worked fine for a surprisingly long time but design software such as AutoCAD is inherently unsuitable for chip layouts with large numbers of photonic crystal devices. AutoCAD does not support hierarchical design, i.e. in AutoCAD every point on the design must be specified in memory even when there are large numbers of repeating units. The repeating air-holes in photonic crystal structures can quickly result in enormously sized design files. This eventually became a problem with our mask maker. I was already familiar with hierarchical design from my earlier work fabricating large-scale bioarrays for biological studies. I began looking for a hierarchical design tool to solve our problems. With help from Frank Zhang, a graduate student working in chip design, I was able to start designing my photonic crystal layouts using Cadence Virtuoso. Virtuoso turned out to be a good choice because of its powerful scripting language. A fellow group member, James McMillan, quickly became a virtuso at Cadence Virtuoso. He wrote a number of software tools which have greatly simplified the the design layout process.

Fig. 1.9 shows one of our typical chip layouts. The chip is $\sim$ 25 x 12 mm in size and contains designs from most of our group members. Using high resolution photolithography, an entire wafer of these chips can be fabricated at a foundry with relative ease, something which is not possible with e-beam lithography. The downside of the photolithography approach in research is the long lag-times between fabrication runs. When many design-fabricate-test iterations are needed, direct-write e-beam lithography is preferable.

1.7 Simulations

Simulation tools are a valuable resource for analyzing electromagnetic phenomena in dielectric micro- and nanostructures. Some tools are frequency-domain while others are time-

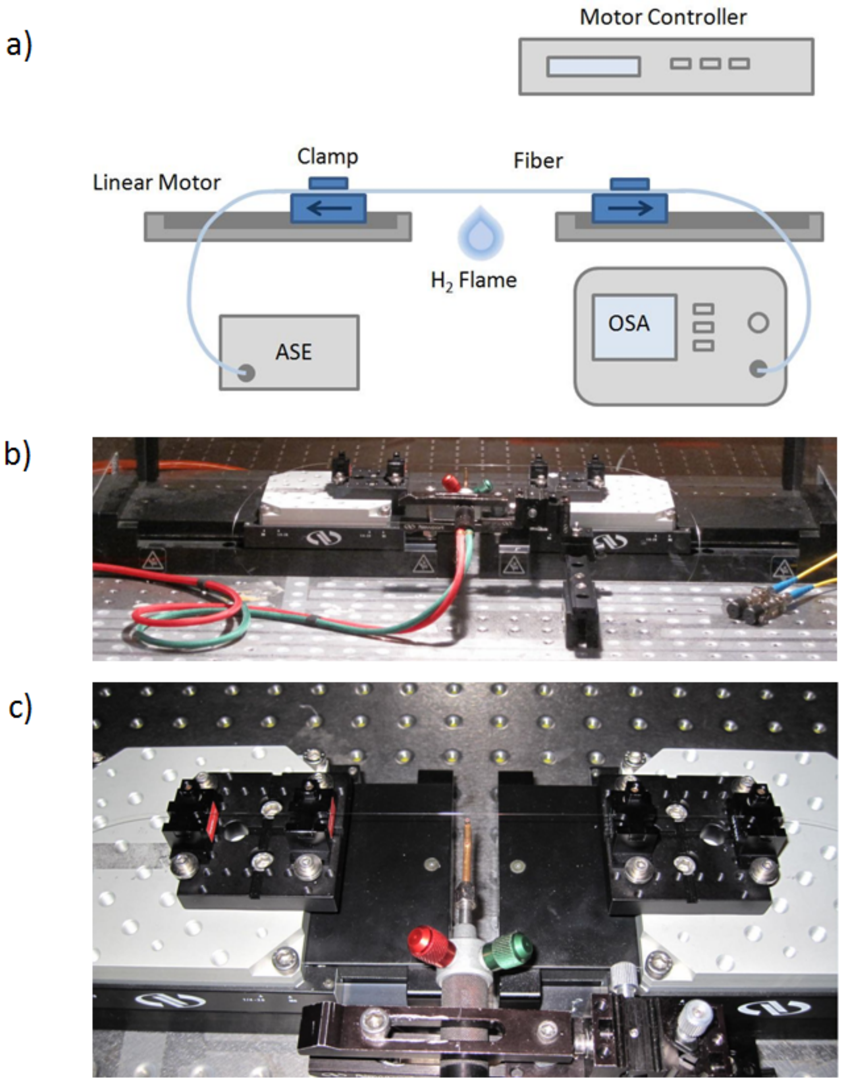

Figure 1.6: Tapered fiber pulling setup.

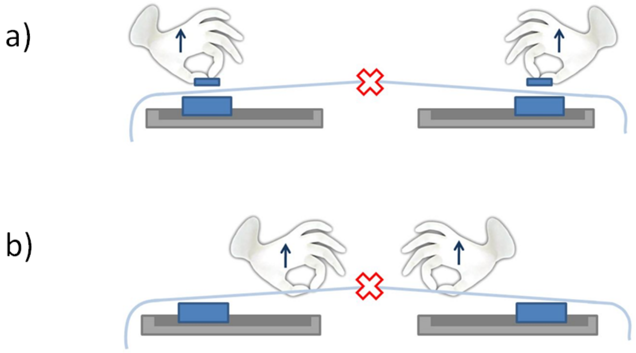

Figure 1.7: After pulling the fiber down to an ~ 1 μm diameter taper, it becomes extremely fragile. Here are some common causes of fiber breakage when removing the fiber from the pulling setup.

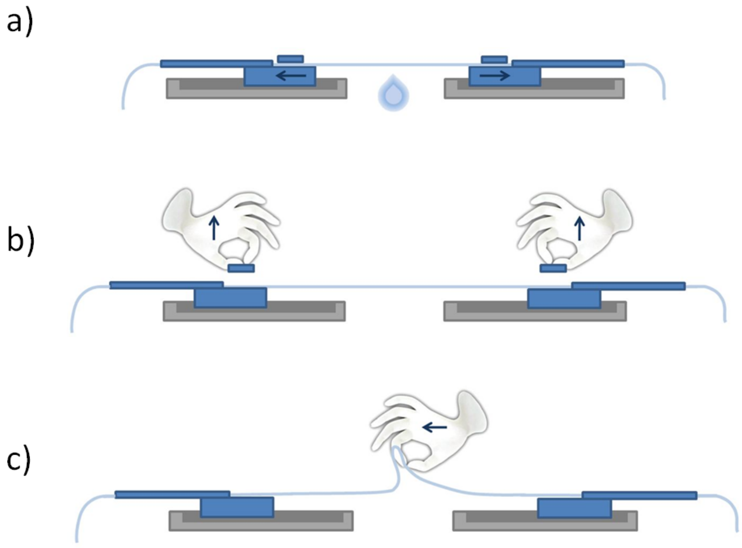

Figure 1.8: Improvements to the tapered fiber setup and pulling technique.

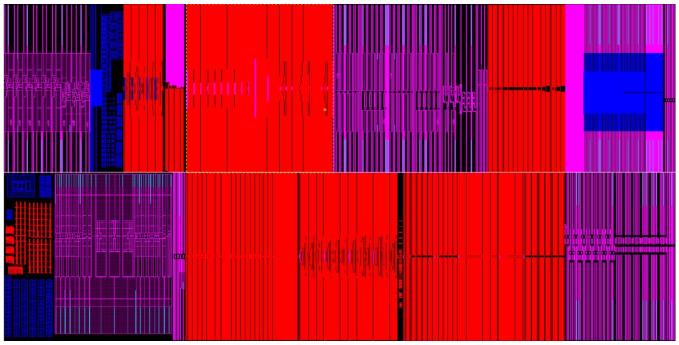

Figure 1.9: Chip layout containing designs from many group members. Such a large chip (∼ 25 x 12 mm) is impractical to fabricate by e-beam lithography due to the long write time. Large numbers of this chip design were fabricated by deep-UV photolithography at IME's research foundry.

domain. The plane wave expansion (PWE) method is used to solve Maxwell's equations (Eqns. 1.7-1.10) in the frequency- domain by direct computation of eigenstates and eigenvalues. Finite-difference time domain (FDTD) solves Maxwell's equation in partial differential form on a discretized grid. The finite-element method (FEM) is a numerical technique that also solves partial differential equations but often using a highly non-uniform mesh. All three of these methods can be used for solving problems in electromagnetics, each with it's own pros and cons. I have used the last method, FEM, for modeling thermal effects. These tools are available in both commercial as well as open source software packages.

$$\nabla \cdot D = \rho_f \tag{1.7}$$

$$\nabla \cdot B = 0 \tag{1.8}$$

$$\nabla \times E = -\frac{\partial B}{\partial t} \tag{1.9}$$

$$\nabla \times H = J_f + \frac{\partial D}{\partial t} \tag{1.10}$$

1.7.1 Frequency Domain Mode Solver - MPB

MIT Photonic Bands (MPB) is freely available software developed by the group of John Joannopoulos at the Massachusetts Institute of Technology [31, 32, 33]. MPB is an iterative eigensolver of Maxwell's equations in the frequency domain. The error in mode calculation decreases exponentially with the number of iterations. This efficiency allows the program to run well on a single computer as opposed to a computer cluster.

I used MPB for calculating the band structure of photonic crystal geometries. The program can also be used to calculate resonantor modes. The modes and field data are determined simultaneously and can be quickly outputted and visualized. The program is not well-suited for calculating time-dependent properties, such as temporal losses (waveguide propagation losses, cavity Q factor, etc.).

1.7.2 Finite-Difference Time-Domain - MEEP and Fullwave

The finite-difference time-domain (FDTD) method calculates the time-dependent Maxwell's equations on a discrete grid in an iterative fashion. First the electric field vector components are solved for a time increment. Then the magnetic field vector components are solved for the next time increment [34]. And the process repeats itself.

When I first started on simulations, I used RSoft Fullwave which is commerical software that is widely used in the photonics industry. In 2006, Steven Johnson at MIT released Meep which is freely available open-source software that can be customized for specific purposes. I immediately began using this software also [35, 36]. Eventually, half of our group members converted to Meep. The other half has been quite happy with Fullwave.

The FDTD method is good for solving problems which involve losses. I have used it to calculate the Q-factor of different optical resonator designs. The electric field data can be outputted and used to determine the modal volume of a cavity. The FDTD method is also suitable for calculating waveguide transmission and simulating the effects of nonlinear materials.

Unlike the frequency-domain method described in the previous section, the FDTD method is computationally more intensive. I generally start out with a 2-D simulations a single computer. Once I am reasonably confident about my design and simulation parameters, I will move to 3-D simulations run on a multi-node linux cluster. Clustering allows the problem to be broken up and solved in parallel, thereby increasing the overall memory size and ultimately the resolution of the simulation. It does not necessarily improve the time needed to run the simulation.

1.7.3 Finite Element - Comsol Multiphysics

I use COMSOL Multiphysics, a commercial software package based on FEM, for modeling thermal effects during processes such as laser irradiation, oxidation, annealing and melting. Other group members have also used COMSOL in place of Meep or Fullwave. FEM does not require a rectangular grid and can be optimized for for complex geometries by varying the density of grid points at different locations (Fullwave also supports a non-uniform grid).

Bibliography

[1] `http://nobelprize.org/nobel_prizes/physics/laureates/2009/`.

[2] MIT Microphotonics Center Industry Consortium, "2005 Communications Technology Roadmap: Silicon Microphotonics." `http://mphotonics.mit.edu/`.

[3] R. Soref, "The past, present, and future of silicon photonics," *IEEE Journal of Selected Topics in Quantum Electronics*, vol. 12, pp. 1678 –1687, Nov. 2006.

[4] H. Rong, R. Jones, A. Liu, O. Cohen, D. Hak, A. Fang, and M. Paniccia, "A continuous-wave Raman silicon laser," *Nature*, vol. 433, pp. 725–728, Feb. 2005.

[5] Q. Xu, B. Schmidt, S. Pradhan, and M. Lipson, "Micrometre-scale silicon electro-optic modulator," *Nature*, vol. 435, pp. 325–327, May 2005.

[6] B. Jalali and S. Fathpour, "Silicon photonics," *Journal of Lightwave Technology*, vol. 24, no. 12, pp. 4600–4615, 2006.

[7] J. Cardenas, C. B. Poitras, J. T. Robinson, K. Preston, L. Chen, and M. Lipson, "Low loss etchless silicon photonic waveguides," *Optics Express*, vol. 17, no. 6, pp. 4752–4757, 2009.

[8] B. E. A. Saleh and M. C. Teich, *Fundamentals of Photonics, 2nd ed.* Wiley, 2007.

[9] `http://techresearch.intel.com/`.

[10] M. Hochberg and T. Baehr-Jones, "Towards fabless silicon photonics," *Nature Photonics*, vol. 4, pp. 492–494, 2010.

[11] K. C. Leuthold, J. and W. Freude, “Nonlinear silicon photonics,” *Nature Photonics*, vol. 4, pp. 535–544, 2010.

[12] M. Soljačić and J. D. Joannopoulos, “Enhancement of nonlinear effects using photonic crystals,” *Nature Materials*, vol. 3, pp. 211–219, 2004.

[13] J. Niehusmann, A. Vörckel, P. H. Bolivar, T. Wahlbrink, W. Henschel, and H. Kurz, “Ultrahigh-quality-factor silicon-on-insulator microring resonator,” *Optics Letters*, vol. 29, pp. 2861–2863, 2004.

[14] Q. Xu, D. Fattal, and R. G. Beausoleil, “Silicon microring resonators with 1.5-μm radius,” *Optics Express*, vol. 16, no. 6, pp. 4309–4315, 2008.

[15] M. Soltani, S. Yegnanarayanan, and A. Adibi, “Ultra-high Q planar silicon microdisk resonators for chip-scale silicon photonics,” *Optics Express*, vol. 15, pp. 4694–4704, 2007.

[16] M. Soltani, Q. Li, S. Yegnanarayanan, and A. Adibi, “Toward ultimate miniaturization of high Q silicon traveling-wave microresonators,” *Optics Express*, vol. 18, no. 19, pp. 19541–19557, 2010.

[17] J. Gao, P. Heider, C. J. Chen, X. Yang, C. A. Husko, and C. W. Wong, “Observations of interior whispering gallery modes in asymmetric optical resonators with rational caustics,” *Applied Physics Letters*, vol. 91, no. 18, p. 181101, 2007.

[18] Q. J. Wang, C. Yan, N. Yu, J. Unterhinninghofen, J. Wiersig, C. Pflugl, L. Diehl, T. Edamura, M. Yamanishi, H. Kan, and F. Capasso, “Whispering-gallery mode resonators for highly unidirectional laser action,” *Proceedings of the National Academy of Sciences*, vol. 107, pp. 22407–22412, 2010.

[19] Y. Akahane, T. Asano, B. Song, and S. Noda, “High-Q photonic nanocavity in a two-dimensional photonic crystal,” *Nature*, vol. 425, pp. 944–947, 2003.

[20] Y. Akahane, T. Asano, B.-S. Song, and S. Noda, “Fine-tuned high-Q photonic-crystal nanocavity,” *Optics Express*, vol. 13, no. 4, pp. 1202–1214, 2005.

[21] E. Kuramochi, M. Notomi, S. Mitsugi, A. Shinya, T. Tanabe, and T. Watanabe, "Ultrahigh-Q photonic crystal nanocavities realized by the local width modulation of a line defect," *Applied Physics Letters*, vol. 88, no. 4, p. 041112, 2006.

[22] B. Song, S. Noda, T. Asano, and Y. Akahane, "Ultra-high-Q photonic double-heterostructure nanocavity," *Nature Materials*, vol. 4, pp. 207–210, 2005.

[23] T. Asano, B.-S. Song, and S. Noda, "Analysis of the experimental Q factors (~ 1 million) of photonic crystal nanocavities," *Optics Express*, vol. 14, pp. 1996–2002, Mar. 2006.

[24] S. L. McCall, A. F. J. Levi, R. E. Slusher, S. J. Pearton, and R. A. Logan, "Whispering-gallery mode microdisk lasers," *Applied Physics Letters*, vol. 60, pp. 289–291, 1992.

[25] X. Liu, W. Fang, Y. Huang, X. H. Wu, S. T. Ho, H. Cao, and R. P. H. Chang, "Optically pumped ultraviolet microdisk laser on a silicon substrate," *Applied Physics Letters*, vol. 84, no. 14, pp. 2488–2490, 2004.

[26] T. J. Kippenberg, J. Kalkman, A. Polman, and K. J. Vahala, "Demonstration of an erbium-doped microdisk laser on a silicon chip," *Physical Review A*, vol. 74, p. 051802, Nov. 2006.

[27] T. J. Johnson, M. Borselli, and O. Painter, "Self-induced optical modulation of the transmission through a high-q silicon microdisk resonator," *Optics Express*, vol. 14, pp. 817–831, Jan. 2006.

[28] K. Srinivasan and O. Painter, "Linear and nonlinear optical spectroscopy of a strongly coupled microdisk-quantum dot system," *Nature*, vol. 450, pp. 862–865, 2007.

[29] J. Wiersig and M. Hentschel, "Combining directional light output and ultralow loss in deformed microdisks," *Physical Review Letters*, vol. 100, p. 033901, Jan. 2008.

[30] S. McNab, N. Moll, and Y. Vlasov, "Ultra-low loss photonic integrated circuit with membrane-type photonic crystal waveguides," *Optics Express*, vol. 11, pp. 2927–2939, Nov. 2003.

[31] S. G. Johnson and J. D. Joannopoulos, “Block-iterative frequency-domain methods for Maxwell’s equations in a planewave basis,” *Optics Express*, vol. 8, no. 3, pp. 173–190, 2001.

[32] S. G. Johnson, “Mit Photonic Bands.” `http://ab-initio.mit.edu/wiki/index.php/MIT_Photonic_Bands`, 2009.

[33] J. D. Joannopoulos, S. G. Johnson, J. N. Winn, and R. D. Meade, *Photonic Crystals: Molding the Flow of Light (Second Edition)*. Princeton University Press, 2 ed., 2008.

[34] K. Yee, “Numerical solution of initial boundary value problems involving Maxwell’s equations in isotropic media,” *IEEE Transactions on Antennas and Propagation*, vol. 14, pp. 302 –307, May 1966.

[35] A. F. Oskooi, D. Roundy, M. Ibanescu, P. Bermel, J. D. Joannopoulos, and S. G. Johnson, “MEEP: A flexible free-software package for electromagnetic simulations by the FDTD method,” *Computer Physics Communications*, vol. 181, pp. 687–702, Jan. 2010.

[36] S. G. Johnson, “MEEP - AbInitio.” `http://ab-initio.mit.edu/wiki/index.php/Meep`, 2009.

Chapter 2

Local Oxidation Resonance Tuning

2.1 Introduction

Photonic crystal nanocavities are increasingly employed in photonic studies and applications because of their high quality factor (Q) to modal volume (V_m) ratios [1, 2, 3]. These nanocavities are also used in photonic devices of increasing complexity where high accuracy of the resonant wavelength is critical. However, due to fabrication imperfections, resonances will often deviate from their desired precise values. Several post-fabrication tuning techniques have been proposed and demonstrated to address this issue. Some of these techniques are listed in Table 2.1, where a positive tuning increment represents a redshift in the cavity resonance, while a negative tuning increment represents a blueshift. These methods can be divided into 2 groups: global and local. Global tuning creates a uniform change over the entire chip, [4, 5, 6] whereas local tuning only changes a small area such as a single nanocavity [8, 9, 10, 11, 12, 13, 14]. Global tuning is useful for correcting uniform errors but cannot address the random local errors that often occur during fabrication. Local tuning can be very important to applications such as the all-optical analog to electromagnetically induced transparency [2] and optical buffers, which require precisely coupled cavities. Another example is in solid-state cavity quantum electrodynamics where local tuning can be used to spectrally match a cavity resonance to a single exciton transition.

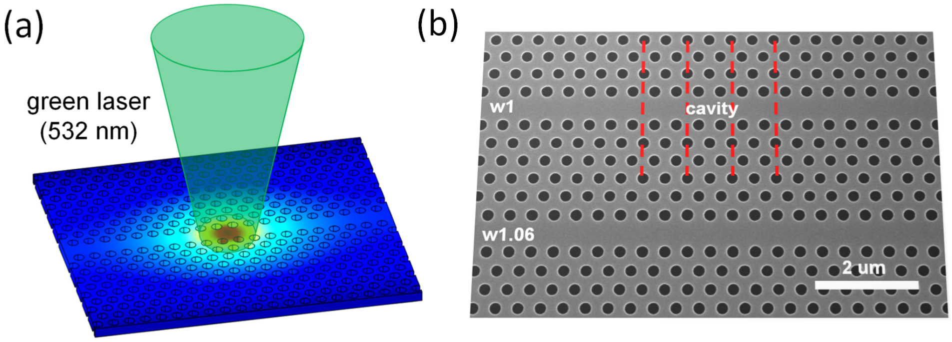

Figure 2.1: (a) Illustration of laser-assisted local thermal oxidation in a silicon double-heterostructure cavity. (b) SEM image of a double-heterostructure cavity.

In this work, we study the selective thermal oxidation of silicon photonic crystal membranes with a highly localized laser beam at ambient conditions in order to finely tune the high-Q resonances. Laser-assisted local oxidation is advantageous to previously demonstrated tuning techniques because it allows for automation of the tuning process by using a computer-controlled stage, shutter or optical modulator and in-situ monitoring system. Such a system would enable the post-fabrication fine-tuning of large numbers of nanocavities.

Laser-assisted local tuning has been demonstrated with the photodarkening of chalcogenide films on GaAs photonic crystals [10] with a Q of $\sim$ 8000. Laser-assisted local tuning has also been studied in the oxidation of GaAs photonic crystal L3 cavities [8] with a Q of 1800. In this work, we study the precise local tuning in silicon, of photonic crystal double-heterostructure nanocavities with high-Qs of $\sim$ 200,000 or higher.

Continuous-wave lasers have been used in oxidation studies of silicon and silicon-on-insulator substrates [15, 16], including temperature independent contributions to silicon oxidation from photon flux [15]. Using a diffraction limited beam, Deustchmann et al. [17] was able to oxidize lines as narrow as 200 nm at a power of approximately 15 mW. Such spatial confinement is possible in thin single crystal silicon films because increased phonon scattering reduces heat flow in the lateral direction [18]. In addition to cavity tuning, local oxidation might be applicable to other post-fabrication tasks such as tuning the dispersion [19, 20] and surface states [21, 22].

2.2 Local oxidation cavity resonance tuning

The photonic crystal double-heterostructure nanocavities [1] used in this work were fabricated by high quality photolithography and dry etching on silicon-on-insulator (250 nm thick) substrates, with 117 nm hole radii and 410 nm lattice parameter. In the cavity region, the lattice parameter increases to 415 and 420 nm. The waveguide-to-cavity separation is 6 layers of air-holes. Approximately 1.5 μm of oxide beneath the photonic crystal region was removed as described in Ref. 4.

A 532 nm diode-pumped solid-state laser, with a collimated beam and power controlled using a variable neutral density filter to $\sim$ 20 mW powers, was used. A 60× objective lens (NA of 0.65) focuses the laser onto the chip and is also used for imaging. The spot-size is measured using the knife-edge technique. The full-width half-maximum beam waist was

Table 2.1: Passive post-fabrication photonic-crystal cavity tuning techniques.

Method	**Material**	**Extent**	**Tuning Range**	**Tuning Increment**	**Ref.**
Atomic Layer Deposition	Si	global	> 20 nm	+122 pm	[4]
Chemical Oxidation	Si	global	> 20 nm	-430 pm	[5]
Wet Etching	GaAs	global	> 20 nm	-2.1 nm	[6]
Self-Assembled Monolayer	GaAs	global	3-5 nm	+3-5 nm	[7]
Laser-Assisted Local Oxidation	GaAs	local	2.5 nm	$\sim$ -200 pm	[8]
Electron-Beam Induced Nanodots	InGaAsP	local	14 nm	$<$ +200 pm	[9]
Photodarkening of Chalcogenide	GaAs	local	3 nm	$<$ +250 pm	[10]
AFM Oxidation	GaAs	local	4 nm	-100 pm	[12]

2.5 μm, corresponding to a maximum energy density at the chip surface of 1×10^8 W/cm^2. The oxidation is carried out in ambient conditions of 22 °C and 20% relative humidity.

Cavity resonance transmission and radiation measurements were performed as described in Refs. 2 and 4. Oxidation results in a blueshift in the cavity resonance as shown in Fig. 2.4 (a). This is the result of a larger decrease in refractive index from the silicon consumed outweighing a smaller increase in refractive index from the oxide generated. Following the initial anomalous oxidation, subsequent tuning follows a parabolic rate law where the cavity resonance blueshift is observed to be proportional to the square root of the oxidation time (Fig. 2.4 (b) and (c)). The decreasing oxidation rate is attributed to the longer diffusion time of oxygen through the thicker oxide in order to reach the silicon-oxide interface where the oxide growth occurs [23]. Corresponding radiation measurements of the high-Q cavity are shown in Fig. 2.5.

Oxidation is expected to occur on both the top and bottom surfaces of the silicon membrane as well as the surface of the air holes because both the 1/e absorption depth of the green laser (1 μm) and the depth of focus of the beam after the objective lens (400 nm for 60× objective) are larger than the 250 nm thickness of the silicon membrane. The oxidation profile remains highly localized with AFM studies showing lateral dimensions 40% smaller than the spot diameter [16]. This can be attributed to a number of factors. The thermal conductivity of silicon is dominated by phonon transport with a smaller contribution from free charge carriers. While the thermal conductivity of silicon is relatively high at room temperature, it decreases significantly at higher temperatures with increased phonon scattering [24, 25]. In addition, as the substrate thickness decreases from bulk dimensions, phonon-boundary scattering increases and the presence of air holes will further decrease the phonon mean free path [18].

2.3 Transient effects from oxide surface chemistry

During the oxidation process, as the cavity is heated to high temperatures by optical absorption of the focused green laser beam, there will be a large redshift in the cavity resonance. The redshift is attributed to the thermal-optic effect in silicon causing a temperature-dependent refractive index change. When the green laser is turned off, the cavity temperature quickly returns to room temperature and the large redshift disappears. But within 1-2 minutes after oxidation (i.e. after the green laser is turned off), a smaller magnitude redshifting of the cavity resonance is observed. The rate of this redshifting is rapid at first and decreases over time, taking many hours to reach a stable value. This transitory effect is caused by water molecules on the surface of the cavity.

The surface chemistry effects occur both during and after laser irradiation, and are illustrated in Fig. 2.6. Upon heating the cavity there is a temporary blueshift from oxide surface and oxide bulk dehydration. After the cavity cools back down, there is a slow redshift caused by gradual rehydration of water molecules onto the cavity. The total shift ranges from $\sim$ 100 pm to hundreds of picometers and appears to be dependent on the oxide thickness. Laser exposure at low powers (less than 1 mW for 10 minutes) shows a completely reversible blueshift, indicating no real oxidation has occurred (i.e. there is only a temporary blueshift from cavity dehydration followed by a rehydration redshift returning the cavity resonance to its original wavelength).

Silicon dioxide terminated by hydroxyl groups (SiOH) is hydrophillic and will readily adsorb water molecules, as schematically shown in Fig. 2.6 (a). At temperatures above $\sim 170\,^{\circ}\mathrm{C}$ the hydrogen bonded water molecules will desorb. The process is reversible but at higher temperatures ($400\,^{\circ}\mathrm{C}$) the hydrogen in the hydroxyl groups can sometimes be removed resulting in a hydrophobic siloxane surface. The long times required to complete the redshift are indicative of a slower diffusion-limited process [26, 27]. While water absorption is known to be much less significant for thermally grown oxides than deposited oxides, [28], studies of laser grown oxides indicate their composition are less dense than traditional thermally oxidized films due to presence of suboxides, especially for thinner films [29]. In order to obtain reliable results, our measurements were taken either immediately after oxidation (less than 1 min) when the cavity region was still dehydrated or immediately after the cavity was re-heated at sub-oxidation threshold powers.

2.4 Thermal oxidation

Prior to oxidation, the test chip had a native oxide (approximately 12 Å in thickness) as it was exposed to ambient conditions. In addition to the native oxide, it was observed that initial oxidation can occur at very low laser powers. Because of this, an accurate initial oxidation threshold power was difficult to determine. This initial growth was anomalous in respect to the Deal-Grove and Massoud models for oxide growth [23, 30]. It has been shown by x-ray photoelectron spectroscopy studies that the initial $\sim$ 22 Å of oxide growth occurs at a very high rate [31]. At this stage, even at very low powers oxidation might occur.

Following the initial anomalous oxidation, subsequent tuning follows a parabolic rate law. The oxidation resonance tuning is permanent and stable. Repeated measurements over the span of many days shows no change within the measurement error. The uncertainty in the cavity resonance measurements is approximately ± 100 pm and primarily attributed to random thermal fluctuations in the ambient environment. This uncertainty is the limiting factor in determining the minimum tuning increment. A number of other factors will affect the minimum achievable tuning increment including: power stability, exposure time accuracy, beam targeting accuracy and beam shape uniformity. Another group has demonstrated a resonance tuning increment of 100 pm using AFM nano-oxidation of GaAs [12].

The inset to Fig. 2.4 (a) shows quality factor measurements during the oxidation process. During the initial oxidation there is a sizeable drop in the Q. Afterwards the Q appears to remain stable upon further oxidation. The initial drop in Q might be attributed to increased optical scattering from the interfacial layer between the silicon and oxide. Surface states might also result in increased absorption at the interface. In this work, the local oxide was left on the chip after the tuning. Removing the oxide with an HF dip [8] has been shown to improve the Q and will also further blueshift the resonance.

The decrease in overall air-hole size can be used to estimate the oxide thickness. The SEM image in Fig. 2.1 (b) shows the double-heterostructure cavity after local oxidation resulting in a 2.1 nm cavity resonance blueshift. Image analysis of the experimental device indicates a hole size change smaller than the error of the SEM measurements (± 5% of the hole diameter). In addition, a redshift of 0.8 nm was observed in the cavity resonance after

SEM imaging the cavity region (Fig. 2.7 (b)). This is likely caused by contamination of the sample in the SEM chamber during imaging. It is well known that organic molecules from vacuum pump oil can be deposited onto the substrate surface by the focused electron beam during SEM imaging [9]. For this reason, SEM imaging was generally avoided while the sample was being tuned. Fig. 2.7 (a) shows an SEM image of the sample after a cavity resonance tuning of 10.4 nm. Using hole-size analysis it is estimated that 1 nm of resonance blueshift corresponds to 1.9 nm of oxide growth. A comparison with calculated resonance shifts is provided in the next section.

2.5 Numerical analysis

Three-dimensional finite-element simulations (COMSOL Multiphysics) are used to estimate the temperature increases caused by optical absorption at different laser powers. The model uses the static heat equation:

$$\nabla[\kappa(T)\nabla T] = -[1-R(T)]I_0\alpha(T)\exp\left(-\frac{(x^2+y^2)}{2\sigma^2}\right)\exp\left(-\int_0^z \alpha(T(x,y,z'))\mathrm{d}z'\right) \quad (2.1)$$

where $\kappa(T)$ is the temperature-dependent thermal conductivity, $R(T)$ is the reflection coefficient and $\alpha(T)$ is the temperature-dependent absorption coefficient. The incident CW laser beam has a Gaussian spatial distribution with a 1/e-squared beam spot-size σ and a center intensity I_0. The reflection coefficient takes the form $R(T) = R_0 + c(T - T_0)$ [32, 15]. The temperature dependent absorption is experimentally fitted as $\alpha(T) = \alpha_0 \exp(T/T_0)$ [33]. Both the absorption and thermal conductivity of silicon are temperature dependent. The absorption of silicon increases significantly at higher temperatures. The thermal conductivity for bulk silicon at room-temperature is 148 $\mathrm{WK^{-1}m^{-1}}$ but as the temperature increases, the thermal conductivity will decrease. For a thin porous photonic crystal slab, the thermal conductivity can be reduced even further. In-plane thermal conductivity is reduced to approximately 90 $\mathrm{WK^{-1}m^{-1}}$ at room temperature for silicon-on-insulator (SOI) devices with a silicon thickness of 260 nm [34], mainly due to increased phonon boundary scattering [25, 35, 36]. Periodic structures on single-crystalline silicon membranes can have thermal conductivity values as small as $\sim$ 6.8 $\mathrm{WK^{-1}m^{-1}}$ due to coherent phononic effects [37].

In order to determine the thermal conductivity for our device, we used our finite-element model along with experimental measurements. Silicon melting is observed to occur at incident laser powers of $\sim$ 35 mW as shown in Fig. 2.7 (a). This was used as a reference point for our model and the resulting room-temperature thermal conductivity was estimated to be 67 $\mathrm{WK^{-1}m^{-1}}$. The simulated temperature profile around the double-heterostructure cavity is shown in Fig. 2.8 (a). Cross-sections of the temperature profile corresponding to incident power of 30 mW and 35 mW are shown in Fig. 2.8 (b) along with the laser intensity profiles at those powers. The temperature profiles show how the temperature gradient increases due to higher absorbed energies and lower thermal conductivity at higher membrane temperatures. The local maximum temperature for different incident laser powers is shown in Fig. 2.8 (c). The features observed in Fig. 2.7 (a) are consistent with results of the numerical model.

The finite-difference-time-domain (FDTD) method [38] with sub-pixel averaging [39] is used to calculate the effects of silicon oxidation on the cavity resonance. The native oxide is assumed to be 1.2 nm. We also assume that if 1 nm of silicon is oxidized (consumed), the resulting oxide grown is 2.17 nm. As the silicon is consumed, the total thickness of the slab (silicon + oxide) will increase, while the air-hole radii will decrease. Simulation results in Fig. 2.9 (b) show that every 0.6 nm of oxide grown results in 1 nm of resonance blueshift. By comparison, the previously discussed SEM hole analysis estimates that 1.9 nm of oxide growth results in 1 nm of resonance blueshift. There are several possible explanations for this discrepancy. It is possible that the amount of oxidation on the bottom-side of the silicon membrane is less than the top-side if the beam focus is less than optimal. In addition, the laser grown oxide might be less dense than furnace grown thermal oxide [29]. Finally, the slight melting of the silicon membrane at 35 mW laser irradiation might have resulted in a decrease in the air-hole size without a proportional increase in oxide growth.

2.6 Conclusions

We have demonstrated the tuning of high-Q double-heterostructured silicon photonic crystal nanocavities using laser-assisted local thermal oxidation. Cavity Q is preserved in the range 2×10^5, for the range of oxidation times and laser powers examined. The effects of water absorption and thin oxide growth were also observed. Numerical simulations were used to model the temperature distribution in the silicon photonic crystal membrane and resonance shift of the optical mode due to oxidation. While our work only focuses on laser-assisted thermal oxidation, other work has shown that under certain conditions there are temperature independent contributions to silicon oxidation from photon flux [15].

2.7 Acknowledgements

This work was done in collaboration with Jiangjun Zheng, a postdoc in our group. I worked on the the experimental setup, local oxidation process and optical experiments. Jiangjun worked on the device fabrication, thermal simulations, and finite-difference time-domain simulations. The boundary conditions for the finite-element thermal simulations were experimentally determined using a chip fabricated by Tingyi Gu. Chip fabrication was also performed at the Institute of Microelectronics in Singapore by Mingbin Yu, Guo-Qiang Lo, and Dim-Lee Kwong. The original idea for this experiment was proposed by James McMillian, another member of our group.

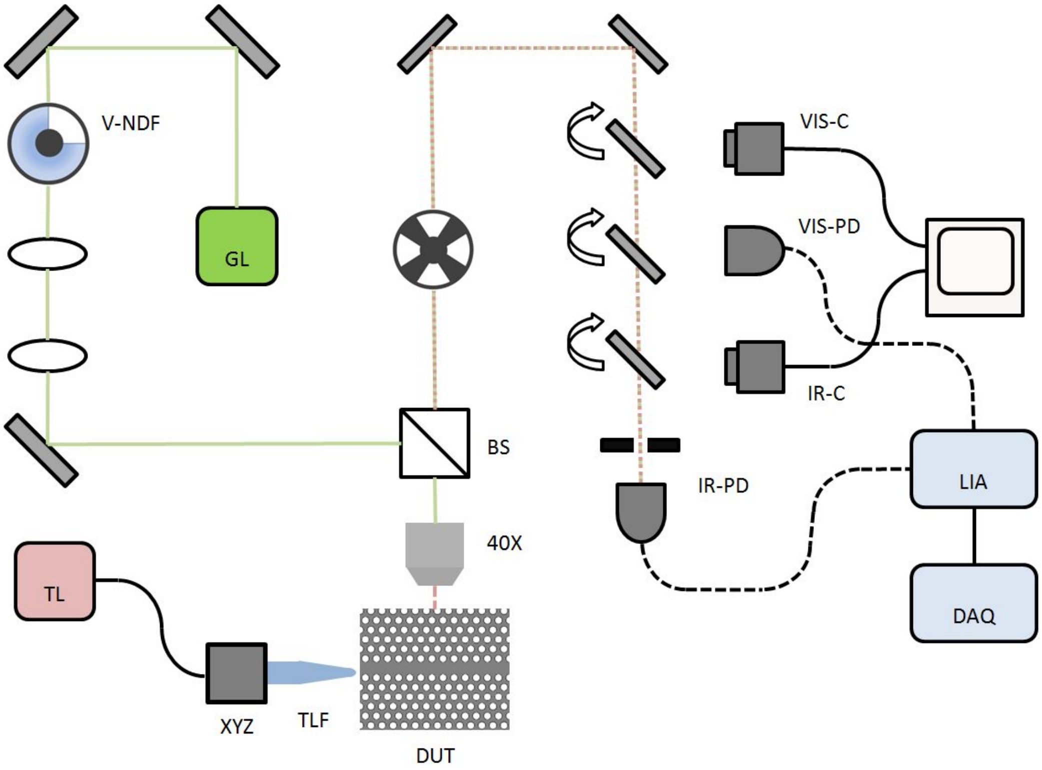

Figure 2.2: Experimental setup for local oxidation tuning and cavity resonance measurements. The green laser on the left-hand side is used to assist the thermal oxidation. On the right-hand side are cameras and photodetectors operating at both visible and IR wavelengths. The cameras are used to image the sample. The detectors are used to measure the radiation signal along with the lock-in amplifier and data acquisition system. At the bottom, near-IR light from a tunable laser is coupled onto the device under test by a tapered lensed fiber.

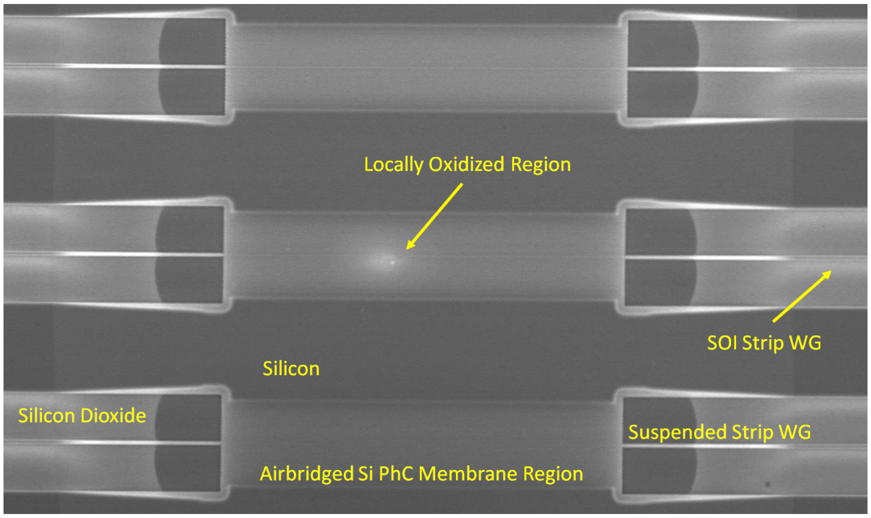

Figure 2.3: SEM image of a device after local oxidation. The oxidized region is white colored in the SEM because of charging effects in the non-conductive oxide. Note: this is a different device than the one used for cavity measurements in Fig. 2.4.

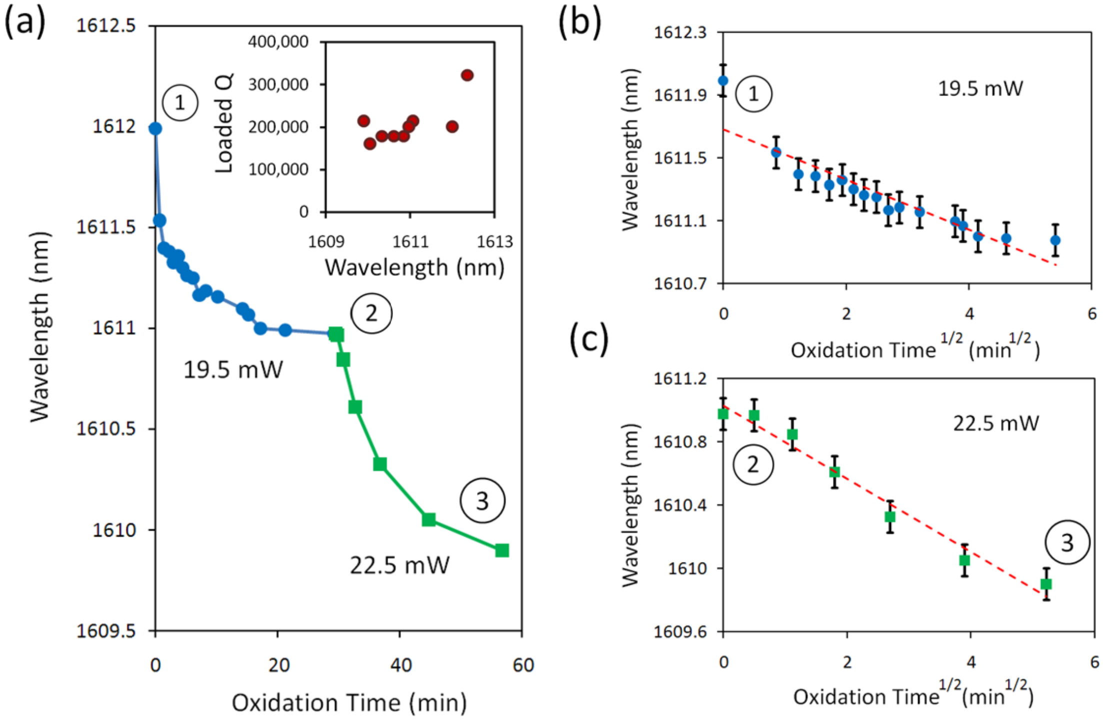

Figure 2.4: (a) Experimental results showing the blueshift from tuning using an initial laser power of 19.5 mW (at the device surface). The same device is then further tuned at 22.5 mW. The inset shows measurements of the loaded quality factor as the cavity is tuned. (b) Fitting of the resonant wavelength shift to the square root of oxidation time for incident power of 19.5mW and (c) for 22.5mW.

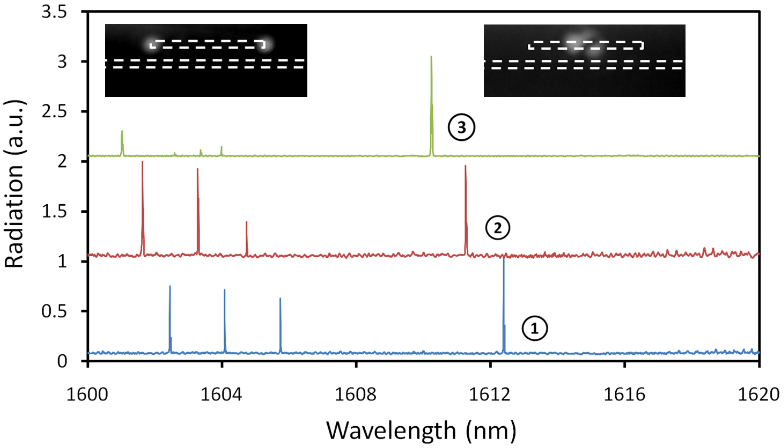

Figure 2.5: Radiation measurements at three different tuning increments corresponding to the numbered positions in Fig. 2. Left inset: near-IR radiation pattern for the Fabry-Perot modes on the left. The dotted lines indicate the position of cavity waveguide (upper) and input/output waveguide (lower). Right inset: near-IR radiation pattern for the cavity mode on the right.

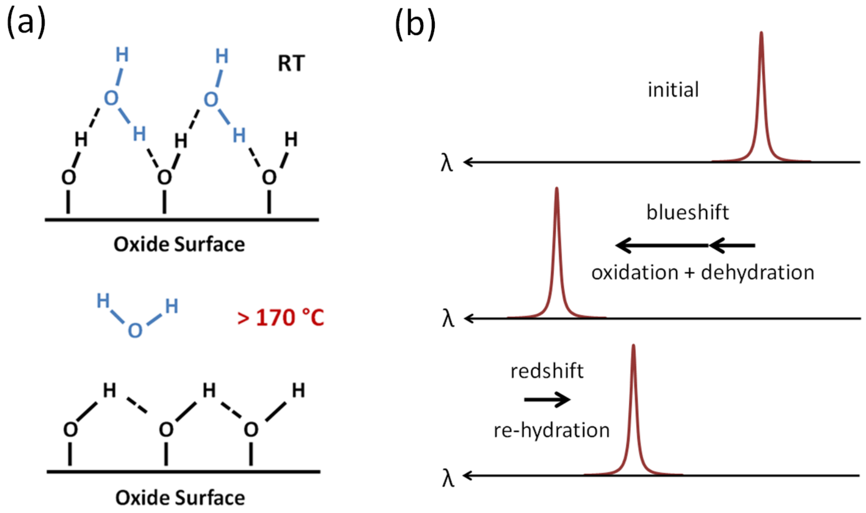

Figure 2.6: Transitory surface chemistry effects. (a) Water molecules absorb onto the oxide surface at room temperature and desorb from the oxide surface at elevated temperatures. (b) During laser irradiation, the cavity experiences a resonance blueshift from oxide dehydration in addition to silicon oxidation. After the cavity cools, water will slowly rehydrate the oxide surface resulting in a gradual redshift.

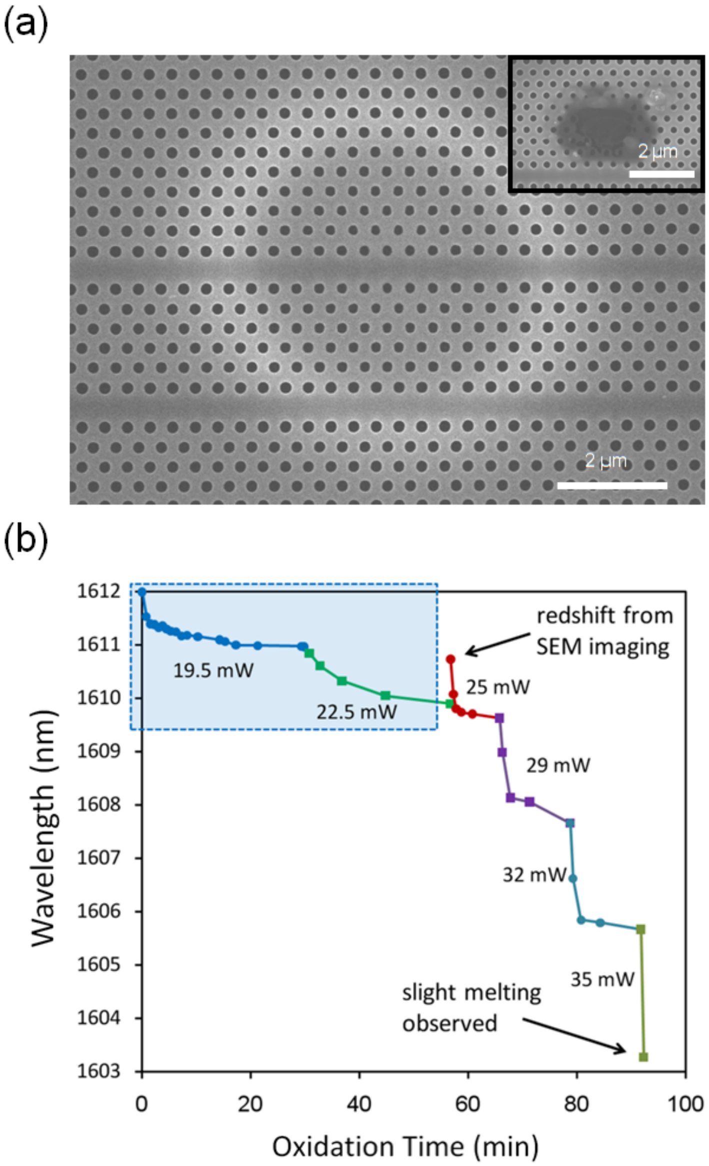

Figure 2.7: (a) SEM image of cavity after local oxidation tuning at laser power of 35 mW. The white ring indicates oxide charging effects during SEM imaging. The center region is darker because of slight melting. Inset: Hole melted through the silicon membrane after irradiation at ∼ 35 mW for several minutes (different device from the main figure). (b) Local oxidation tuning over a larger wavelength range. The blue region (upper-left) corresponds to the data shown in Fig. 2(a). The upper arrow corresponds to the SEM image in Fig. 1(b). The lower-right arrow corresponds to the SEM image in Fig. 5(a).

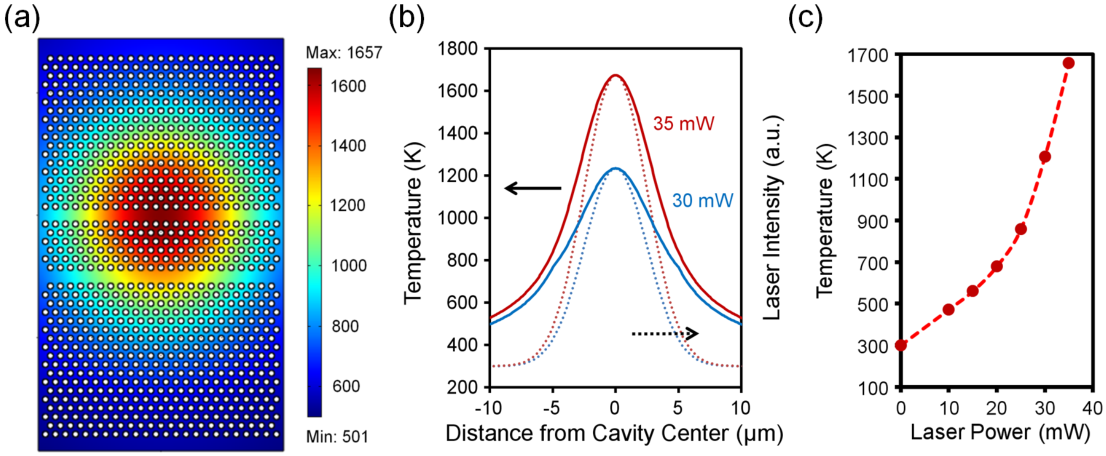

Figure 2.8: (a) Finite-element simulation (COMSOL Multiphysics) of temperature distribution across silicon double-heterostructure cavity during green laser irradiation at 35 mW. (b) Solid lines represent the temperature distribution as a function of distance from the center of the laser beam. Dotted lines represent the intensity profile of the laser beam. (c) Simulation results of local maximum temperature versus laser power. Temperatures range from room temperature to the melting point of silicon.

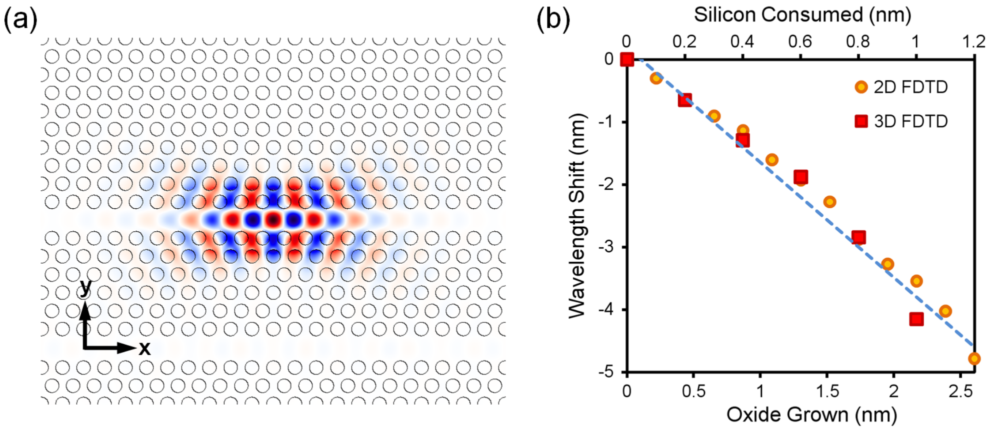

Figure 2.9: (a) Calculated electric field E_y profile of high-Q mode supported by double-heterostructure cavity. (b) Calculated wavelength shift of the resonant mode due to local oxidation of the silicon photonic crystal membrane.

Bibliography

[1] B. Song, S. Noda, T. Asano, and Y. Akahane, "Ultra-high-Q photonic double-heterostructure nanocavity," Nature Materials, **4,** 207-210 (2005).

[2] X. Yang, M. Yu, D.-L. Kwong, and C. W. Wong, "All-optical analog to electromagnetically induced transparency in multiple coupled photonic crystal cavities," Physical Review Letters, **102,** 173902 (2009).

[3] J. Gao, J. F. McMillan, M.-C. Wu, S. Assefa, and C. W. Wong, "Demonstration of an air-slot mode-gap confined photonic crystal slab nanocavity with ultrasmall mode volumes," Appl. Phys. Lett., **96,** 051123 (2010).

[4] X. Yang, C. J. Chen, C. A. Husko, and C. W. Wong, "Digital resonance tuning of high-Q/V$_m$ silicon photonic crystal nanocavities by atomic layer deposition," Applied Physics Letters, **91**(16), 161114 (2007).

[5] B.-S. Song, T. Nagashima, T. Asano, and S. Noda, "Resonant-wavelength tuning of a nanocavity by subnanometer control of a two-dimensional silicon-based photonic crystal slab structure," Applied Optics, **48**(26), 4899-4903 (2009).

[6] K. Hennessy and A. Badolato and A. Tamboli and P. M. Petroff and E. Hu and M. Atatüre and J. Dreiser and A. Imamoğlu, "Tuning photonic crystal nanocavity modes by wet chemical digital etching," Applied Physics Letters, **87**(2), 021108 (2005).

[7] S. Strauf and M. T. Rakher and I. Carmeli and K. Hennessy and C. Meier and A. Badolato and M. J. A. DeDood and P. M. Petroff and E. L. Hu and E. G. Gwinn

and D. Bouwmeester, "Frequency control of photonic crystal membrane resonators by monolayer deposition," Applied Physics Letters, **88**(4), 043116 (2006).

[8] H. S. Lee, S. Kiravittaya, S. Kumar, J. D. Plumhof, L. Balet, L. H. Li, M. Francardi, A. Gerardino, A. Fiore, A. Rastelli, and O. G. Schmidt, "Local tuning of photonic crystal nanocavity modes by laser-assisted oxidation," Applied Physics Letters, **95**(19), 191109 (2009).

[9] M.-K. Seo, H.-G. Park, J.-K. Yang, J.-Y. Kim, S.-H. Kim, and Y.-H. Lee, "Controlled sub-nanometer tuning of photonic crystal resonator by carbonaceous nano-dots," Optics Express, **16**(13), 9829-9837 (2008).

[10] A. Faraon, D. Englund, D. Bulla, B. Luther-Davies, B. J. Eggleton, N. Stoltz, P. Petroff, and J. Vuckovic, "Local tuning of photonic crystal cavities using chalcogenide glasses," Applied Physics Letters, **92**(4), 043123 (2008).

[11] M. W. Lee, C. Grillet, S. Tomljenovic-Hanic, E. C. Magi, D. J. Moss, B. J. Eggleton, X. Gai, S. Madden, D.-Y. Choi, D. A. P. Bulla, and B. Luther-Davies, "Photowritten high-Q cavities in two-dimensional chalcogenide glass photonic crystals," Optics Letters, **34,** 3671-3673 (2009).

[12] K. Hennessy and C. Högerle and E. Hu and A. Badolato and A. Imamoğlu, "Tuning photonic nanocavities by atomic force microscope nano-oxidation," Applied Physics Letters, **89**(4), 041118 (2006).

[13] C. W. Wong, P. T. Rakich, S. G. Johnson, M. Qi, H. I. Smith, E. P. Ippen, L. C. Kimerling, Y. Jeon, G. Barbastathis, and S.-G. Kim, "Strain-tunable silicon photonic band gap microcavities in optical waveguides," Applied Physics Letters, **84**(8), 1242-1244 (2004).

[14] J. Pan, Y. Huo, K. Yamanaka, S. Sandhu, L. Scaccabarozzi, R. Timp, M. L. Povinelli, S. Fan, M. M. Fejer, and J. S. Harris, "Aligning microcavity resonances in silicon photonic-crystal slabs using laser-pumped thermal tuning," Applied Physics Letters **92**(10), 103114 (2008).

[15] F. Micheli and I. W. Boyd, ”Photon-controlled oxidation of silicon,” Applied Physics Letters, **51**(15), 1149-1151 (1987).

[16] M. Huber, R. A. Deutschmann, R. Neumann, K. Brunner, and G. Abstreiter, ”Local laser induced rapid thermal oxidation of SOI substrates,” Applied Surface Science, **168**(1-4), 204-207 (2000).

[17] R. A. Deutschmann, M. Huber, R. Neumann, K. Brunner, and G. Abstreiter, ”Direct sub-μm lateral patterning of SOI by focused laser beam induced oxidation,” Microelectronic Engineering, **48**(1-4), 367-370 (1999).

[18] Y. S. Ju and K. E. Goodson, ”Phonon scattering in silicon films with thickness of order 100 nm,” Applied Physics Letters, **74**(20), 3005-3007 (1999).

[19] C. J. Chen, C. A. Husko, I. Meric, K. L. Shepard, C. W. Wong, W. M. J. Green, Y. A. Vlasov, and S. Assefa, ”Deterministic tuning of slow-light in photonic-crystal waveguides through the C and L bands by atomic layer deposition,” Applied Physics Letters, **96**(8), 081107 (2010).

[20] M. W. Lee, C. Grillet, C. L. C. Smith, D. J. Moss, B. J. Eggleton, D. Freeman, B. Luther-Davies, S. Madden, A. Rode, Y. Ruan, and Y.-H. Lee, ”Photosensitive post tuning of chalcogenide photonic crystal waveguides,” Optics Express, **15**(3), 1277-1285 (2007).

[21] Y. A. Vlasov and S. J. McNab, ”Coupling into the slow light mode in slab-type photonic crystal waveguides,” Optics Letters, **31**(1), 50-52 (2006).

[22] R. Chatterjee, N. C. Panoiu, K. Liu, Z. Dios, M. B. Yu, M. T. Doan, L. J. Kaufman, R. M. Osgood, and C. W. Wong, ”Achieving subdiffraction imaging through bound surface states in negative refraction photonic crystals in the near-infrared range,” Physical Review Letters, **100,** 187401 (2008).

[23] B. E. Deal and A. S. Grove, ”General relationship for the thermal oxidation of silicon,” Journal of Applied Physics, **36**(12), 3770-3778 (1965).

[24] H. R. Shanks, P. D. Maycock, P. H. Sidles, and G. C. Danielson, "Thermal conductivity of silicon from 300 to 1400 K," Physical Review, **130,** 1743-1748 (1963).

[25] M. Asheghi, M. N. Touzelbaev, K. E. Goodson, Y. K. Leung, and S. S. Wong, "Temperature-dependent thermal conductivity of single-crystal silicon layers in SOI substrates," Journal of Heat Transfer, **120**(1), 30-36 (1998).

[26] R. K. Iler, The Chemistry of Silica: Solubility, Polymerization, Colloid and Surface Properties, and Biochemistry. Wiley (1979).

[27] J. D. Le Grange, J. L . Markham, and C. R. Kurkjian, "Effects of surface hydration on the deposition of silane monolayers on silica," Langmuir, **9,** 1749-1753 (1993).

[28] N. D. Rooij, R. Sieverdink, and R. Tromp, "An investigation of the hydration properties of chemically vapour deposited silicon dioxide films by means of ellipsometry," Thin Solid Films, **47**(3), 211–218 (1977).

[29] G. Aygun, E. Atanassova, R. Turan, and T. Babeva, "Reflectance spectra and refractive index of a Nd:YAG laser-oxidized Si surface," Materials Chemistry and Physics, **89**(2-3), 316-320 (2005).

[30] H. Z. Massoud, J. D. Plummer, and E. A. Irene, "Thermal oxidation of silicon in dry oxygen: Growth-rate enhancement in the thin regime," Journal of Electrochemical Society, **132**(11), 2693-2700 (1985).

[31] Y. Enta, B. S. Mun, M. Rossi, J. Philip N. Ross, Z. Hussain, C. S. Fadley, K.-S. Lee, and S.-K. Kim, "Real-time observation of the dry oxidation of the Si(100) surface with ambient pressure x-ray photoelectron spectroscopy," Applied Physics Letters, **92**(1), 012110 (2008).

[32] E. Liarokapis, and Y. S. Raptis, "Temperature rise induced by a cw laser beam revisited," Journal of Applied Physics **57**, 5123 (1985).

[33] G. E. Jellison, Jr., and F. A. Modine, "Optical absorption of silicon between 1.6 and 4.7 eV at elevated temperatures," Applied Physics Letters **41**, 180 (1982).

[34] M. S. Aubain, and P. R. Bandaru, "In-plane thermal conductivity determination in silicon on insulator (SOI) structures through thermoreflectance measurements," in *Materials Research Society Symposium Proceedings,* (MRS Spring Meeting, San Francisco, CA 2010), p. 1267-DD12-01.

[35] D. Song, and G. Chen, "Thermal conductivity of periodic microporous silicon films," Applied Physics Letters **84**, 687 (2004).

[36] P. E. Hopkins, P. T. Rakich, R. H. Olsson, I. F. El-Kady, and L. M. Phinney, "Origin of reduction in phonon thermal conductivity of microporous solids," Applied Physics Letters **95**, 161902 (2009).

[37] P. E. Hopkins, C. M. Reinke, M. F. Su, R. H. Olsson III, E. A. Shaner, Z. C. Leseman, J. R. Serrano, L. M. Phiney, and I. El-Kady, "Reduction in the thermal conductivity of single crystalline silicon by phononic crystal patterning," Nano Letters **11**, 107 (2011).

[38] A. F. Oskooi, D. Roundy, M. Ibanescu, P. Bermel, J. D. Joannopoulos, and S. G. Johnson, "MEEP: A flexible free-software package for electromagnetic simulations by the FDTD method," Computer Physics Communications **181**, 687 (2010).

[39] H. Hagino, Y. Takahashi, Y. Tanaka, T. Asano, and S. Noda, "Effects of fluctuations in air hole radii and positions on optical characteristics in photonic heterostructure nanocavities," Physical Review B **79**, 085112 (2009).

Chapter 3

Atomic Layer Deposition Resonance Tuning

3.1 Introduction

Two-dimensional 2D PhC slabs confine light by Bragg reflection in-plane and total internal reflection in the third dimension. Introduction of point and line defects into 2D PhC slabs create localized resonant cavities and PhC waveguides respectively, with full control of dispersion ab initio. Such defect cavities in high-index contrast materials, such as monolithic silicon, possess strong confinement with subwavelength modal volumes (V_m) at $\sim (\lambda/n)^3$, corresponding to high field intensities per photon for increased nonlinear and nonclassical interactions. Moreover, photonic crystal cavities with remarkable high quality factors (Q) [1, 2] have been achieved recently, now permitting nanosecond photon lifetimes for enhanced light-matter interactions. The strong localization and long photon lifetimes in these high-Q/V_m photonic crystal nanocavities are strong candidates for enhanced nonlinear optical physics, such as optical bistability [3, 4, 5] and Raman lasing [6, 7], and cavity quantum electrodynamics [8].

These applications require precise control of cavity resonances to achieve tuned spectral overlap between the cavity modes and the gain or emitter material for controlled light-matter interactions. The cavity resonances is strongly dependent on the fabricated lattice constant a and the hole radius r of photonic crystals; slight differences in the photonic crystal geometries will result in large differences (a few to tens of nanometers in wavelength) in the dispersion characteristics. Active tuning using thermal (with associated phonon broadening of quantum dots) [9] or piezoelectric effects [10] can be employed. A passive post-fabrication tuning mechanism is particularly demanded, without external input power, to precisely align the designed resonant wavelengths. Specifically, wet chemical digital etching techniques [11] were recently developed for GaAs photonic crystal nanocavities, where the controlled blue shift of the cavity resonance was around 2-3 nm/cycle. Additionally, condensation of Xe [12] or self-assembled monolayers (such as a 2-nm polypeptide monolayer) [13] can be used, where a 3-5 nm cavity red shift per monolayer was observed for the latter. To achieve hundreds of picometer cavity resonance tuning, thin films below one nanometer is needed to be etched or deposited.

Atomic layer deposition (ALD) is widely used for gate dielectric and capacitance memory applications due to its high dielectric constant, precise thickness control, and highly

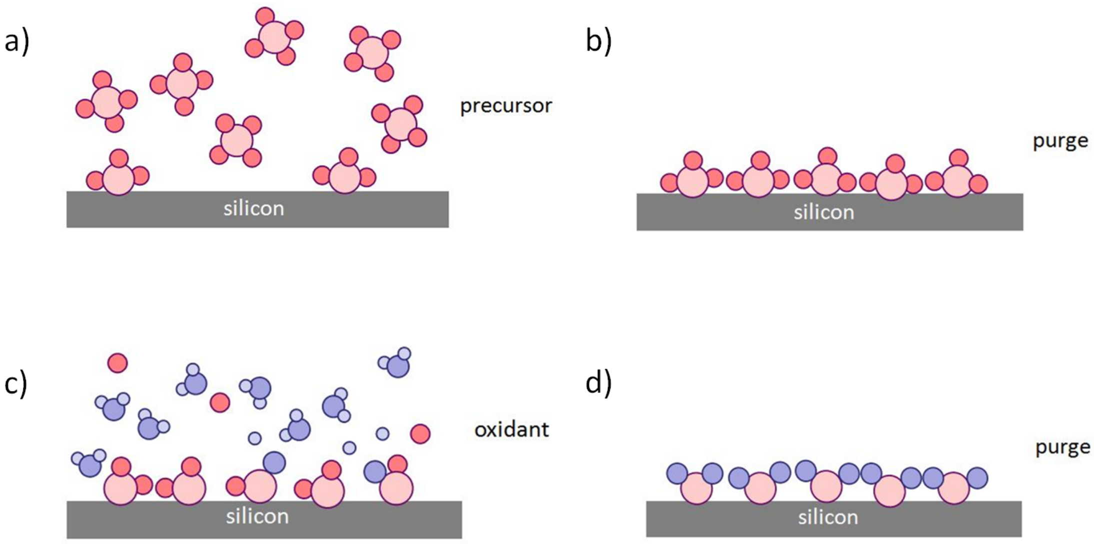

Figure 3.1: Steps in the ALD process involved in depositing a single monolayer of HfO_2. (a) A pulse of $Hg(DEA)_4$ precursor flows into chamber. (b) Unreacted $Hg(DEA)_4$ precursor is flushed out of chamber. (c) A pulse of oxidant flows into the chamber. (d) Unreacted oxidant is flushed out of chamber.

conformal properties. Several metal oxides such as aluminum oxide (Al_2O_3), hafnium oxide (HfO_2), and titanium dioxide (TiO_2) have been used in low temperature ALD thin film growth. All these materials have been widely used in optical coating applications with relatively high refractive indices (at 1.55 μm, n = 1.88 for HfO_2 [14], n = 1.57 for Al_2O_3 [15], and n = 2.18 for TiO_2 [16]) and a wide band gap with low absorption from the near-ultraviolet to the mid-infrared. Recently, ALD has become a promising tool for the fabrication of high quality three-dimensional photonic crystals from inorganic (opal) and organic (patterned polymer) templates [17, 18, 19, 20]. Photonic band structure tuning in a 2D periodic lattice was also demonstrated, with 12% tuning range and 0.005% precision based on a deposition rate of 0.51 Å TiO_2 per ALD cycle [21].

Here we investigated the post-fabrication digital resonance tuning of high-Q/V$_m$ silicon photonic crystal nanocavities using self-limiting atomic layer deposition of HfO_2. The vertical radiation from the top of the nanocavities was collected to analyze the mode resonances after each conformal coating step with slightly decreased r/a and increased t/a ratios in air-bridged photonic crystal slabs. The results demonstrate wide tuning range and precise fine control of cavity resonances while preserving high quality factors. The observed deposition rate is around 0.93 Å HfO_2 per ALD cycle, which leads to the red shift of resonant wavelength with precision of 122 ± 18 pm for a resonant wavelength ~ 1.55 μm. Total resonant wavelength tuning range is around 17 nm and currently only limited by the number of deposition steps (7 steps which is equivalent to 140 ALD cycles) used in this study.

3.2 Design and Fabrication

The structure investigated is an air-bridged triangular lattice photonic crystal slab with silicon membrane thickness of 190 nm ($t/a = 0.4524$) and air holes radii of 90 nm ($r/a = 0.2143$), where the lattice period $a = 420$ nm. High-Q/V_m nanocavities with five linearly aligned missing air holes (L5) are side coupled with photonic crystal waveguides, as shown in Figure 3.3(a). The shift S1 of two air-holes at cavity edge is 0.02a, 0.06a and 0.10a, respectively, for three different L5 nanocavities studied, in order to tune the radiation mode pattern for increasing the Q factors. The waveguide-to-cavity separation is five layers of holes. The devices were initially patterned with deep UV lithography at the Institute of Microelectronics in Singapore, and subsequently etched with SF_6/C_4F_8-based inductively coupled plasma (ICP) into the silicon-on-insulator substrate.

Post-fabrication processing to air-bridge the test chip was done at the Columbia University cleanroom. It was shown that the post-fabricaton processes used effected the quality of the ALD film later deposited. Fig. 3.2 shows a comparison between our initial process which had poor surface quality and improved process with better surface quality. We concluded that the high surface roughness in Figs. 3.2 (a) and (c) was at least partially related to the critical point drying (CPD) procedure. Optimal results involved no CPD, a lower ALD processing temperature (150°C) and processing steps as follows. Optical lithography with AZ4620 photoresist was used to open a window in photonic crystal region, and 10 minutes HF BOE (6:1) was used to release the air-bridged structures. Samples were then cleaned using Piranha (H_2SO_4:H_2O_2 3:1) solution for 5 minutes followed by HF BOE (6:1) solution dip for 30 seconds and deionized water rinse. Hot methanol was used as the final rinsing liquid to prevent stiction due to its lower surface tension. This procedure results in ∼ 6 Å of (O-H)-terminated silicon oxide on the surface of silicon air-bridged photonic crystal slabs [22]. All samples were exposed to UV generated ozone for 10 minutes to restore the hydrophilic character of surface immediately prior to HfO_2 deposition. Figure 3.3(a) shows the top-view scanning electron microscopy (SEM) image of air-bridged L5 cavity with S1 = 0.02a before ALD. Figure 3.5(a) shows the electric field E_y of the resonance mode mid-slab from 3D finite-difference time-domain simulations, calculated using a freely available software package with subpixel smoothing for increased accuracy [23].

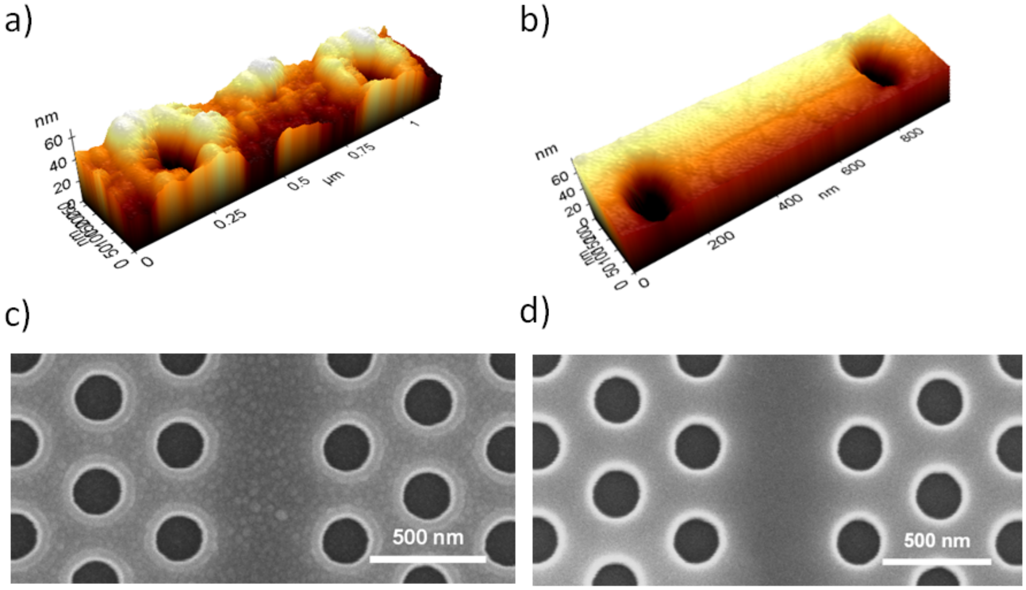

Figure 3.2: ALD surface quality resulting from different post-fabrication processes. AFM images of ALD surface resulting from (a) initial post-fabrication method and (b) modified post-fabrication method. SEM images of ALD surface resulting from (c) initial post-fabrication method and (d) modified post-fabrication method.

Thin films of amorphous HfO_2 are deposited conformally on silicon air-bridged photonic crystal slabs by means of ALD at 150°C. A lower substrate temperature down to 90°C is also possible with our machine, but at the expense of slow deposition rates. Films were deposited using tetrakis (diethylamido) hafnium (IV) $[Hf(DEA)_4]$ and water (H_2O) vapor

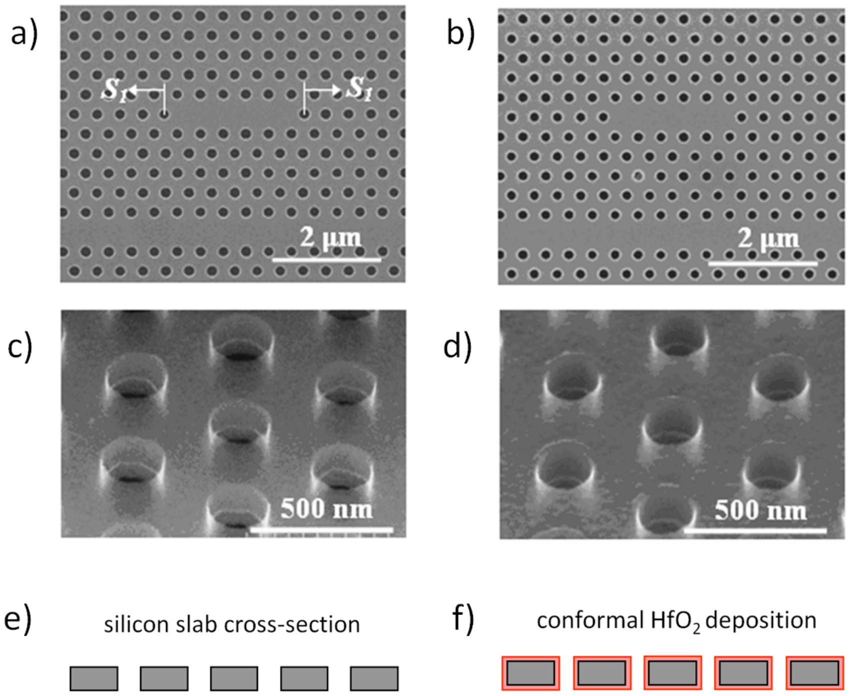

Figure 3.3: Top-view SEM images of airbridged L5 nanocavity (a) before ALD (b) after 140 ALD cycles of HfO2 (c) angled view before ALD (d) angled view after ALD (e) schematic of PhC cross-section before ALD (f) cross-section after ALD

in alternating pulses with N_2 purge of the reaction chamber between pulses. The process is self-limiting because the chemistry only allows one monolayer to form during each ALD cycle. The steps involved in one ALD cycle is shown in Fig. 3.1. In Fig. 3.1 (a) $Hf(DEA)_4$ is injected into the chamber with a 0.25 seconds long pulse. The precursor reacts with the hydrophillic surface resulting in a single layer of Hafnium. Next, N_2 is used to purged the ALD chamber for 150 seconds. In Fig. 3.1 (c) H_2O vapor is injected into the chamber with a 0.02 second pulse. It reacts with the chip surface to create a single layer of oxygen terminated bonds on top of the hafnium. Next, a 200 second N_2 purge removes the excess oxidant from the chamber. This completes one cycle. The next cycle follows the exact same steps. Using SEM analysis (averaged over a large number of cycles) our observed linear deposition rate is around 0.93 Å per cycle, which is about a monolayer of hafnium oxide.

We define a deposition step to be the number of ALD cycles performed before the test sample is removed from the chamber for optical measurements. We chose our deposition step to be 20 ALD cycles. Figure 3.3(b) shows a top-down SEM image of a L5 cavity after seven deposition steps, with the same magnification as in Figure 3.3(a). Based on geometrical statistical analysis of high-resolution SEM images, the hole radius reduces from 92.8 ± 1.6 nm to 79.9 ± 2.7 nm [24]. Figure 3.3(c) and 3.3(d) are the angled SEM images of air-bridged photonic crystal slabs before ALD and after seven deposition steps, respectively. The surface is still smooth enough to support high-Q modes for L5 nanocavities after HfO_2 deposition. The thickness of photonic crystal slabs increases from 190 nm to 216 nm based on SEM estimates. These geometry changes agree well with the deposition schematic cross section of the sample morphology drawn in Figures 3.3(e) and (f).

With slightly decreased r/a and increased t/a ratios in air-bridged photonic crystal slabs, the photonic band gap will shift to lower frequencies. In addition to a frequency shift, the photonic bandgap also decreases from an 11.4% to a 9.7% gap with a deposition of HfO_2 as computed using a freely available software package [25]. This can be attributed to a lower-index contrast between the holes and the bulk dielectric. The resonant wavelength of L5 nanocavities will undergo a redshift.

3.3 Experimental Setup

For the measurement setup, a polarization controller and a lensed fiber are used to couple transverse-electric (TE) polarization light from tunable laser source (1480-1580 nm, wavelength accuracy 10 pm with 200 kHz linewidth) into the waveguide. A second lensed fiber collects the transmission from the waveguide output to check the total transmission loss of the whole system, which is around 24.8 dBm at wavelength of 1550 nm. The vertical radiation from the top of nanocavities collected by a 40X objective lens (NA of 0.65) and a 4X telescope was sent to the photodetector and lock-in amplifier to analyze the cavity resonances. In order to exclude optical nonlinear effects, low input power of 10 μW was coupled to the waveguide. Figure 3.5(e) plots the measured cavity resonances after each deposition step for L5 cavity with S1 = 0.02a. The quality factor Q is estimated from the full-width at half maximum and is $\sim$ 49,000. From the 3D FDTD method, the Q factor

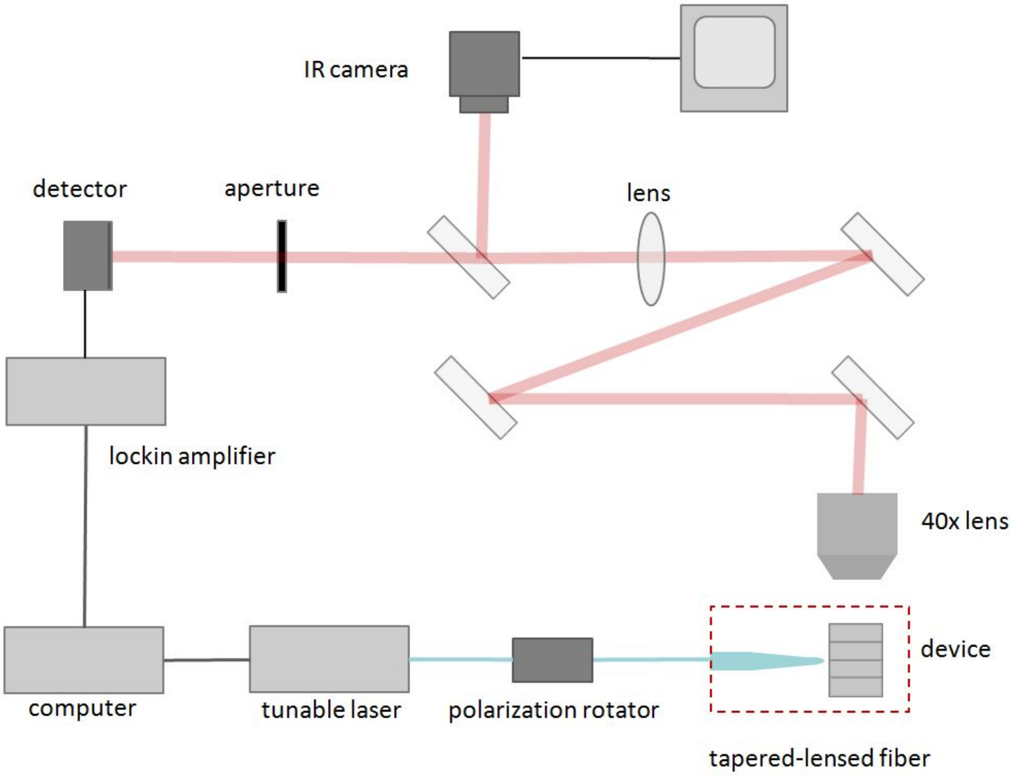

Figure 3.4: Test setup for taking radiation measurements from on-chip PhC nanocavity devices.

and modal volume are calculated around 50,000 and $\sim$ 0.98 cubic wavelengths ($(\lambda/n)^3$) respectively.

3.4 Cavity Resonance Tuning

Figure 3.5(a) shows how the tuned resonant wavelength scales linearly with the number of deposition steps for all three L5 cavities under investigation. Total resonant wavelength tuning range is around 17 nm with the current 7 deposition steps. With more deposition steps, wider tuning range can be obtained. The 3D FDTD simulations (inset of Figure 3.5(a)) show a linear shift in the resonant wavelength as expected from small perturbations, although there is more uncertainty in the simulations due to the high spatial resolution ($\sim$ a few nanometers or less) required to capture this digital tuning. Figure 3.5(b) plots the resonant wavelength increment for each deposition step. An average wavelength red shift of 2.4 ± 0.4 nm is obtained for each step, which corresponds to a resonance shift of 122 ± 18 pm per HfO_2 monolayer deposition. An oscillatory variation of the resonance shift is also observed, as shown in Figure 3.5(b). This could be due to variations in the film deposition thickness, which is not exactly the same in each step. In addition, we observe that the resonance increment itself increases slightly from 2.2 nm to 2.7 nm based on the linear curve fit. This is because, due to the conformality of ALD process, more dielectric material will be added relative to the previous step due to the expanded surface area, so that the resonance increment also slightly goes up, as illustrated in deposition schematics in Figure 3.3(f).

With different deposition material, the precision of the resonant wavelength shift per ALD cycle can be changed. Single monolayer of HfO_2 induces an average 122 pm shift ($n = 1.88$ at 1.55 μm, 0.93 Å per ALD cycle at 150 °C). From first-order perturbation estimate, a monolayer of TiO2 ($n = 2.18$ at 1.55 μm, 0.5 Å per ALD cycle at 100 °C [16]) can induce approximately 54 pm shift, while a monolayer of Al_2O_3 ($n = 1.57$ at 1.55 μm, 1 Å per ALD cycle at 100 °C [15]) can generate approximately a 158 pm wavelength shift.

Figure 3.5(d) illustrates the variation of quality factor Q with the number of deposition steps for all three L5 cavities. After the first deposition step, Q values drop almost by half for

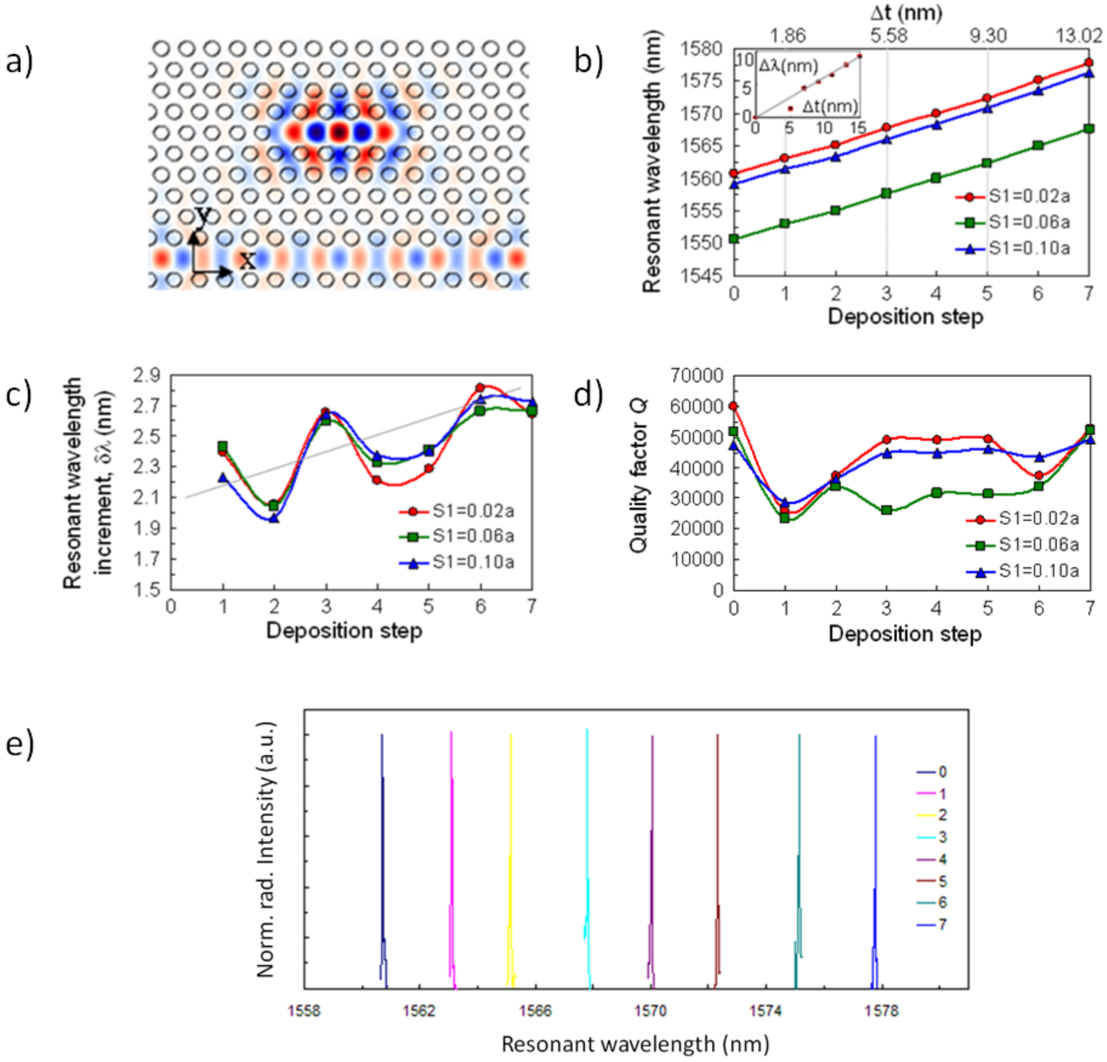

Figure 3.5: (a) FDTD calculated electric field E_y profile of the high-Q mode supported in the L5 nanocavity. (b) The tuned resonant wavelength scales linearly with the number of deposition step for all three L5 cavities under investigation. Inset: 3D FDTD calculated wavelength shift (Δλ) for increasing thicknesses (Δt) of HfO_2 deposited for all three cavities studied. (c) The wavelength increment $\delta\lambda$ for each deposition step. (d) The variation of the quality factor Q with the number of deposition steps for all three L5 cavities. (e) Measured cavity resonances after each deposition step ("1" to "7" in legend; "0" is unperturbed) for L5 cavity with S_1=0.02a.

all cavities. This is because the ALD deposited film has a larger roughness initially, leading to more surface and air hole sidewall roughness scattering. The larger roughness is caused by the formation of an interfacial layer between the Si and HfO_2 layers. With subsequent deposition steps, the conformal deposition gives a smoother film surface, permitting the Q values to recover back to almost their initial values. The Q values always maintain at least 20,000 or more during the deposition steps; this characteristic is also observed in our 3D FDTD simulations. This demonstrated shift in the resonance, while preserving the cavity Q, in response to a monolayer deposition also suggests these cavities as possible integrated sensors with pronounced responsivity to environmental conditions.

3.5 Selective Tuning

The ALD tuning process previously described is a global process, i.e. it affects the entire chip simultaneously. This is a useful tool for correcting a uniform wafer-wide fabrication errors. But other fabrication errors require more localized tuning. We have proposed and investigated a selective ALD process can be used to tune individual cavities or regions without perturbing nearby structures. The process is described in Fig. 3.6 (a). We first start with chip which has already been airbridged. Because of this, extra precautions must be taken to avoid damaging the delicate Si PhC membrane. First the chip is carefully cleaned acetone, isopropanol and water. In order to prevent damage to the delicate suspended membrane, the chip should not be allowed to dry during the cleaning process. The chip should be placed in methanol heated on a hotplate at $\sim 80 \circ C$ before being allowed to dry in air on the hot plate. Next PMMA e-beam resist is spin-coated onto the chip. The areas to be tuned are patterned using e-beam lithography and carefully developed, once again ensuring there is minimal surface tension during drying. Next the ALD is used to deposit discrete monolayers of HfO_2 using the process described earlier in this chapter. Finally, the PMMA is removed in acetone. Note that possible alternatives to e-beam patterning include direct-write laser patterning and photolithography.

Fig. 3.6 (b), demonstrates how selective ALD tuning can be used for cavity resonance matching, which is important for fields such as the optical analogue to electromagnetically-induced transparency (EIT) and cavity quantum-electrodynamics(QED). The resonance of the cavity on the right has been digitally tuned by ∼ 2 nm to match the resonance of the cavity on the left. The cavity resonance can be tuned by even finer increments by patterning a small sub-cavity sized region for selective ALD deposition as shown in Fig. 3.7. Due to the smaller index perturbation the resonance tuning increment of a single monolayer will also decrease.

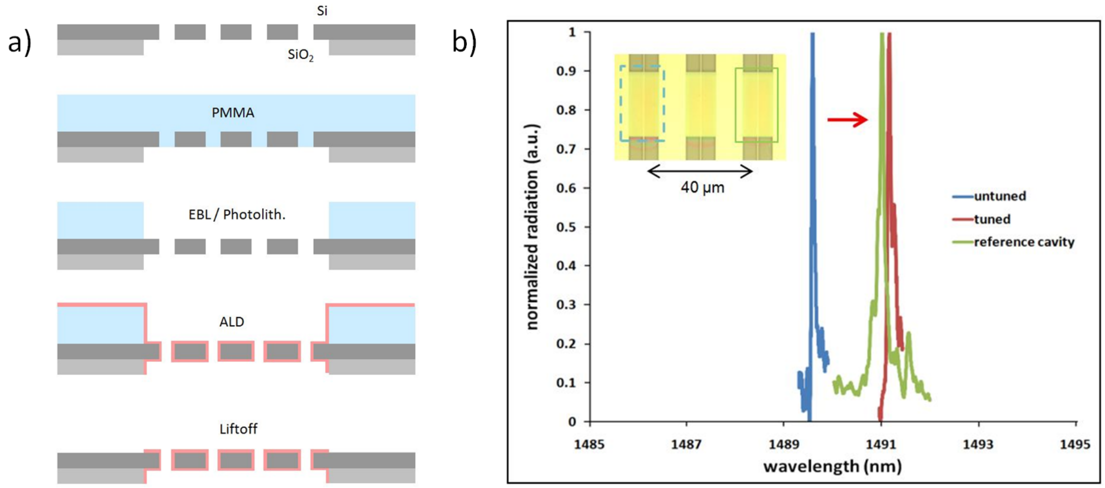

Figure 3.6: Selective ALD (a) process steps (b) selective resonance tuning of a single high-Q cavity. Inset: the left cavity is tuned while the right cavity is unperturbed

3.6 Conclusions

In summary, we have developed a technique for fine tuning the resonant wavelengths of high-Q/Vm silicon photonic crystal nanocavities digitally using ALD of HfO_2 monolayers. The results demonstrate a nearly linear tuning across a range of around 17 nm. The tuning range is currently limited only by the number of deposition steps used in this study. The tuning precision is 122 ± 18 pm per ALD cycle while preserving high quality factors of resonant modes in L5 photonic crystal nanocavities. With selective patterning, HfO_2 monolayers can be selectively deposited only within the nanocavity region using low-temperature ALD [26] for even finer tuning control. The highly controlled, digital tuning of high-Q modes

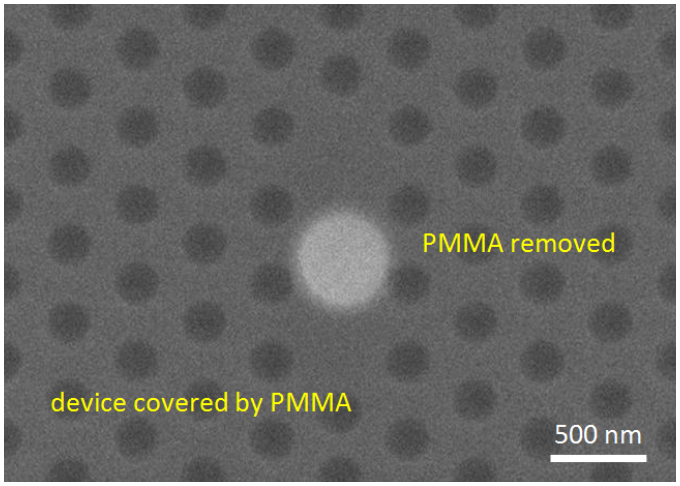

Figure 3.7: SEM image of L3 nanocavity coated with PMMA. A 250 nm diameter hole has been patterned in the center of the cavity for selective ALD tuning.

in silicon photonic crystal nanocavities allows for practical realization of optical devices involving multiple resonances and matching transitions between quantum dots and optical resonances for cavity quantum electrodynamics.

3.7 Acknowledgements

This work was done in collaboration with Xiaodong Yang, another graduate student in our group, at the Columbia Optical Nanostructures Laboratory. Chip fabrication was performed at the Institute of Microelectronics in Singapore by Mingbin Yu and Dim-Lee Kwong. Post-fabrication air-bridging and ALD deposition were performed in the Columbia University cleanroom. Chad Husko performed some of the FDTD simulations. We were also aided by Inanc Meric, a graduate student from Prof. Shepard's group in the Electrical Engineering department, who had prior experience with hafnium oxide (HfO_2) atomic layer deposition.

Bibliography

[1] B. Song, S. Noda, T. Asano, and Y. Akahane, "Ultra-high-Q photonic double-heterostructure nanocavity," *Nature Materials*, vol. 4, pp. 207–210, Mar. 2005.

[2] E. Kuramochi, M. Notomi, S. Mitsugi, A. Shinya, T. Tanabe, and T. Watanabe, "Ultrahigh-Q photonic crystal nanocavities realized by the local width modulation of a line defect," *Applied Physics Letters*, vol. 88, no. 4, p. 041112, 2006.

[3] P. Barclay, K. Srinivasan, and O. Painter, "Nonlinear response of silicon photonic crystal microresonators excited via an integrated waveguide and fiber taper," *Optics Express*, vol. 13, no. 3, pp. 801–820, 2005.

[4] T. Tanabe, M. Notomi, S. Mitsugi, A. Shinya, and E. Kuramochi, "All-optical switches on a silicon chip realized using photonic crystal nanocavities," *Applied Physics Letters*, vol. 87, no. 15, p. 151112, 2005.

[5] X. Yang, C. Husko, C. W. Wong, M. Yu, and D.-L. Kwong, "Observation of femtojoule optical bistability involving fano resonances in high-Q/V$_m$ silicon photonic crystal nanocavities," *Applied Physics Letters*, vol. 91, no. 5, p. 051113, 2007.

[6] H. Rong, S. Xu, Y. Kuo, V. Sih, O. Cohen, O. Raday, and M. Paniccia, "Low-threshold continuous-wave Raman silicon laser," *Nature Photonics*, vol. 1, pp. 232–237, Apr. 2007.

[7] X. Yang and C. W. Wong, "Coupled-mode theory for stimulated raman scattering in high-Q/V$_m$ silicon photonic band gap defect cavity lasers," *Optics Express*, vol. 15, no. 8, pp. 4763–4780, 2007.

[8] R. Bose, X. Yang, R. Chatterjee, J. Gao, and C. W. Wong, “Weak coupling interactions of colloidal lead sulphide nanocrystals with silicon photonic crystal nanocavities near 1.55 μm at room temperature,” *Applied Physics Letters*, vol. 90, no. 11, p. 111117, 2007.

[9] E. Peter, P. Senellart, D. Martrou, A. Lemaître, J. Hours, J. M. Gérard, and J. Bloch, “Exciton-photon strong-coupling regime for a single quantum dot embedded in a microcavity,” *Physical Review Letters*, vol. 95, p. 067401, Aug 2005.

[10] C. W. Wong, P. T. Rakich, S. G. Johnson, M. Qi, H. I. Smith, E. P. Ippen, L. C. Kimerling, Y. Jeon, G. Barbastathis, and S.-G. Kim, “Strain-tunable silicon photonic band gap microcavities in optical waveguides,” *Applied Physics Letters*, vol. 84, no. 8, pp. 1242–1244, 2004.

[11] K. Hennessy, A. Badolato, A. Tamboli, P. M. Petroff, E. Hu, M. Atatüre, J. Dreiser, and A. Imamoğlu, “Tuning photonic crystal nanocavity modes by wet chemical digital etching,” *Applied Physics Letters*, vol. 87, no. 2, p. 021108, 2005.

[12] S. Mosor, J. Hendrickson, B. C. Richards, J. Sweet, G. Khitrova, H. M. Gibbs, T. Yoshie, A. Scherer, O. B. Shchekin, and D. G. Deppe, “Scanning a photonic crystal slab nanocavity by condensation of xenon,” *Applied Physics Letters*, vol. 87, no. 14, p. 141105, 2005.

[13] S. Strauf, M. T. Rakher, I. Carmeli, K. Hennessy, C. Meier, A. Badolato, M. J. A. DeDood, P. M. Petroff, E. L. Hu, E. G. Gwinn, and D. Bouwmeester, “Frequency control of photonic crystal membrane resonators by monolayer deposition,” *Applied Physics Letters*, vol. 88, no. 4, p. 043116, 2006.

[14] M. Al-Kuhaili, “Optical properties of hafnium oxide thin films and their application in energy-efficient windows,” *Optical Materials*, vol. 27, no. 3, pp. 383 – 387, 2004.

[15] T. S. Eriksson, A. Hjortsberg, G. A. Niklasson, and C. G. Granqvist, “Infrared optical properties of evaporated alumina films,” *Applied Optics*, vol. 20, no. 15, pp. 2742–2746, 1981.

[16] X. Wang, M. Fujimaki, and K. Awazu, "Photonic crystal structures in titanium dioxide (TiO_2) and their optimal design," *Optics Express*, vol. 13, no. 5, pp. 1486–1497, 2005.

[17] J. S. King, C. W. Neff, C. J. Summers, W. Park, S. Blomquist, E. Forsythe, and D. Morton, "High-filling-fraction inverted ZnS opals fabricated by atomic layer deposition," *Applied Physics Letters*, vol. 83, no. 13, pp. 2566–2568, 2003.

[18] A. Rugge, J. S. Becker, R. G. Gordon, and S. H. Tolbert, "Tungsten nitride inverse opals by atomic layer deposition," *Nano Letters*, vol. 3, no. 9, pp. 1293–1297, 2003.

[19] J.-H. Lee, W. Leung, J. Ahn, T. Lee, I.-S. Park, K. Constant, and K.-M. Ho, "Layer-by-layer photonic crystal fabricated by low-temperature atomic layer deposition," *Applied Physics Letters*, vol. 90, no. 15, p. 151101, 2007.

[20] J. Y. Huang, X. D. Wang, and Z. L. Wang, "Controlled replication of butterfly wings for achieving tunable photonic properties," *Nano Letters*, vol. 6, no. 10, pp. 2325–2331, 2006.

[21] E. Graugnard, D. P. Gaillot, S. N. Dunham, C. W. Neff, T. Yamashita, and C. J. Summers, "Photonic band tuning in two-dimensional photonic crystal slab waveguides by atomic layer deposition," *Applied Physics Letters*, vol. 89, no. 18, p. 181108, 2006.

[22] A. Deshpande, R. Inman, G. Jursich, and C. Takoudis, "Atomic layer deposition and characterization of hafnium oxide grown on silicon from tetrakis(diethylamino)hafnium and water vapor," *Journal of Vacuum Science & Technology A: Vacuum, Surfaces, and Films*, vol. 22, no. 5, pp. 2035–2040, 2004.

[23] A. Farjadpour, D. Roundy, A. Rodriguez, M. Ibanescu, P. Bermel, J. D. Joannopoulos, S. G. Johnson, and G. W. Burr, "Improving accuracy by subpixel smoothing in the finite-difference time domain," *Optics Letters*, vol. 31, no. 20, pp. 2972–2974, 2006.

[24] M. Skorobogatiy, G. Bégin, and A. Talneau, "Statistical analysis of geometrical imperfections from the images of 2D photonic crystals," *Optics Express*, vol. 13, no. 7, pp. 2487–2502, 2005.

[25] S. Johnson and J. Joannopoulos, “Block-iterative frequency-domain methods for maxwell’s equations in a planewave basis,” *Optics Express*, vol. 8, no. 3, pp. 173–190, 2001.

[26] M. J. Biercuk, D. J. Monsma, C. M. Marcus, J. S. Becker, and R. G. Gordon, “Low-temperature atomic-layer-deposition lift-off method for microelectronic and nanoelectronic applications,” *Applied Physics Letters*, vol. 83, no. 12, pp. 2405–2407, 2003.

Chapter 4

Atomic Layer Deposition Slow-Light Tuning

4.1 Overview

Dramatic reduction of the group-velocity of light has been demonstrated in atomic and solid-state systems [1, 2, 3, 4, 5]. This reduction is accompanied by a large increase in light-matter interaction, although typically at the expense of bandwidth. Slow-light in photonic-crystal (PhC) waveguides, through strong structural dispersion, allows larger bandwidth for potential applications such as optical buffering and switching [6, 7, 8, 9] , disordered localization [10, 11], and nonclassical optics [12, 13]. The dispersion-to-loss ratio [14] is comparable to that of single-mode optical fibers, allowing strong enhancement of nonlinear processes on the chip, such as third-harmonic generation, self-phase modulation, Raman and parametric processes [15, 16, 17, 18, 19]. However, in order to operate at a particular frequency, these devices often possess stringent fabrication requirements that are difficult to achieve using current e-beam or deep-UV lithography; even slight fabrication deviations at the nanometer level can shift the tight operating bandwidths of the integrated photonic devices [20]. Active approaches to tune photonic elements include aligned external pump laser beams [21], integrated piezoelectric elements [22] or micro-heaters [6]. To maintain the shifted dispersion or resonances in active tuning approaches, a finite external power must be continuously applied to the photonic elements. Alternatively, passive tuning approaches have been examined, such as GaAs wet-etching [23], nitrogen or Xe condensation in cryostats [24, 25], self-assembled polypeptide monolayers [26] and electron beam induced compaction [27]. Recently we examined an ALD approach to tune PhC microcavity resonances with a precision of $\sim$ 122 pm per hafnium oxide (HfO_2) layer [28]; additionally, the tuning of photonic bands in silicon-on-insulator slab PhC structures has also been examined with titanium dioxide deposition [29]. Here we propose and demonstrate for the first time a passive post-fabrication scheme for tuning dispersion in slow-light PhC waveguides by utilizing a digital self-limiting deposition of HfO_2 monolayers.

4.2 Experimental Setup

To study the effect of passive tuning of the slow-light regime, we designed PhC waveguides and Mach-Zehnder interferometer (MZI) devices for transmission measurements in the near-

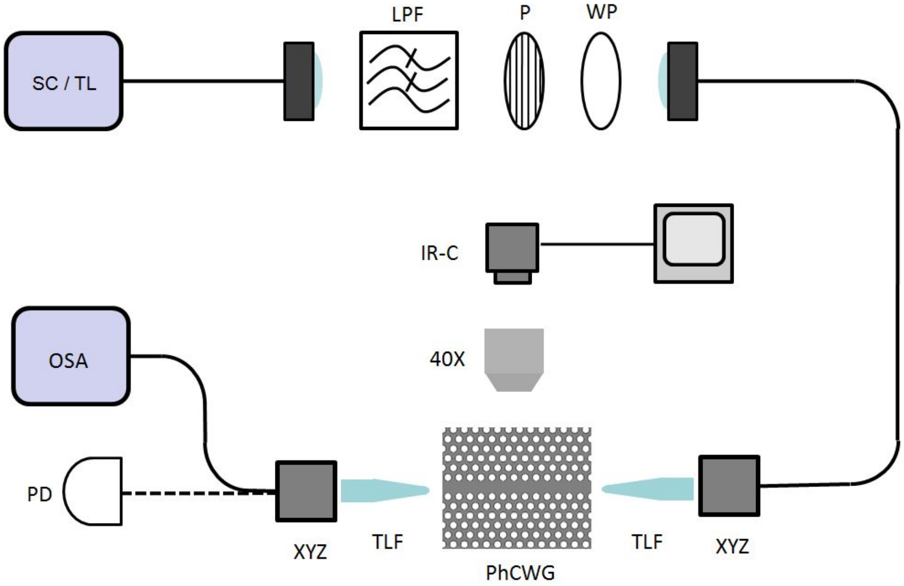

Figure 4.1: Test setup for ALD dispersion tuning studies. Polarization of light from the laser source (supercontinuum / tunable laser) is controlled by a polarizer and waveplate and coupled to the photonic crystal chip with a polarization maintaining lensed fiber. The output light is sent to a photodetector or optical spectrum analyzer. The chip is imaged with a 40X objective lens and IR camera.

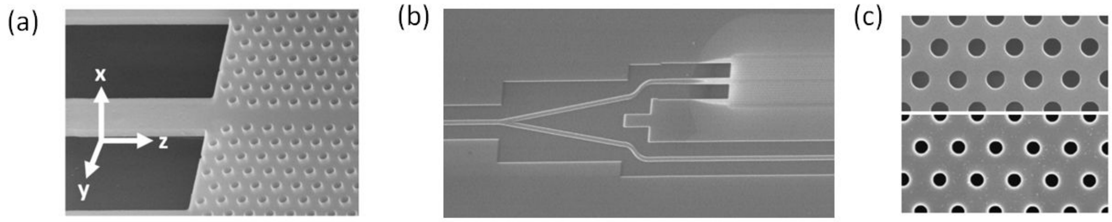

Figure 4.2: SEM image of (a) PhC waveguide and strip waveguide interface (b) MZI structure with PhC waveguide on upper section and strip waveguide on lower section. (c) PhC before deposition (upper image) and after 160 ALD layers of HfO_2.

infrared [6, 30]. Each MZI device consists of a Y-splitter connected to a strip waveguide on one arm and to a PhC waveguide on the other arm, as shown in Figure 4.2(b). The interference fringes from MZI spectral measurements are used to determine group-velocity using a procedure described below. The PhC waveguides are W0.9 line defects created by removing a single row of air holes in a hexagonal lattice of air holes along the Γ-K direction and then decreasing the defect width by 10%. The lattice parameter of the PhCs (a) is 410 nm with air hole radii of 108 nm (r/a ratio of 0.265). The structures were fabricated by e-beam lithography on SOI substrates with a silicon slab thickness of 220 nm (t/a ratio of 0.537). The PhC waveguide is 250 μm long and butt-coupled to strip waveguides at both ends, and has previously demonstrated low-loss of 2.4-dB/mm [22]. The underlying oxide was subsequently removed by HF etching. The silicon strip waveguides are tapered adiabatically as they connect to polymer couplers which are used for low-loss coupling to off-chip polarization-maintaining tapered-lensed fibers [31].

Figure 4.3(a) shows the projected band structure of our PhC waveguide, computed through 3D plane wave expansion [32]. In order to get the best fitting to experimental data a procedure described in reference [30] was used. Within the band gap, there are two TE-like modes (even and odd modes). The even mode exhibits slow-light characteristics near the band-edge where $d\omega/dk$ becomes increasingly small, resulting in large group indices, $n_g = c(dk/d\omega)$. The corresponding projected band structure for the TM-like mode is shown Figure 4.3(b) where, although no band gap exists, one observes a Bragg stop gap due to

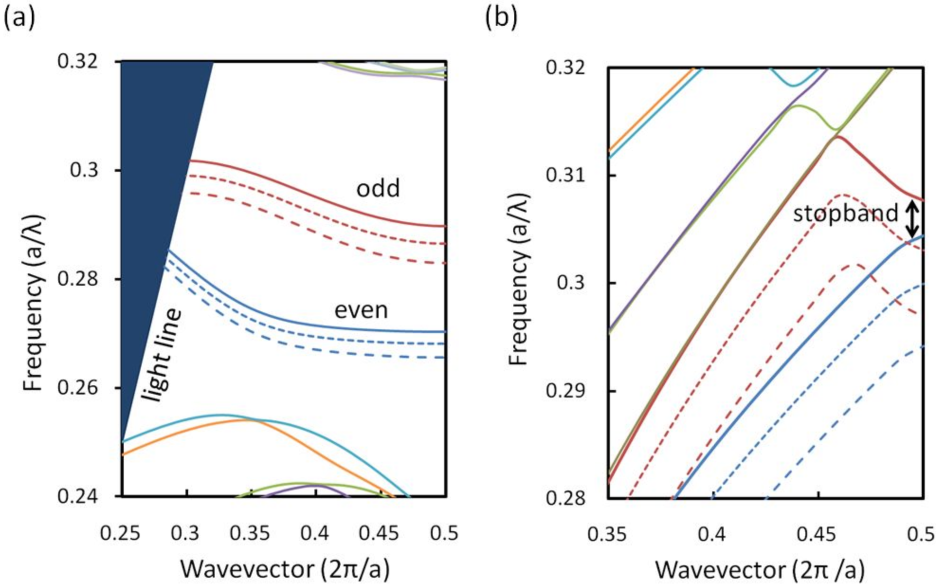

Figure 4.3: Band structures calculated using plane-wave expansion method. Solid-lines correspond to no HfO_2 deposition. Dotted-lines and dashed-lines correspond to 80 and 160 atomic layers of HfO_2 deposition, respectively. (a) Projected band diagram for TE-like W0.9 waveguide modes (b) Corresponding TM band diagram. Note that the vertical and horizontal ranges are different than in (a).

the periodic modulation of the effective index in the propagation direction [33].

4.3 Fabrication

In order to tune the structures, sequential conformal deposition of HfO_2 atomic layers was performed. HfO_2 was chosen as the ALD material due to its wide band gap, low optical absorption [34], and direct CMOS-compatibility having been used as a high-k dielectric gate insulator in the 45 nm technology node [35]. Prior to each deposition step, samples were cleaned with acetone, isopropanol and UV ozone. The UV generated ozone was used to create a hydrophilic surface favorable for the ALD process. Monolayer films were deposited at a temperature of 200 °C using two precursors, tetrakis(diethylamido)hafnium(IV) [Hf(DEA)4] and water (H_2O) vapor, in alternating pulses. Nitrogen gas was flowed through the reaction chamber during the entire process. Lower temperature depositions are also possible with the trade-off of longer deposition times. The process is self-limiting and deposits one atomic layer at a time, with deposition rate of approximately 0.1 nm per minute. As shown by the SEM image in Figure 4.2(c), the ALD deposited film is high quality and uniform even inside of the air holes. Because ALD is a conformal process, each cycle incrementally decreases the hole radii and increases the slab thickness. The increase in brightness around the hole after ALD deposition is due to charging effects in the HfO_2 during SEM imaging.

4.4 Slow Light Tuning

Digital tuning was performed in increments of 40 atomic layers, with 1.05 ± 0.05 Å thickness for each HfO_2 atomic layer [36]. After each of these deposition steps (40 atomic layers), transmission measurements were performed for both the TE and TM polarizations. Light from a supercontinuum source was coupled into the on-chip polymer couplers using a polarization-maintaining tapered-lensed fiber. The output from the chip was similarly coupled to a tapered-lensed fiber and measured with an optical spectrum analyzer in the spectral range of 1300 to 1600 nm. The measured transmission spectra were normalized by the transmission spectra through a reference strip waveguide.

Figure 4.4(a) shows a series of TE transmission spectra after sequential ALD deposition steps. A wide bandwidth transmission region extends across the lower wavelength range followed by a sudden drop in transmission around 1514 nm for the pre-deposition measurement. The slow-light regime, which is close to onset of the waveguiding mode, is characterized by high group-indices as shown in figure 4.5(a). We observed a deterministic red-shift in the slow-light TE-like mode onset edge from 1513.8 nm (before ALD tuning) to 1533.7 nm (after 160 ALD deposition cycles), with the slow-light edge determined by a 10-dB drop in transmission corresponding to a group index of approximately 40. The inset of Figure 4.5(a) illustrates that the red-shift is linear, with a 140 ± 10 pm per monolayer control of the slow-light mode onset edge. The initial deposition step was not used in calculating this value because the slow-light red-shift in the first deposition step was slightly smaller than subsequent deposition steps. This is likely due to the formation of an 8-10 Å interfacial layer between HfO_2 and silicon during the first 20 ALD deposition cycles [36, 37]. In addition, on a different chip we have also tuned the slow-light edge across the entire optical communications C-band (and into part of the L-band), with tuning from 1530.6 nm to 1597.8 nm with 450 ALD cycles, i.e. 150 ± 10 pm per monolayer.

Figure 4.4(b) shows a series of TM transmission spectra after sequential ALD deposition steps. Unlike the TE-like slow-light mode which is found in the TE band gap, the TM-like slow-light modes are found on either side of the stop gap (illustrated by the dashed-lines in the computed band structure of Figure 4.3(b)). The TM-like modes are also red-shifted with the ALD deposition. The red-shift for the shorter-wavelength TM slow-light mode is likewise linear with control from 1370.7 nm to 1403.5 with 160 ALD layers, or 250 ± 10 pm per monolayer. The larger TM shift is due to the larger modal area and overlap with the HfO_2 monolayers. In comparing the slow-light tuning of the TE and TM modes, we note that there is a differential shift of 110 ± 30 pm per monolayer. This difference can be used for exact tuning of the pump-Stokes frequency spacing, in order to match the optical phonons (15.6-THz) in single-crystal silicon, for cross-polarized Raman amplification [33].

Along with PhC waveguide transmission measurements, MZI transmission measurements were taken to determine group indices using a frequency-domain interferometric technique [6, 30]. The MZI structure is shown in Figure 4.2(b). The results of the measurements (over a total of 160 atomic layers) are summarized in Figure 4.5(a). The solid lines

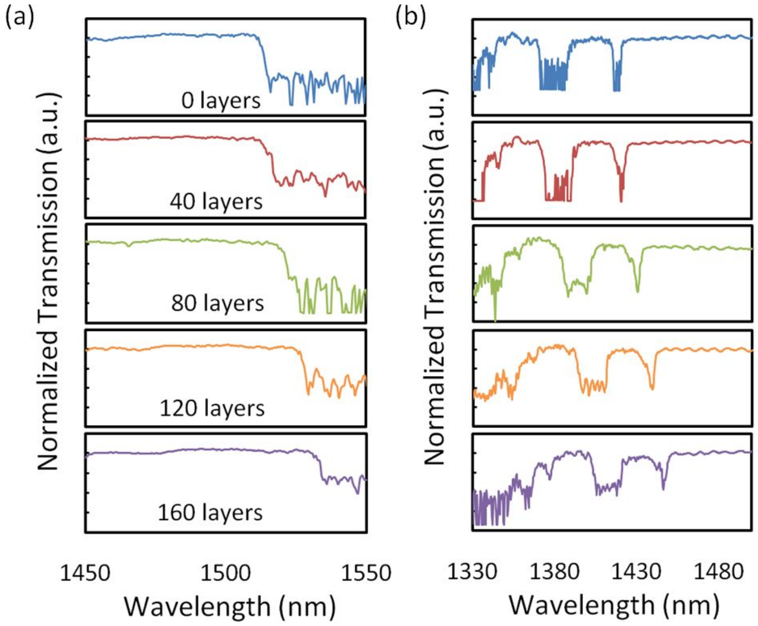

Figure 4.4: (a) TE transmission measurements for different ALD tuning steps. The different colors denote the various ALD layers. (b) Corresponding TM transmission measurements.

are from exponential fitting of group indices which were in-turn deduced from the spectral positions of minima and maxima in the MZI transmission with: $n_g(\lambda) = \lambda_{min}\ \lambda_{max}$ / $(2L(\lambda_{min}$ - λ_{max} $)+$ $n_g{}^{ref}$, where L is the PhC waveguide length [6]. Both before and after ALD controlled tuning, group indices of more than 60 were consistently obtained in our measurements.

4.5 Higher Order Dispersion

Higher order dispersion was also studied because of the important role it plays in pulse propagation in slow-light PhC waveguides [6, 38]. At low group-velocities there can be a significant increase in temporal pulse width and pulse shape asymmetry due to higher order dispersion [39]. We investigated the effects of ALD on higher order dispersion, particularly the group velocity dispersion (GVD; $\lambda^2/2\pi c)(\partial n_g/\partial\lambda)$ and third-order dispersion (TOD; $\lambda^2/2\pi c)(\partial(GVD)/\partial\lambda)$. The GVD and TOD results for the different ALD deposition steps are summarized in Fig. 4.5(b) and 4.5(c) respectively. The results show that the GVD and TOD do not change appreciably while the slow-light mode onset edge is deterministically tuned by ALD, with a variation of only 3% when determined from experimental group-index data which has been fitted. This small variation is not necessarily due to ALD tuning but can also originate in part from uncertainty in fitting the data.

4.6 Tuning Range

Figure 4.6 shows the slow-light TE-like mode onset edge is tuned across a wavelength range of approximately 20 nm, from 1513.8 nm to 1533.7 nm. On a separate chip, the slow-light edge has been tuned across a much wider wavelength range covering the entire optical communications C-band and part of the L-band using deposition steps of 150 atomic layers. This is shown in Figure 4.6. The slow-light edge is tuned from 1530.6 nm to 1597.8 nm with 450 atomic layers of HfO_2. On this chip, a smaller average red-shift per monolayer was also observed during an initial 20 monolayer deposition. This is likely due to the formation of an 8-10 Å interfacial layer between HfO_2 and silicon.

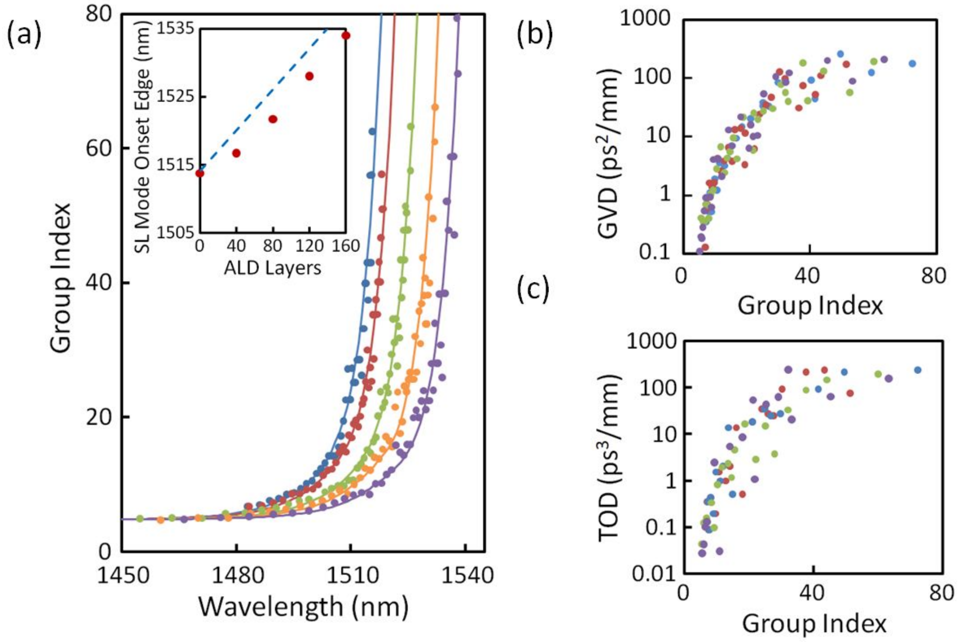

Figure 4.5: (a) Group-index measurements from MZI devices. The number of atomic layers deposited is indicated by the color of the circles. Refer to the color code described in Figure 3(a). The solid lines are provided for clarity. Inset: measured slow-light (SL) mode onset (red circles) and numerical simulations (blue dashed line). (b and c) Measured group-velocity dispersion and third-order dispersion for the different ALD tuning steps.

4.7 Propagation Losses

Surface roughness is recognized as a significant factor in PhC waveguide losses [40]. Previous work [41] using similar waveguides has demonstrated a decrease in propagation loss as the size of the hole is decreased, which is attributed to the smaller surface area which results in reduced scattering. Ultra-smooth ALD films have also been demonstrated to not significantly affect the quality factors of optical resonators [28]. Atomic force microscopy studies by Puthenkovilakam et al. [37] have confirmed deposited HfO_2 films can have a root-mean-square roughness as small as 2.7 Å, which is much smaller than the silicon sidewall roughness of the PhC structures as fabricated [42]. If extra surface roughness was introduced due to the deposition, an increase in propagation losses would steadily reduce the

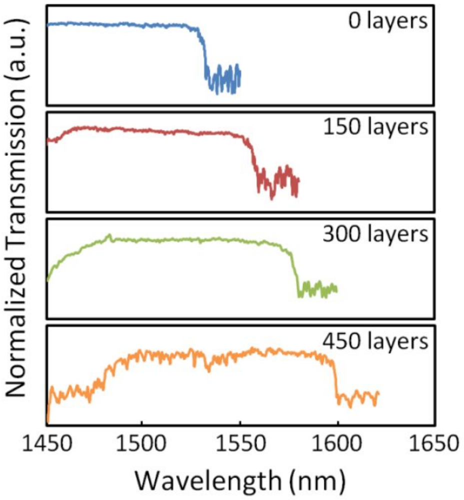

Figure 4.6: TE transmission measurements before HfO_2 ALD and after deposition in increments of 150 atomic layers. The slow-light mode onset edge is tuned across the C-band and also across part of the L-band.

maximal group indices which can be resolved by the interferometric measurements. Since the ranges of group-index values extracted are comparable for each deposition thickness, our measurements suggest that the addition of ALD HfO_2 to the PhC waveguide structure does not introduce extra roughness or increase the propagation losses.

Another factor which can affect the propagation loss of PhC waveguides is the spatial confinement of slow-light modes. Increased field overlap with the sidewall will cause increased light scattering in the presence of roughness [40]. The effects of ALD on confinement were studied for various group indices using 3D plane wave expansion computations [32]. Figure 4.7 shows the average effective modal area of slow-light modes for two different group-indices (of 50 and 6) at different deposition steps. Figure 4.7(b) shows a cross-section of the slow-light mode (at a group-index of 50) through the air-clad silicon PhC waveguide before deposition and after deposition of 160 HfO_2 atomic layers. Note that the slow-light mode is less localized than the waveguide mode at a group-index of 6, suggesting potentially higher sensitivity to ALD deposition. For the group-index of 50, the effective modal area increases from 1.79×10^{-13} m^2 to 2.03×10^{-13} m^2, i.e. by 13.4% after 160 atomic layers.

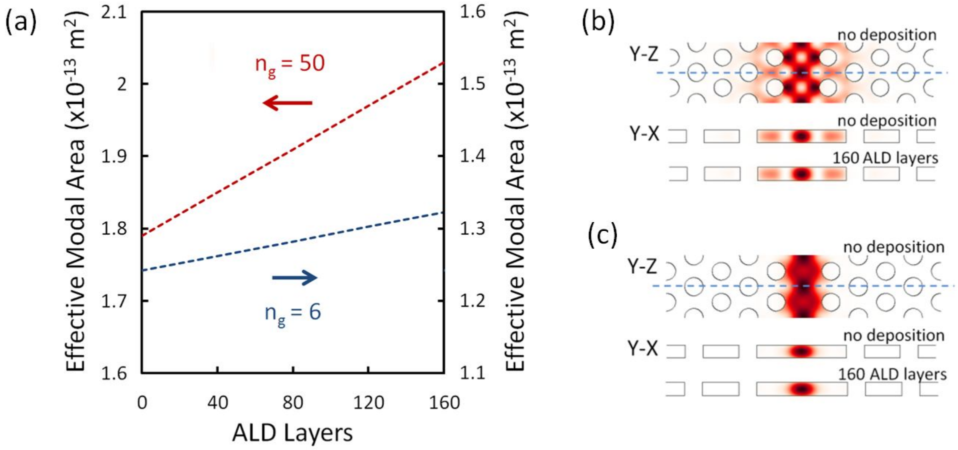

Figure 4.7: (a) Average effective area of PhC waveguide slow light modes with ALD deposition at group-index of 50 (red line) and group-index of 6 (blue line). Calculated modes of W0.9 waveguide at (b) group-index of 50 (c) group-index of 6. The blue dotted line indicates where the cross-sections are taken perpendicular to the Y-Z plane. The resulting Y-X cross-sections before and after 160 atomic layers of HfO_2 have been deposited are shown below the Y-Z figures.

For a group-index of 6, the effective modal area also increases with ALD depositions (from 1.24×10^{-13} m^2 to 1.32×10^{-13} m^2), albeit a smaller increase of 6.4% compared to the slow-light mode. As discussed previously, the deposition is conformal and does not introduce extra roughness; thus, the fabrication-induced roughness stays the same (or decreases) with increasing number of layers. However, the higher refractive index of HfO_2 compared to air results in a slightly graded structure wherein the mode interacts less with the surface. As shown in Figures 4.7(a), the average effective modal area increases at a slower rate than the increase in cross-sectional area of the dielectric material due to the conformal ALD coating (25.5% after 160 ALD layers) Thus, the conformal deposition reduces Rayleigh scattering thereby reducing the propagation loss.

4.8 Coupling into Slow Light

As group indices increase, coupling into slow-light PhC waveguides become increasingly difficult. This is a serious problem which places limitations on practical slow-light devices. It has been shown that surface terminations have a significant effect on the dispersion of surface states. This in turn affects the slow-light coupling [43, 44]. When surface states are tuned in resonance with the PhC waveguide slow light mode, transmission is improved. This is analogous to impedance matching in electronic circuits.

Here we investigated whether slight adjustments to surface states at the interface between the PhC lattice and single-mode strip waveguide using ALD could improve slow-light coupling. We investigated 3 different PhC terminations (τ = 0, 0.5 and 0.75) as shown in Fig. 4.8. Coupling coefficients were derived from the minima and maxima of interference fringes in our MZI measurements, using the equation $I_{min}/I_{max} = (1-A)^2/(1+A)^2$. In addition to coupling loss, these values also incorporate other kinds of loss such as scattering loss. The coupling coefficients before and after ALD are shown in Fig. 4.8 (b) and (c), respectively. It appears that the slight changes in surface termination by 160 atomic layers of deposition were insufficient to cause a noticeable change between the three termination types. But there is a slight decrease in coupling across all three termination types after deposition. This is likely due to increased waveguide propagation loss rather than a change in surface state coupling.

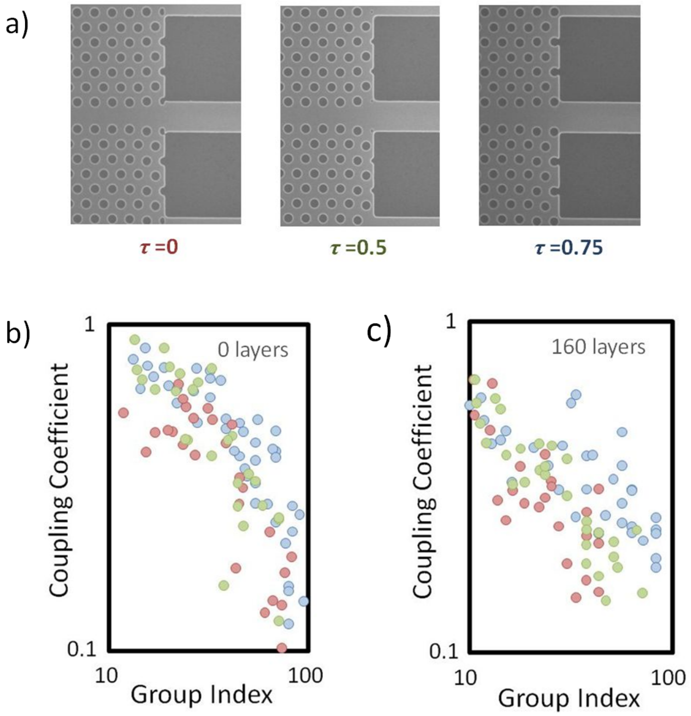

Figure 4.8: (a) SEM images of different PhC terminations at the interface between the PhC lattice and strip waveguide. From left to right: $\tau = 0$, $\tau = 0.5$ and $\tau = 0.75$. (b) Experimentally determined coupling coefficients as a function of group index (log-log scale) before ALD. Points correspond to the following surface terminations: $\tau = 0$ (red), $\tau = 0.5$ (green), and $\tau = 0.75$ (blue). c) Coupling coefficients after 160 atomic layers of HfO_2 deposited.

4.9 Conclusions

In conclusion, we have demonstrated the control of slow-light dispersion characteristics of W0.9 PhC waveguides using a self-limiting monolayer precision process. High group indices were digitally tuned with sequential atomic layer depositions without increasing propagation losses. A red-shift of 140 ± 10 pm per atomic layer was observed for the slow-light mode onset edge, while no appreciable change was observed in the GVD and TOD. A differential shift of 110 ± 30 pm per monolayer in slow-light tuning of the TE and TM modes was observed. This difference can be used for exact tuning of the pump-Stokes frequency spacing for Raman amplification. As a low temperature post-fabrication process, the atomic layer deposition of HfO_2 is an enabling passive tuning technology for many practical chip-scale slow-light devices and modules.

4.10 Acknowledgements

This investigation was a collaboration with Solomon Assefa of Yuri Vlasov's group (Silicon Integrated Nanophotonics Group) at IBM Research in Yorktown Heights, New York. The photonic chips used in this experiment were designed and fabricated by the group at IBM. The experimental measurements were performed at the Columbia University Optical Nanostructures Laboratory. Inanc Meric from Prof. Shepard's group in the Electrical Engineering department provided valuable assistance with the atomic layer deposition system and Chad Husko helped with some of the numerical simulations using the plane-wave expansion method.

Bibliography

[1] M. Bajcsy, A. S. Zibrov, and M. D. Lukin, “Stationary pulses of light in an atomic medium,” *Nature*, vol. 426, no. 6967, pp. 638–641, 2003.

[2] E. Parra and J. R. Lowell, “Toward applications of slow light technology,” *Optics and Photonics News*, vol. 18, no. 11, pp. 40–45, 2007.

[3] M. S. Bigelow, N. N. Lepeshkin, and R. W. Boyd, “Superluminal and slow light propagation in a room-temperature solid,” *Science*, vol. 301, no. 5630, pp. 200–202, 2003.

[4] M. Notomi, K. Yamada, A. Shinya, J. Takahashi, C. Takahashi, and I. Yokohama, “Extremely large group-velocity dispersion of line-defect waveguides in photonic crystal slabs,” *Physical Review Letters*, vol. 87, p. 253902, Nov 2001.

[5] X. Yang, M. Yu, D.-L. Kwong, and C. W. Wong, “All-optical analog to electromagnetically induced transparency in multiple coupled photonic crystal cavities,” *Physical Review Letters*, vol. 102, p. 173902, Apr 2009.

[6] Y. A. Vlasov, M. O’Boyle, H. F. Hamann, and S. J. McNab, “Active control of slow light on a chip with photonic crystal waveguides,” *Nature*, vol. 438, pp. 65–69, Nov. 2005.

[7] T. Baba, “Slow light in photonic crystals,” *Nature Photonics*, vol. 2, pp. 465–473, Aug. 2008.

[8] J. M. Dudley and J. R. Taylor, “Ten years of nonlinear optics in photonic crystal fibre,” *Nature Photonics*, vol. 3, pp. 85–90, Feb. 2009.

[9] T. F. Krauss, “Why do we need slow light?,” *Nature Photonics*, vol. 2, pp. 448–450, Aug. 2008.

[10] P. Colman, C. Husko, S. Combrié, I. Sagnes, C. W. Wong, and A. De Rossi, “Observation of soliton pulse compression in photonic crystal waveguides,” *ArXiv e-prints*, Apr. 2010.

[11] S. Mookherjea, J. S. Park, S. Yang, and P. R. Bandaru, “Localization in silicon nanophotonic slow-light waveguides,” *Nature Photonics*, vol. 2, pp. 90–93, Feb. 2008.

[12] V. S. C. M. Rao and S. Hughes, “Single quantum dot spontaneous emission in a finite-size photonic crystal waveguide: Proposal for an efficient “on chip” single photon gun,” *Physical Review Letters*, vol. 99, p. 193901, Nov 2007.

[13] R. Bose, J. F. McMillan, J. Gao, and C. W. Wong, “Solution-processed cavity and slow-light quantum electrodynamics in near-infrared silicon photonic crystals,” *Applied Physics Letters*, vol. 95, p. 131112, Sept. 2009.

[14] B. Jalali, D. R. Solli, and S. Gupta, “Silicon photonics: Silicon’s time lens,” *Nature Photonics*, vol. 3, pp. 8–10, Jan. 2009.

[15] B. Corcoran, C. Monat, C. Grillet, D. J. Moss, B. J. Eggleton, T. P. White, L. O’Faolain, and T. F. Krauss, “Green light emission in silicon through slow-light enhanced third-harmonic generation in photonic-crystal waveguides,” *Nature Photonics*, vol. 3, pp. 206–210, Apr. 2009.

[16] A. de Rossi, M. Lauritano, S. Combrié, Q. V. Tran, and C. Husko, “Interplay of plasma-induced and fast thermal nonlinearities in a GaAs-based photonic crystal nanocavity,” *Physical Review A*, vol. 79, p. 043818, Apr. 2009.

[17] K. Inoue, H. Oda, N. Ikeda, and K. Asakawa, “Enhanced third-order nonlinear effects in slow-light photonic-crystal slab waveguides of line-defect,” *Optics Express*, vol. 17, no. 9, pp. 7206–7216, 2009.

[18] J. F. McMillan, X. Yang, N. C. Panoiu, R. M. Osgood, and C. W. Wong, "Enhanced stimulated Raman scattering in slow-light photonic crystal waveguides," *Optics Letters*, vol. 31, no. 9, pp. 1235–1237, 2006.

[19] M. Soljačić and J. D. Joannopoulos, "Enhancement of nonlinear effects using photonic crystals," *Nature Materials*, vol. 3, pp. 211–219, Apr. 2004.

[20] T. Barwicz, M. R. Watts, M. A. Popović, P. T. Rakich, L. Socci, F. X. Kärtner, E. P. Ippen, and H. I. Smith, "Polarization-transparent microphotonic devices in the strong confinement limit," *Nature Photonics*, vol. 1, pp. 57–60, Jan. 2007.

[21] Q. Xu, P. Dong, and M. Lipson, "Breaking the delay-bandwidth limit in a photonic structure," *Nature Physics*, vol. 3, pp. 406–410, June 2007.

[22] C. W. Wong, P. T. Rakich, S. G. Johnson, M. Qi, H. I. Smith, E. P. Ippen, L. C. Kimerling, Y. Jeon, G. Barbastathis, and S.-G. Kim, "Strain-tunable silicon photonic band gap microcavities in optical waveguides," *Applied Physics Letters*, vol. 84, no. 8, pp. 1242–1244, 2004.

[23] K. Hennessy, A. Badolato, A. Tamboli, P. M. Petroff, E. Hu, M. Atatüre, J. Dreiser, and A. Imamoğlu, "Tuning photonic crystal nanocavity modes by wet chemical digital etching," *Applied Physics Letters*, vol. 87, no. 2, p. 021108, 2005.

[24] K. Srinivasan and O. Painter, "Linear and nonlinear optical spectroscopy of a strongly coupled microdisk-quantum dot system," *Nature*, vol. 450, pp. 862–865, Dec. 2007.

[25] S. Mosor, J. Hendrickson, B. C. Richards, J. Sweet, G. Khitrova, H. M. Gibbs, T. Yoshie, A. Scherer, O. B. Shchekin, and D. G. Deppe, "Scanning a photonic crystal slab nanocavity by condensation of xenon," *Applied Physics Letters*, vol. 87, no. 14, p. 141105, 2005.

[26] S. Strauf, M. T. Rakher, I. Carmeli, K. Hennessy, C. Meier, A. Badolato, M. J. A. DeDood, P. M. Petroff, E. L. Hu, E. G. Gwinn, and D. Bouwmeester, "Frequency control of photonic crystal membrane resonators by monolayer deposition," *Applied Physics Letters*, vol. 88, no. 4, p. 043116, 2006.

[27] J. Schrauwen, D. V. Thourhout, and R. Baets, "Trimming of silicon ring resonator by electron beam induced compaction and strain," *Optics Express*, vol. 16, no. 6, pp. 3738–3743, 2008.

[28] X. Yang, C. J. Chen, C. A. Husko, and C. W. Wong, "Digital resonance tuning of high-Q/V_m silicon photonic crystal nanocavities by atomic layer deposition," *Applied Physics Letters*, vol. 91, no. 16, p. 161114, 2007.

[29] E. Graugnard, D. P. Gaillot, S. N. Dunham, C. W. Neff, T. Yamashita, and C. J. Summers, "Photonic band tuning in two-dimensional photonic crystal slab waveguides by atomic layer deposition," *Applied Physics Letters*, vol. 89, no. 18, p. 181108, 2006.

[30] S. Assefa and Y. A. Vlasov, "High-order dispersion in photonic crystal waveguides," *Optics Express*, vol. 15, no. 26, pp. 17562–17569, 2007.

[31] S. McNab, N. Moll, and Y. Vlasov, "Ultra-low loss photonic integrated circuit with membrane-type photonic crystal waveguides," *Optics Express*, vol. 11, no. 22, pp. 2927–2939, 2003.

[32] S. Johnson and J. Joannopoulos, "Block-iterative frequency-domain methods for Maxwell's equations in a planewave basis," *Optics Express*, vol. 8, no. 3, pp. 173–190, 2001.

[33] J. F. McMillan, M. Yu, D.-L. Kwong, and C. W. Wong, "Observation of spontaneous raman scattering in silicon slow-light photonic crystal waveguides," *Applied Physics Letters*, vol. 93, no. 25, p. 251105, 2008.

[34] M. Fadel, O. A. Azim M., O. A. Omer, and R. R. Basily, "A study of some optical properties of hafnium dioxide (HfO_2) thin films and their applications," *Applied Physics A: Materials Science & Processing*, vol. 66, pp. 335–343, 1998.

[35] R. L. Puurunen, "Surface chemistry of atomic layer deposition: A case study for the trimethylaluminum/water process," *Journal of Applied Physics*, vol. 97, no. 12, p. 121301, 2005.

[36] J. C. Hackley, J. D. Demaree, and T. Gougousi, "Interface of atomic layer deposited HfO_2 films on GaAs (100) surfaces," *Applied Physics Letters*, vol. 92, no. 16, p. 162902, 2008.

[37] R. Puthenkovilakam, Y. S. Lin, J. Choi, J. Lu, H.-O. Blom, P. Pianetta, D. Devine, M. Sendler, and J. P. Chang, "Effects of post–deposition annealing on the material characteristics of ultrathin HfO_2 films on silicon," *Journal of Applied Physics*, vol. 97, no. 2, p. 023704, 2005.

[38] N. Panoiu, J. McMillan, and C. W. Wong, "Theoretical analysis of pulse dynamics in silicon photonic crystal wire waveguides," *Selected Topics in Quantum Electronics, IEEE Journal of*, vol. 16, pp. 257 –266, jan.-feb. 2010.

[39] R. Engelen, Y. Sugimoto, Y. Watanabe, J. Korterik, N. Ikeda, N. van Hulst, K. Asakawa, and L. Kuipers, "The effect of higher-order dispersion on slow light propagation in photonic crystal waveguides," *Optics Express*, vol. 14, no. 4, pp. 1658–1672, 2006.

[40] D. K. Sparacin, S. J. Spector, and L. C. Kimerling, "Silicon waveguide sidewall smoothing by wet chemical oxidation," *Journal of Lightwave Technology*, vol. 23, no. 8, p. 2455, 2005.

[41] E. Dulkeith, S. J. McNab, and Y. A. Vlasov, "Mapping the optical properties of slab-type two-dimensional photonic crystal waveguides," *Physical Review B*, vol. 72, p. 115102, Sep 2005.

[42] Y. A. Vlasov, M. O'Boyle, H. F. Hamann, and S. J. McNab, "Active control of slow light on a chip with photonic crystal waveguides," *Nature*, vol. 438, pp. 65–69, Nov. 2005.

[43] Y. A. Vlasov, N. Moll, and S. J. McNab, "Observation of surface states in a truncated photoniccrystal slab," *Optics Letters*, vol. 29, pp. 2175–2177, Sep 2004.

[44] Y. A. Vlasov and S. J. McNab, "Coupling into the slow light mode in slab-type photonic crystal waveguides," *Optics Letters*, vol. 31, pp. 50–52, Jan. 2006.

Chapter 5

Hydrogen Annealing and Sidewall Roughness

5.1 Overview

Hydrogen annealing of silicon-on-insulator (SOI) wafers was first studied to improve wafer bonding technology. These studies showed that hydrogen annealing could improve the surface roughness to an extent comparable to chemical mechanical polishing [1]. More recently, hydrogen annealing has received interest in silicon photonics for its ability to improve post-etching sidewall roughness as well as its ability to create rounded features[2, 3]. Improved sidewall roughness can decrease the propagation loss in waveguides and increase the quality factor of optical resonators.

The hydrogen annealing process involves placing substrates in a high temperature hydrogen environment. Often, low pressures are also used. The smoothening of surfaces and rounding of sharp corners is the result of atom migration driven by surface energy minimization. Gibbs [1] described the equilibrium shape of a droplet or crystal as depending on the minimization of the quantity ΔG_i:

$$\mathrm{\Delta G_i = \sum_n A_n \gamma_n} \tag{5.1}$$

A_n is the area of the nth crystal face. γ_n is the surface energy or surface tension per unit area of the nth face and it can also be thought of as the amount of work needed to create a new surface from bulk material [4]. From this equation, it can be seen that round shapes are often thermodynamically favorable because they minimize the overall surface area.

Thermal reflow techniques have been used on optical microstructures made of amorphous materials such as oxide and polymers. Fig. 5.1 is an SEM image of a surface tension induced silica microcavity made by thermal reflow using a CO_2 laser. The original shape of this device was a microdisk but upon reflow it formed into a toroid. The toroidal shape is in thermodynamic equilibrium and will not be effected by further thermal processing [5]. Armani has created similar toroidal microcavities with Q over 100 million [5]. The equilib-

---

[1] Joshiah Willard Gibbs was awarded the first Ph.D. in engineering in the United States in 1863 from Yale University. One year later, the King's College School of Mines was founded. The school is now known as the Columbia University Fu Foundation School of Engineering and Applied Science.

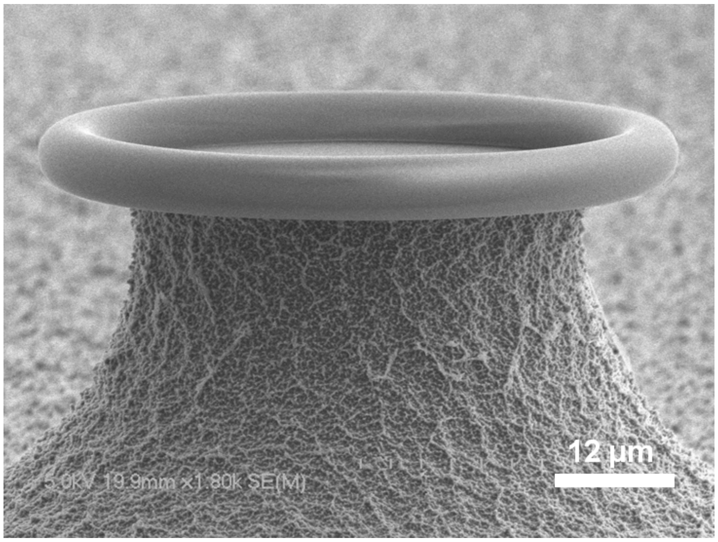

Figure 5.1: Silica microtoroid fabricated by laser induced thermal reflow. The pedestal is single-crystal silicon.

rium shape of reflowed devices is not purely geometry dependent but can also be material dependent. Grossman has demonstrated that when poly(methyl methacrylate) microdisks are reflowed they adopt a self-limiting conical shape. These conical microresonators have been shown to have a Q of 2 million [6].

Unlike amorphous materials, crystalline materials often show directional preferences during fabrication processes such as etching. Thermal reflow can also have directionally dependent effects on single-crystal materials but this will be discussed later. Maleki and Mailis have thermally reflowed a number of single-crystal optical materials including lithium niobate, lithium tantalate, sapphire and calcium fluoride [7, 8]. The optical resonators in Maleki's experiments were fairly large, on the millimeter scale. A summary is shown in Table 5.1.

The material we are most interested in is single-crystal silicon and Wu has fabricated a 39 μm diameter silicon microtoroid with a surface roughness of less than 2.6 Å. While the device has atomic level smoothness, it's Q-factor is unexpectedly low at 1.1×10^5 [12]. Due to it's large size, the microtoroid's Q is not radiation limited. The vast improvement in surface roughness should increase the Q significantly but this was not observed. By

Table 5.1: Thermal reflow on amorphous and crystalline optical materials

Material	**Atomic Structure**	**Device**	**Q-factor**	**Ref.**
Silica (SiO_2)	amorphous	microtoroid (r=47μm)	1×10^8	[5]
Poly(methyl methacrylate) (PMMA)	amorphous	conical cavity (r=40μm)	2×10^6	[6]
Arsenic Trisulfphide (As_2S_3)	amorphous	waveguides	n/a	[9, 10]
Lithium Niobate ($LiNbO_3$)	crystalline	toroid (r$\sim$3mm)	$> 2\times10^8$	[7, 8]
Lithium Tantalate ($LiTaO_3$)	crystalline	toroid (r$\sim$3mm)	$> 2\times10^8$	[8]
Sapphire (Al_2O_3)	crystalline	toroid (r$\sim$3mm)	$> 1\times10^9$	[8]
Calcium Fluoride (CaF_2)	crystalline	toroid (r=50μm)	4×10^8	[11]

comparison, atomically smooth amorphous silica microtoroids have a Q of 1×10^8 [5] and even unannealed silicon microdisks have been fabricated with a Q of 3×10^6 [13].

Hence, the purpose of this study was to better characterize the effects of hydrogen annealing on improving the quality of silicon microresonators. If indeed hydrogen annealing failed to improve the resonators performance despite achieving atomic-scale roughness it was of interest to understand what other factors were limiting the Q.

5.2 Fabrication

The silicon microdisks used in this experiment were fabricated by two different methods, both on SOITEC SOI wafers with 250 nm of slilcon, approximately 2 μm of oxide, and p-type doping concentration of 10^{16} cm^{-3}. Some of the disks were fabricated using high quality photolithography at IME. Other disks were fabricated in the Columbia cleanroom using the NPGS e-beam lithography system. While e-beam generally produces higher quality devices, the IME devices had superior surface and sidewall roughness due the limitations of dry-etching equipment as well as relatively high particle count in the Columbia cleanroom. The different surface roughnesses were purposely fabricated in order to help evaluate the effects of hydrogen annealing.

5.3 Hydrogen Annealing

The annealing furnace used in this experiment was part of the laboratory of Stephen O'Brien and the hydrogen annealing was done with Limin Huang, a research scientist in the group. Samples were placed on a cermanic boat and inserted into the middle of a 1-inch diameter quartz tube furnace. Hydrogen gas at a pressure of 760 torr was flowed through the tube at a rate of approximately 500 cm^3/min. On some runs, inert argon gas was added to the gas flow in order to reduce the hydrogen content (40 torr H_2 : 720 torr Ar). For safety reasons as well as to prevent oxidation, care was taken to stop oxygen from leaking into the system. The furnace temperature controller allowed for steady ramp up and cool down of the temperature. Experiments were performed at atmospheric pressure as there was no vacuum on the system. Work by other groups has shown that surface smoothening using hydrogen annealing at atmospheric pressures. The tradeoff has been the longer annealing times required [14].

Annealing was performed at temperatures up to 950°C which was the upper limit for this particular furnace. A temperature ramp up rate of 20°C/min was used. The sample was held at the annealing temperature for periods ranging from 1 to 6 hours. After annealing, the sample was allowed to cool down slowly overnight in order to minimize thermal stress. Prior to the experiment a RCA clean was performed on the sample. In addition, the quartz furnace tube was physically cleaned and then purged with an argon gas flow for 1 hour to remove contaminants.

5.4 Discussion

Fig. 5.2 shows SEM images from a microdisk surface taken before and after hydrogen annealing. It is apparent that instead of decreasing surface roughness, the thermal processing has actually increased roughness. This phenomenon occurred throughout the range of different process parameters used. We found this was very puzzling at first but later became aware that some other research groups had actually observed similar phenomena during hydrogen annealing [15, 16]. For example, both Yanase and Habuka observed rectangular shaped pitting in (001) silicon and triangular shaped pitting in (111) silicon [17]. We also observed rectangular pitting with our chips fabricated on (001) silicon.

The cause of increased surface roughness is due to hydrogen etching of the silicon by two reactions:

$$\mathrm{Si} + 2\mathrm{H}_2\ (\mathrm{g}) \longrightarrow\ \mathrm{SiH}_4\ (\mathrm{g}) \tag{5.2}$$

$$\mathrm{Si} + \mathrm{H}_2\ (\mathrm{g}) \longrightarrow\ \mathrm{SiH}_2\ (\mathrm{g}) \tag{5.3}$$

But if the etching of silicon is uniform, it should not cause pitting and surface nonuniformities. Another reaction also plays an important role, the etching of oxide by the hydrogen gas. The etch rate of the oxide is slower than for silicon and also more temperature dependent

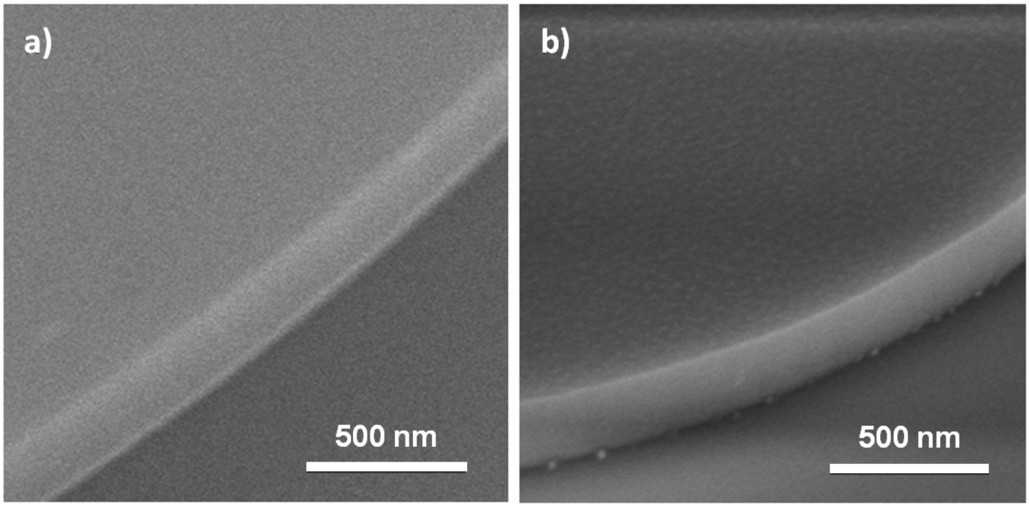

Figure 5.2: SEM images of silicon microdisk surface and edge; (a) before hydrogen annealing (b) after hydrogen annealing. Scale bar in both images represents 500 nm.

[15].

$$SiO_2 + H_2\ (g) \longrightarrow\ SiO\ (g) + H_2O\ (g) \tag{5.4}$$

The difference in etch rates is the cause of pitting during hydrogen annealing. Residual islands of oxide on the surface will serve as etch masks as the silicon is etched away. Even a native oxide as thin as 4 Å can result in increased surface roughness.

In our experiment we performed a RCA clean to remove the native oxide and metallic contaminants before putting the sample into the annealing furnace. But it required 10-15 minutes to transport the sample from the acid hood in the cleanroom to the laboratory with the furnace. It is also possible that trace amounts of moisture and oxygen from the hydrogen gas tank could have resulted in thin oxide formations.

The solution to this problem would be to anneal at higher temperatures where the etch rate for oxide is higher. Indeed, Habuka observed less surface roughness with higher temperature annealing [15]. In addition, a lower pressure would decrease the etching of both silicon and oxide and also increase atom migration and rounding effects [2]. Unfortunately, neither of these two options was available to us due to the inherent limitations of the furnace being used.

Carbon contamination may have also played a role in increasing roughness. The formation of carbon-silicon bonds on the surface could lead to micromasking, similar to residual oxide islands previously described. Carbon-silicon bonds can be difficult to break, requiring high temperatures of over 1200°C [14]. The SEM image in Fig. 5.3(a) shows carbon nanotube growth, the result of carbon contamination in the furnace flow chamber. The furnace had been previously used for carbon nanotube growth but was rigorously cleaned and purged before this experiment. Even when the quartz tube was replaced with a new and unused tube, carbon nanotube contamination was still observed.

In addition to surface roughness effects, linear crystallographic defects known as dislocations were observed after hydrogen annealing. Stresses are generated in the substrate by large temperature gradients during thermal processing. When stresses are sufficiently high, silicon bonds can break and reform with adjacent atoms resulting in a misalignment of atoms in the crystal lattice. These dislocations must exist as complete loops and cannot end inside of the crystal. Hence, they are visible on the crystal surface as seen in the SEM images in Fig. 5.3. While dislocations are generally atom-scale in width, the dislocations in the SEM image appear to be much wider. Indeed, it is the hydrogen induced etching which exposes the dislocations, which otherwise might not be observable by SEM. Preferential etching of silicon around the dislocations is attributed to weaker atomic bonds caused by higher stress fields around the dislocations. This results in wide trenches along the path of the dislocation. Where the dislocation changes direction and goes into the plane of the crystal, deep holes are also etched following the dislocation down into the crystal.

5.5 Conclusions

The results from the hydrogen annealing were unexpected. Upon further analysis, it is believed that the resulting surface morphology was due to equipment limitations. For surface roughness improvement, a higher temperature and lower pressure are needed. In addition, a higher purity hydrogen gas flow and prevention of carbon and other contaminates into the flow tube is also necessary.

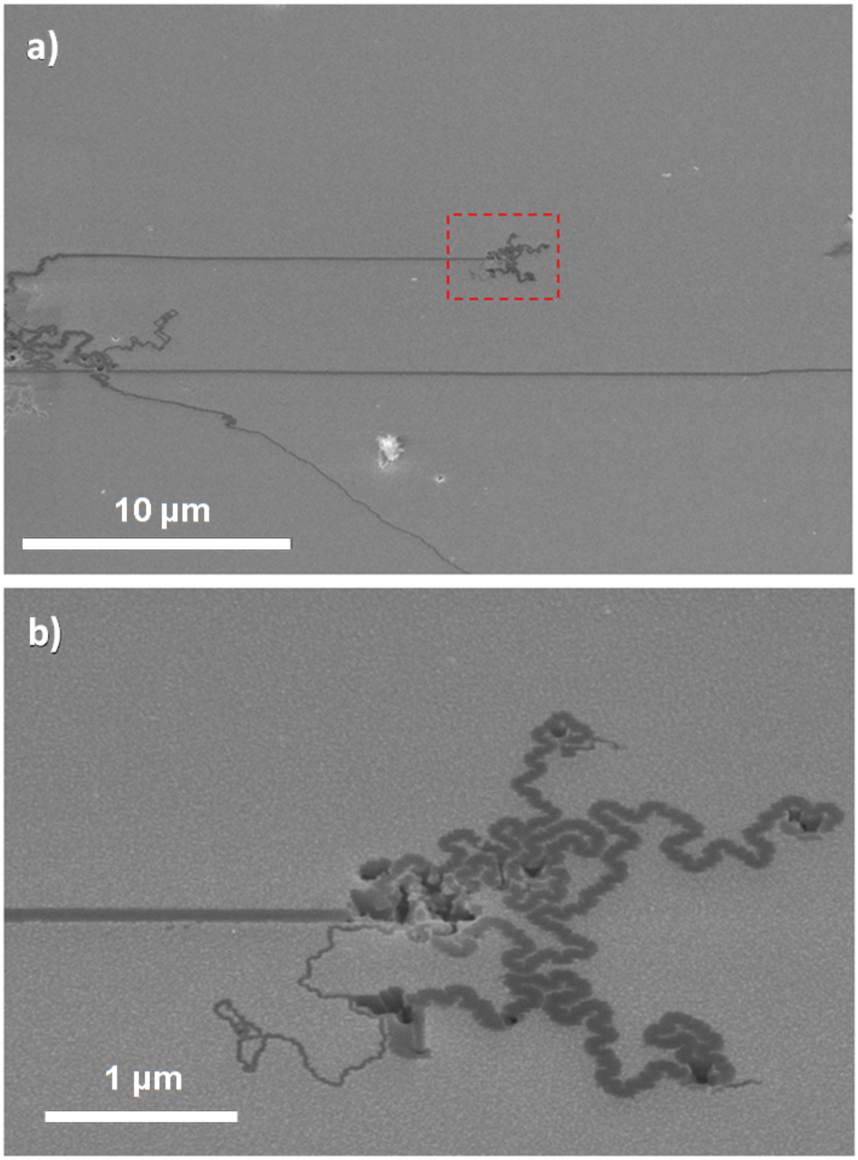

Figure 5.3: SEM images of silicon surface after hydrogen annealing. Pitting, dislocations and carbon nanotube contamination can be seen. The region in (a) enclosed by the dotted line is magnified and shown in (b). The scale bar in (a) is 10 μm and in (b) is 1 μm.

While this experiment failed to meet our expectations for improving surface roughness, it did provide us with some valuable insights. One of the motivations for this experiment was to understand the unusually low Q values observed by Wu in atomically smooth hydrogen annealed silicon microtoroids [12]. Our results give a potential explanation for this. The presence of dislocations and possibly also point defects caused by the stresses in high temperature processing can degrade the performance of single-crystal nanophotonic devices. These atomic-level defects might serve as color centers resulting in increased light absorption. They might also result in increased light scattering. These are potential areas for further research.

An alternative form of thermal processing could potentially circumvent these thermal stress issues. Localized thermal processing via lasers (as discussed earlier in this thesis) can minimize thermal stresses. For SOI devices, the different coefficients of thermal expansion between silicon and oxide can result in large stresses during thermal processing. Since thermal expansion is proportional to the length of a heated object, a smaller heating region will minimize the atomic displacements experienced between the silicon and oxide layers.

5.6 Acknowledgements

The hydrogen annealing furnace used in this work was in the laboratory of Prof. O'Brien. Limin Huang, a research scientist in the O'Brien group provided generous help with furnace. Optical devices were fabricated by e-beam lithography and photolithography at the Columbia University cleanroom using fabrication processes that I had developed. SEM analysis was performed at the Columbia MRSEC facilities.

Bibliography

[1] N. Sato and T. Yonehara, "Hydrogen annealed silicon-on-insulator," *Applied Physics Letters*, vol. 65, pp. 1924 –1926, Oct. 1994.

[2] H. Kuribayashi, R. Hiruta, R. Shimizu, K. Sudoh, and H. Iwasaki, "Shape transformation of silicon trenches during hydrogen annealing," *Papers from the 49th International Symposium of the American Vacuum Society*, vol. 21, no. 4, pp. 1279–1283, 2003.

[3] M. Lee, W. Chiu, T. Yang, and C. Chen, "Monolithically integrated low-loss silicon photonic wires and three-dimensional tapered couplers fabricated by self-profile transformation," *Applied Physics Letters*, vol. 91, p. 191114, Nov. 2007.

[4] J. W. Gibbs, *The Collected Works of J. Willard Gibbs.* New York, Longmans, Green, 1931.

[5] D. K. Armani, T. J. Kippenberg, S. M. Spillane, and K. J. Vahala, "Ultra-high-Q toroid microcavity on a chip," *Nature*, vol. 421, pp. 925–928, Feb. 2003.

[6] T. Grossmann, M. Hauser, T. Beck, C. Gohn-Kreuz, M. Karl, H. Kalt, C. Vannahme, and T. Mappes, "High-Q conical polymeric microcavities," *Applied Physics Letters*, vol. 96, no. 1, p. 013303, 2010.

[7] C. Y. J. Ying, C. L. Sones, A. C. Peacock, F. Johann, E. Soergel, R. W. Eason, M. N. Zervas, and S. Mailis, "Ultra-smooth lithium niobate photonic micro-structures by surface tension reshaping," *Optics Express*, vol. 18, no. 11, pp. 11508–11513, 2010.

[8] A. A. Savchenkov, V. S. Ilchenko, A. B. Matsko, and L. Maleki, “Kilohertz optical resonances in dielectric crystal cavities,” *Physical Review A*, vol. 70, p. 051804, Nov 2004.

[9] D.-Y. Choi, S. Madden, D. Bulla, R. Wang, A. Rode, and B. Luther-Davies, “Thermal annealing of arsenic tri-sulphide thin film and its influence on device performance,” *Journal of Applied Physics*, vol. 107, p. 053106, Mar. 2010.

[10] J. Hu, N.-N. Feng, N. Carlie, L. Petit, A. Agarwal, K. Richardson, and L. Kimerling, “Optical loss reduction in high-index-contrast chalcogenide glass waveguides via thermal reflow,” *Optics Express*, vol. 18, pp. 1469–1478, Jan 2010.

[11] I. S. Grudinin, V. S. Ilchenko, and L. Maleki, “Ultrahigh optical Q factors of crystalline resonators in the linear regime,” *Physical Review A*, vol. 74, p. 063806, Dec 2006.

[12] J. Yao, D. Leuenberger, M.-C. Lee, and M. Wu, “Silicon microtoroidal resonators with integrated MEMS tunable coupler,” *Selected Topics in Quantum Electronics, IEEE Journal of*, vol. 13, no. 2, pp. 202 –208, 2007.

[13] M. Soltani, S. Yegnanarayanan, and A. Adibi, “Ultra-high Q planar silicon microdisk resonators for chip-scale silicon photonics,” *Optics Express*, vol. 15, pp. 4694–4704, Apr 2007.

[14] S. Sato, I. Mizushima, K. Miyano, T. Sato, S. Nakamura, Y. Tsunashima, T. Arikado, and N. Uchitomi, “Defects induced by carbon contamination in low-temperature epitaxial silicon films grown with monosilane,” *Japanese Journal of Applied Physics*, vol. 44, pp. 1169–1173, Mar. 2005.

[15] H. Habuka, H. Tsunoda, M. Mayusumi, N. Tate, and M. Katayama, “Roughness of silicon surface heated in hydrogen ambient,” *Journal of The Electrochemical Society*, vol. 142, no. 9, pp. 3092–3098, 1995.

[16] Y. Yanase, H. Horie, Y. Oka, M. Sano, S. Sumita, and T. Shigematsu, “Atomic force microscopy observation of Si(100) surface after hydrogen annealing,” *Journal of The Electrochemical Society*, vol. 141, no. 11, pp. 3259–3263, 1994.

[17] Y. Yanase, H. Nishihata, T. Ochiai, and H. Tsuya, “Atomic force microscope observation of the change in shape and subsequent disappearance of crystal-originated particles after hydrogen-atmosphere thermal annealing,” *Japanese Journal of Applied Physics*, vol. 37, pp. 1–4, Jan. 1998.

Chapter 6

Excimer Laser and Sidewall Roughness

6.1 Overview

Whispering gallery mode (WGM) optical microcavities such as microspheres, microtoroids and microdisks have been widely studied and applied to applications such as low-threshold microcavity lasers [1, 2, 3] and biomolecular sensors [4, 5]. Thermal techniques have been employed to improve resonator quality factors by improving the smoothness of the microcavity surfaces. Examples of this are polymer reflow for conical polymeric microcavities [6] and CO_2 laser assisted reflow for silica microcavities [5]. Larger-sized calcium fluoride microdisks (millimeter-scale) have shown $Q > 3\times10^5$ [7]. Thermal reflow has also been studied with chalcogenide glass waveguides [8] as well as single-crystalline lithium niobate structures [9]. Similarly, thermal methods such as hydrogen annealing have also been applied to silicon microcavities [10].

WGM resonators made of silicon have several disadvantages to other material systems but can be more readily integrated into the silicon photonics platform. For example, direct bandgap materials such as gallium nitride are more ideal for microdisk lasers than silicon which is an indirect bandgap material [1]. Silica based microtoroids can also be made into lasers by applying an Erbium-doped sol-gel thin film around the resonator [11]. And similarly for silicon rich oxide based microtorids by doping with silicon nanocrystals [3]. Another disadvantage of silicon-based WGM resonators is that higher quality factors have been achieved in other systems. Silica microtoroids have shown Q values of $4\text{x}10^8$ whereas silicon microtoroids fabricated via hydrogen annealing have only shown Q-values of $1.1\text{x}10^5$. The diameter of the disks were 29 μm and 39 μm, respectively [12, 10]. Despite the limitations, silicon photonics is very much an active area of research due to its commercial potential.

Rayleigh scattering, the elastic scattering of photons from subwavelength scale particles or density fluctuations, can adversely affect optical performance of silicon microcavities. The source of edge roughness can be attributed to fabrication, particularly the dry etching step. Using resist reflow and low-damage plasma dry etch Q factors of $5\text{x}10^6$ have been achieved. For disks having a diameter larger than 10 μm the Q-limiting factor is no longer Rayleigh scattering but rather surface state absorption and bulk absorption [13]. Smaller microdisks are more susceptible to the effects of surface roughness. Improving the Q factors for small diameter microdisks is important for applications requiring high-Q to modal volume ratio (Q/V_m).

Research by Chou's group has shown that the sidewall roughness of silicon devices can be substantially decreased by excimer laser assisted melting and re-solidification, a process they refer to as *self-perfection by transient liquefaction* [14]. As a processing tool, excimer laser has several unique advantages. Roughness is improved by a single shot lasting only 20-30 ns. Time-resolved reflectivity measurements using a HeNe laser show that melting can begin to occur after 1 ns and the silicon can stay molten for over 200 ns [15]. Melting only occurs on the top silicon surface to a depth of 50-300 nm. Hence there will be minimal effect on any underlying structures. By comparison, longer wavelength lasers such as 532-nm green lasers, have a much longer coupling depth and will tend to heat up the bulk substrate as illustrated in Fig. 6.1 [1]. The excimer beam is strongly absorbed by silicon but only weakly absorbed by oxide because the bandgap is too large. The band gaps of silicon and oxide are 1.12 eV and 8.9 eV, respectively. Also the spot size of the excimer beam can be varied with a mask. The mask size can range from microns up to millimeters and allow for selective exposure to certain locations.

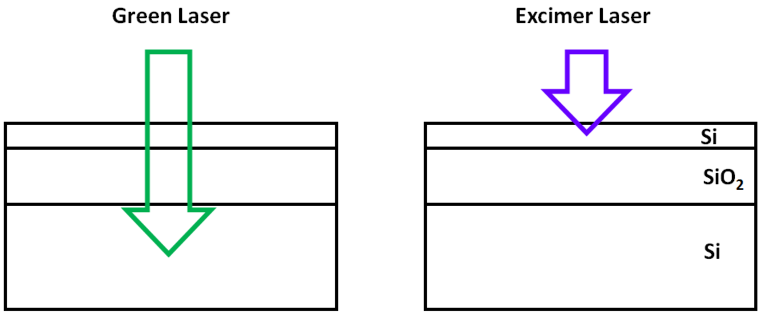

Figure 6.1: Comparison between the coupling depth of the green laser and excimer laser in SOI substrates. Not drawn to scale. The top silicon layer is 250 nm, the oxide layer is 3 μm, and the bulk silicon substrate is $\sim$ 750 μm.

---

[1] Our work with laser-assisted local oxidation in Chapter 2 shows that it is possible to achieve localized surface melting with the green laser if the beam is focused to a small spot size ($\sim$ 2.5 μm radius).

6.2 Fabrication and Experiment

In this work, we investigate using excimer laser to decrease the edge roughness of silicon microdisks and microrings in order to improve the properties of optical resonators. The devices were fabricated on SOI wafers with a 250 nm top layer of single-crystal silicon and 3 μm of thermal oxide. The microdisk is a good device for studying the effects of surface roughness because the optical confinement of its whispering-gallery mode can be varied by changing the disk radius. This allows the effects of losses due to sidewall roughness to be separated from other loss mechanisms [16]. Microrings were also studied due to their different geometry and hence silicon melting profiles. Note that microdisks are suspended by a central oxide pedestal, whereas microrings are directly on top of oxide. In addition, microrings should be more sensitive to sidewall roughness effects as they have both inner and outer sidewalls.

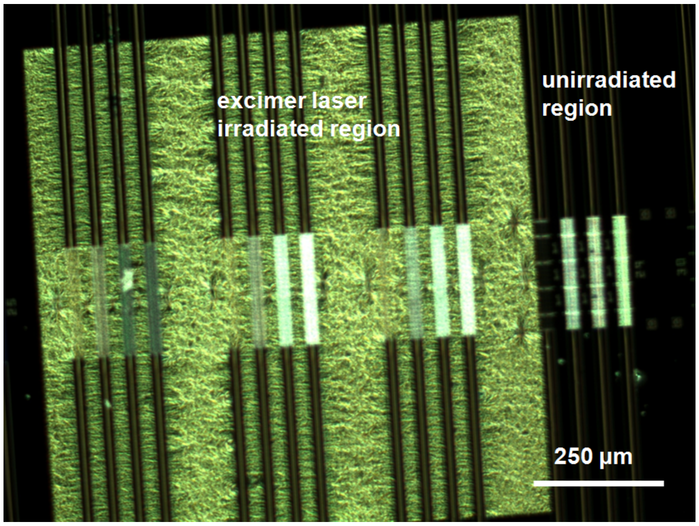

Figure 6.2: Dark-field optical microscope image of highly non-uniform silicon surface morphology after excimer exposure if BOE dip prior to exposure is not performed.

Several different fabrication methods were employed for our microdisk and microring devices, in order to create different initial sidewall roughnesses. SEM image analysis of devices fabricated by IME (process described in previous chapters) using high-quality photolithography showed sidewall roughenss of less than $\sim$ 3 nm. Microdisks fabricated in the Columbia Cleanroom and dry etched at Brookhaven CFN showed a far higher initial sidewall roughness. In this process, AZ5214E resist was spin coated on the SOI substrates. A Suss contact aligner was used for pattern transfer from a chrome mask (PhotoSciences, Inc.) with 50 nm roughness to the substrate. After development, a thermal reflow step was applied in order to reduce the sidewall roughness of the resist patterns. Subsequently, a cryogenic plasma etch process with straight sidewalls was used to transfer the pattern from resist into silicon.

Excimer laser irradiation was performed on microdisks both with and without the underlying oxide layer etched. However, chips that were not etched prior to the excimer exposure were etched afterwards. The oxide was etched in buffered hydrofluoric acid and the resulting undercut beneath the microdisk was approximately 2 μm. No oxide etching was performed for the microring devices. Just prior to exposure, all chips were dipped in dilute buffered oxide etch (BOE) for 5 seconds to remove any native oxide. Samples that did not go through the BOE dip, showed highly non-uniform surface morphology under the optical microscope after excimer exposure, as shown in Fig 6.2.

The laser used was a Lambda Physik (Coherent) 308 nm XeCl excimer with a 28 ns pulse. The energy densities used ranged from 228 to 1300 mJ/cm^2. Lower energy densities can also be achieved by attenuating the beam but these lower energies were well below the threshold of melting for the silicon samples. Light intensity drops by $I = I_0 exp(-\alpha z)$ and melting only occurs to a depth of 50-300 nm. Energy transfer primarily consists of rapid heat diffusion into the oxide pedestal and possibly evaporative cooling at higher energies. Convective and radiative cooling are negligible [17]. The heat flow throught the oxide pedestal will be slower due to its lower heat conductivity but the heat will quickly dissipate once it reaches the bulk silicon substrate. At higher energies, ablation can occur which will result in the redeposition of ablated silicon particles on the top surface of the devices and surrounding areas.

The threshold melting energy is dependent on the geometry. SEM analysis shows slight melting at the microdisk edges at energy densities as low as $\sim$ 260 mJ/cm^2 when the microdisk oxide has been undercut by 2 μm. Microdisks with no undercut prior to irradiation had a melting threshold of $\sim$ 400 mJ /cm^2. This is much lower than the 800 mJ /cm^2

threshold reported by Chou [15]. The difference being our samples are SOI whereas his are bulk silicon.

Two-dimensional finite element simulations (COMSOL Multiphysics) of heat flow through the silicon microdisks and oxide pedestal show that heat becomes concentrated at the upper edge of the microdisk. The edge regions will heat up the most and hence melt even before the top surface. This behaviour is also confirmed from SEM images which showed melting along the upper edge of the microdisk before spreading to other areas.

The silicon stays molten for several hundred nanoseconds [15]. While previous work shows that the molten time is sufficient for smoothening out of the surface [14], this is not the case for different geometries. Another issue is the preservation of the single-crystalline structure of silicon. If the single-crystal silicon is melted too deeply, solidification will occur at numerous nucleation sites and result in grain growth. The result will be polycrystalline silicon which is highly unfavorable in silicon photonics because of the increased light scattering from the grain boundaries. This will result in increased optical losses.

6.3 SEM Image Analysis

SEM images were taken before and after excimer irradiation in order to analyze changes in edge roughness. Low accelerating voltages of 0.8 kV were used for imaging surface roughness because of the reduced penetration depth of the electron beam and minimal charging effects in the oxide layer. Top-down SEM images were taken at magnifications of 100,000× and 150,000× where the pixel sizes were $\sim$ 1 nm and $\sim$ 0.7 nm respectively.

The root mean square edge roughness as defined in Eqn.(6.1) was determined through SEM image analysis. The parameters N and δ are the total number of pixels in the x-direction and the distance from the average surface edge, respectively. In order to characterize the spatial distribution of the roughness, the correlation length ξ was determined from the correlation function, Eqn.(6.2). ξ can also be defined as the minimum length where σ becomes independent of the length [18].

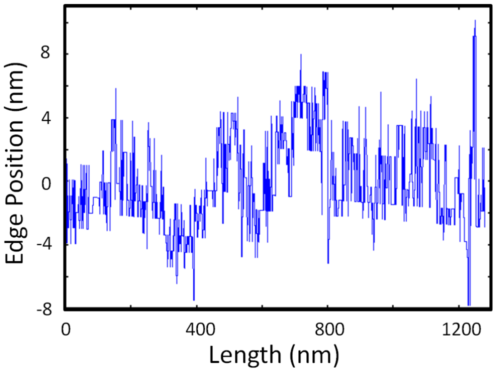

Figure 6.3: SEM image analysis of a line edge prior to excimer exposure. The RMS roughness is 2.8 nm.

$$\sigma = \sqrt{\frac{\sum_{i=1}^{N} \delta_i^2}{N}} \tag{6.1}$$

$$G(r) = \sqrt{\frac{1}{N-m} \sum_{i=1}^{N-m} (\delta_{i+m} - \delta_i)^2} \tag{6.2}$$

$$\alpha \leq \frac{\sigma^2}{k_0 d^4 n_1} \kappa \tag{6.3}$$

Eqn.(6.3) is an analytical relationship between scattering loss (α) and roughness (σ) [19]. The other parameters k_0, d, n_1 and κ are the free space wavenumber, thickness, refractive index and a statistical factor, respectively. Eqn.(6.3), which describes the upper limit for scattering loss, assumes the correlation length is comparable to the beat length between the guided and radiation modes resulting in maximum scattering. The equation shows the importance of minimizing the sidewall roughness. [19].

6.4 Experimental Setup

Two different test setups were used in this experiment. This was dictated by the different approaches needed to couple light in the microdisk and microring devices. For microdisks, evanescent coupling by tapered fiber allows for quick measurements and low losses. But the evanescent coupling technique does not work well for SOI microrings because the evanescent field from the fiber taper will couple into the underlying oxide. Instead, light is coupled to microrings by on-chip strip waveguides. Lensed fibers are used to couple off-chip light into these waveguides.

A tapered fiber with 2 dB loss was pulled from single mode optical fiber (Corning SMF-28e). The fiber pulling was done using linear motors to slowly pull on two ends of the fiber while a small cladding-stripped region along the mid-length of the fiber was exposed to a small hydrogen flame. The optical transmission was monitored to determine the stop point whereupon the minimum fiber diameter has decreased from 9 μm to approximately 1 μm. The taper was then bent, with a resulting bend radius of approximately 0.5 mm, and mounted on a 3-axis stage with differential actuators for regular stage movements and piezoelectric actuators for fine movements (20 nm resolution). The test chip was mounted on a 4-axis stage and imaged from above with a 50x long-working distance objective connected to an ultra-zoom lens system with a high-resolution CMOS camera. An image of the fiber to microdisk coupling is shown in Fig.6.4

Despite the different coupling approaches, the rest of the test setup is fairly similar. A broadband ASE source and optical spectrum analyzer with 10 pm resolution are used to take transmission measurements. For higher resolution measurements, a tunable laser with a spectral width of 200 kHz, InGaAs detector and lock-in amplifier are used. A polarization controller was used to change between TE and TM polarizations. The TE polarization was determined by referencing to the known TE polarization of a silicon photonic crystal cavity.

6.5 Excimer Irradiation Results

Figure 6.5 shows a SEM image of a microdisk after excimer laser irradiation. Excimer-assisted melting begins along the upper edge of the microdisk and moves inwards. Unlike the CO_2 laser-assisted reflow of silica microtoroids [20], the excimer-assisted melting does not result in a self-limiting microtorid. One difference is the oxide pedestal which cannot dissipate heat as efficiently as a silicon pedestal. At high enough energies and long enough

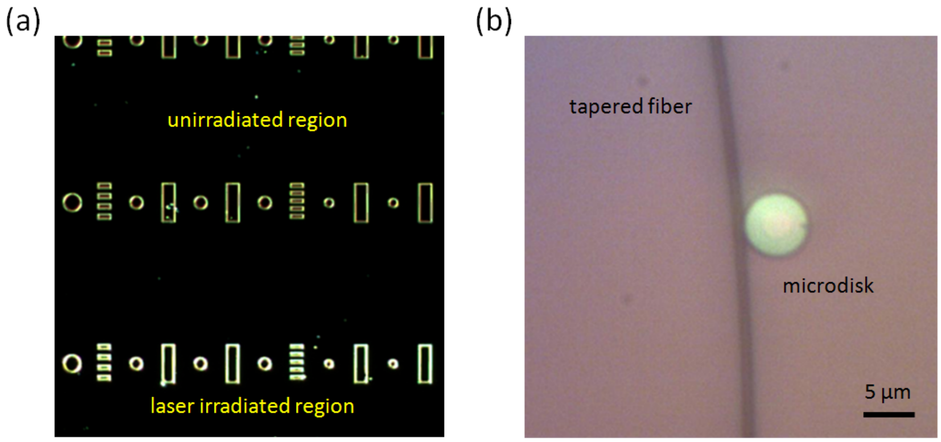

Figure 6.4: (a) Dark-field optical microscope image of excimer irradiated ($\sim$ 300 mJ/cm^2) and unirradiated regions. The irradiated region is brighter, indicating increased light scattering and roughness. (b) Optical microscope image of tapered fiber to microdisk coupling for optical measurements.

melting times, the edges of the microdisk will completely migrate to the center and form a dome-like shape.

In addition to SEM analysis, optical measurements were used to characterize microdisk and microring devices after the excimer processing (Fig. 6.10). The data from these measurements did not show an improvement in the quality factors of these cavities. Microring structures as shown in Fig. 6.10 (a) and microdisk structures as shown in Fig. 6.4 were excimer laser irradiated. The energy densities used were slightly above melting threshold. Optical measurements of the microring quality factor, as shown in Fig. 6.10 (b), were taken. The Q-factor of the microdisk was measured using a tapered fiber as shown in Fig. 6.4 (b). In both cases, no conclusive improvement in the Q-factor after laser irradiation was observed. A dark-field optical microscope image containing both irradiated and unirradiated regions is shown in Fig 6.4. We observed that the laser irradiated regions would always be brighter than the unirradiated regions. The brightness is inidicative of increased light-scattering and hence increased roughness, contrary to our desired result.

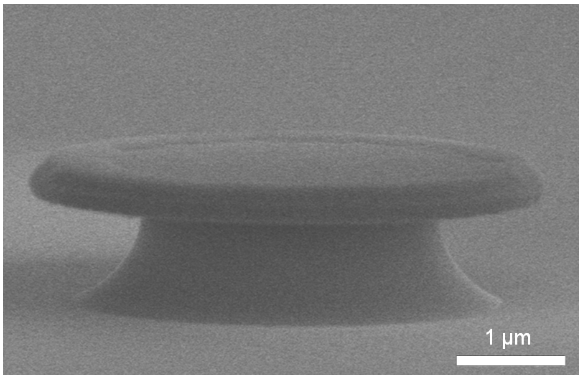

Figure 6.5: SEM image of silicon microdisk after excimer laser irradiation.

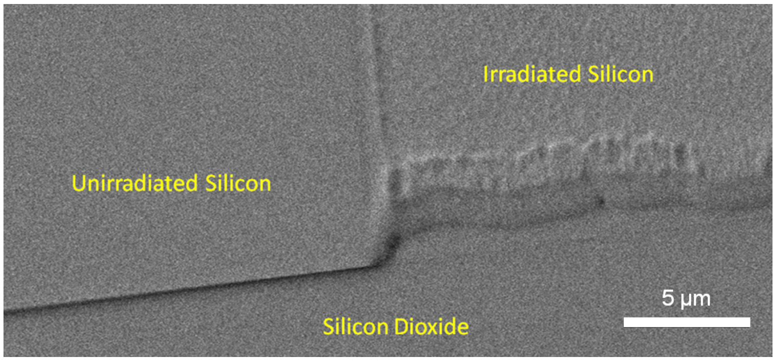

Figure 6.6: SEM image of edge of silicon edge region that has been half excimer laser irradiated (right) with an energy density of 1200 mJ/cm^2. The silicon is 250 nm thick. Note that in this case the oxide underneath has not been removed.

6.6 Analysis and Discussion

While Chou has demonstrated that small structures ($\sim$ 50-300 nm) can be made smoother using the excimer laser, our results indicate that larger structures do not improve in roughness. We observed an increase in both large-scale (micron-level) roughness as well as an increase in small-scale (nanometer-level) roughness.

Figure 6.6 shows a region of silicon on top of oxide that has been partially exposed to the excimer laser. The edge of the irradiated region flows inwards when melted. The edge is no longer straight but becomes wavy. The surface also becomes rippled. We attribute

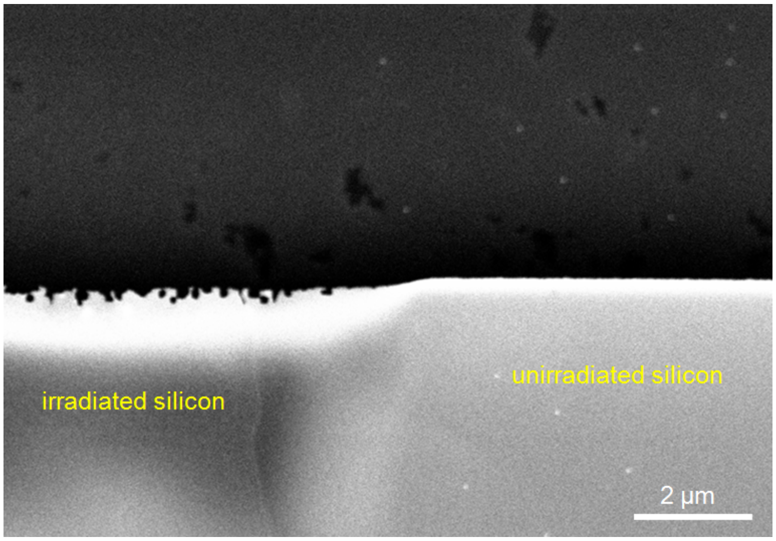

Figure 6.7: SEM image of edge of silicon edge region that has been half excimer laser irradiated (left) with an energy density of 240 mJ/cm^2. The silicon is 250 nm thick. The oxide underneath has been isotropically etched by several microns.

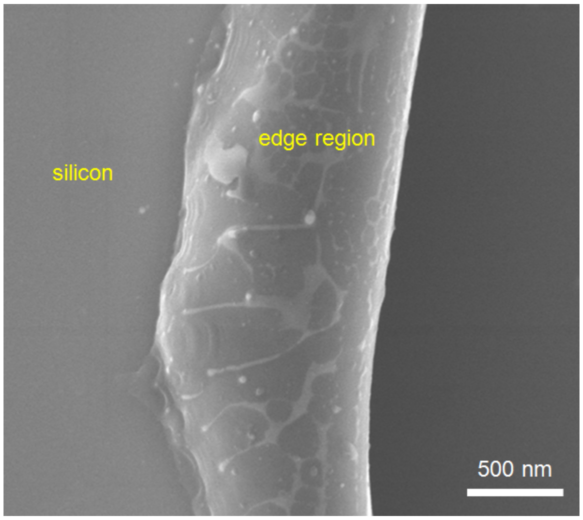

Figure 6.8: SEM image of undercut silicon edge region that has been excimer laser irradiated at an energy density of 370 mJ/cm^2.

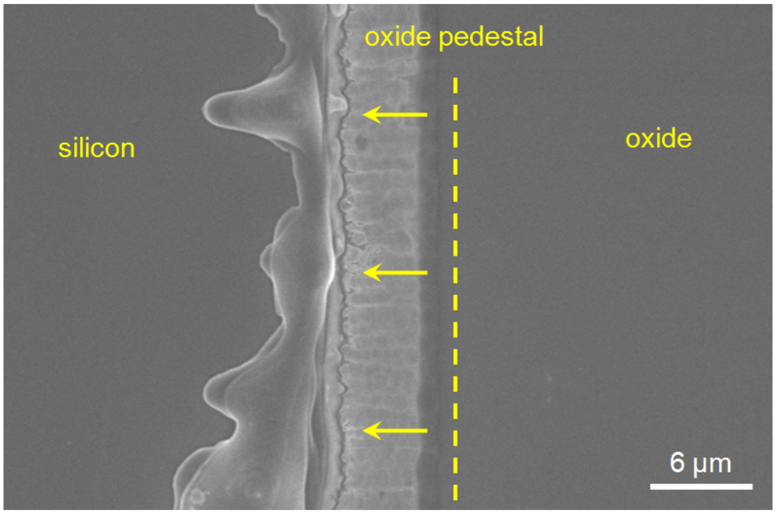

Figure 6.9: SEM image of undercut silicon edge region that has been excimer laser irradiated at an energy density of 460 mJ/cm^2.

these waves to the low viscosity of molten silicon [21] which makes it easy for the liquid to splash around when there is ambient vibration. The migration of the silicon interface inwards is due to the high surface tension of silicon. The surface tension of molten silicon can be expressed as $\gamma = 733 - 0.062(T - 1687)$, where γ is the surface tensions in (mN/m) and T is the temperature in K in a range from 1357-1890 K [22]. By comparison the surface tension of a polymer such as PMMA is $\sim$ 50 (mN/m). Surface energy minimization creates a strong internal pressure that pulls the liquid interface inwards. Additionally, this interface contraction might cause disturbances in the liquid silicon which result in the ripples in the solidified silicon. Solidification occurs over a period of less than $\sim$ 50 ns.

Another cause of increased roughness upon solidification could be due to the density difference between liquid and solid silicon. Similar to water, silicon is more dense as a liquid than as a solid and will expand as it freezes. If the the molten silicon solidifies from the inside outwards, a non-uniform solidification front can result in non-uniformities at the surface. Solidification driven extrusions have been observed during excimer laser irradiation of silicon nanopillars [23].

Figures 6.8, 6.7 and 6.9 show excimer irradiated structures that were originally straight edges. Prior to laser irradiation the oxide underneath the edge of these silicon structures had

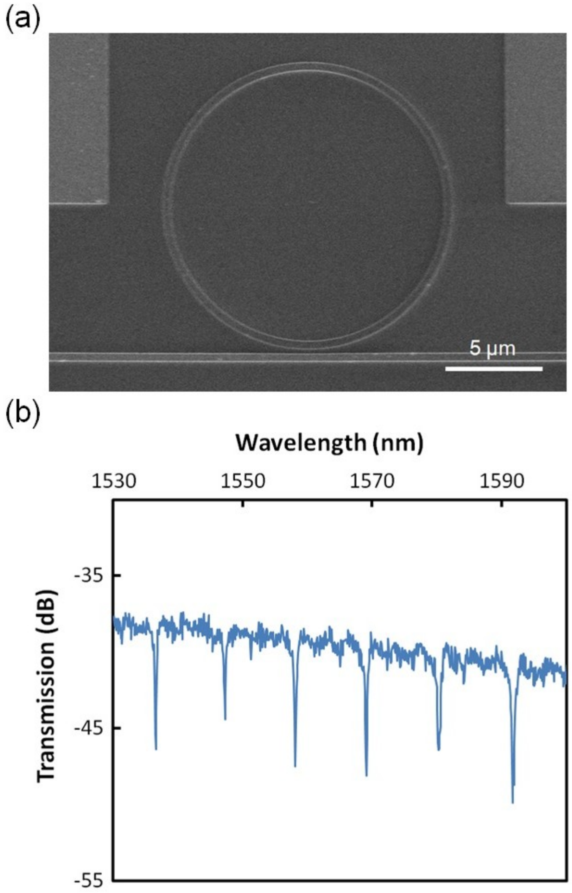

Figure 6.10: (a) SEM image of 15 μm diameter silicon microring on top of oxide. (b) Transmission measurements from 15 μm diameter silicon microring after excimer irradiation.

been etched by several microns using HF. In Fig. 6.8, the left-half of the silicon ledge shown has been exposed to a single excimer laser pulse with an energy density of 240 mJ/cm^2. This top-down SEM image shows a large increase in sidewall roughness. This is the result of the energy density being insufficient to completely melt the entire 250 nm thick ledge. The rough region is the silicon on the lower surface of the silicon ledge that has not been melted.

Higher energy irradiation with a single-shot energy density of 370 mJ/cm^2 is shown in 6.7. While the edge is now more rounded, it is also no longer straight along the vertical direction. In addition there appears to be some ablation of the silicon contributing to increased roughness. The SEM image in Fig. 6.9 is after an excimer shot of 460 mJ/cm^2. While the features are highly rounded, it can also be seen that the previously straight edge can no longer be maintained and is now unacceptably random. At higher energies silicon structures can reach an equilibrium shape which is also a function of the underlying oxide geometry. For small structures the equilibrium shape is often spherical. The surface roughness is not perfect, possibly due to ablation effects. Waveguides also have trouble maintaining their straight edges and will become wavy. At higher energies they will turn into discrete spheres.

6.7 Conclusions

Qualitative and quantitative improvements in sidewall roughness of silicon devices using excimer irradiation has not been shown. This can be attributed to a number of the material properties of the silicon, as well the thermal characteristics of the cavity designs. There may be ways to get around or take advantage of these limitations and here are some ideas. First, it appears that this technique is more suitable for applications requiring small spherical shapes (several microns or smaller) because they have reached an equilibrium shape. Second, a silicon microtoroid might be possible if a pedestal material is used which is more thermally-conductive than silicon. Third, in order to effect sidewall roughness, the chip might need to be mounted at an angle to the incident excimer beam in order to receive adequate exposure. Forth, the solidification period might be increased by high-temperature back-side heating of the silicon chip (hot plate) simultaneously with laser irradiation, hence allowing more time for features to smoothen out. But, this would need to be performed in an oxygen-free environment (such as a nitrogen chamber) in order to prevent silicon oxidation.

6.8 Acknowledgements

The excimer laser irradiation used in this study was performed in the laboratory of James Im. Yikang Deng, a graduate student in that group, provided much assistance both with

the laser as well as with the interpretation of the excimer melting results. Discussions also included James Im, Alexandar Limanov and Paul van der Wilt. The optical device measurements were conducted in the Optical Nanostructures Laboratory using a tapered fiber coupling test setup I had built in collaboration with Felice Geusuele, a postdoctoral researcher in our group. A lensed fiber coupling setup was also used for measurements on microring devices.

Part of the fabrication and SEM analysis was performed at the Center for Functional Nanomaterials (CFN) at Brookhaven National Laboratory where excellent training and assistance on the JEOL JBX-6300FS e-beam lithography system, cryogenic reactive ion etcher, and other fabrication tools was provided by Aaron Stein and Ming Lu. The fabrication facilities at CFN are top notch and the staff is even better. Fabrication was also performed at the Columbia University cleanroom. Yuan Zhang helped in the layout of a photomask for the contact aligner.

Bibliography

[1] S. Chang, N. B. Rex, R. K. Chang, G. Chong, and L. J. Guido, "Stimulated emission and lasing in whispering-gallery modes of GaN microdisk cavities," *Applied Physics Letters*, vol. 75, no. 2, pp. 166–168, 1999.

[2] L. Yang, T. Carmon, B. Min, S. M. Spillane, and K. J. Vahala, "Erbium-doped and Raman microlasers on a silicon chip fabricated by the sol–gel process," *Applied Physics Letters*, vol. 86, no. 9, p. 091114, 2005.

[3] R. D. Kekatpure and M. L. Brongersma, "Fundamental photophysics and optical loss processes in Si-nanocrystal-doped microdisk resonators," *Physical Review A*, vol. 78, p. 023829, Aug 2008.

[4] F. Vollmer, D. Braun, A. Libchaber, M. Khoshsima, I. Teraoka, and S. Arnold, "Protein detection by optical shift of a resonant microcavity," *Applied Physics Letters*, vol. 80, no. 21, pp. 4057–4059, 2002.

[5] A. M. Armani, R. P. Kulkarni, S. E. Fraser, R. C. Flagan, and K. J. Vahala, "Label-free, single-molecule detection with optical microcavities," *Science*, vol. 317, no. 5839, pp. 783–787, 2007.

[6] T. Grossmann, M. Hauser, T. Beck, C. Gohn-Kreuz, M. Karl, H. Kalt, C. Vannahme, and T. Mappes, "High-Q conical polymeric microcavities," *Applied Physics Letters*, vol. 96, no. 1, p. 013303, 2010.

[7] A. A. Savchenkov, A. B. Matsko, V. S. Ilchenko, and L. Maleki, "Optical resonators with ten million finesse," *Optics Express*, vol. 15, no. 11, pp. 6768–6773, 2007.

[8] J. Hu, N.-N. Feng, N. Carlie, L. Petit, A. Agarwal, K. Richardson, and L. Kimerling, "Optical loss reduction in high-index-contrast chalcogenide glass waveguides via thermal reflow," *Optics Express*, vol. 18, no. 2, pp. 1469–1478, 2010.

[9] C. Y. J. Ying, C. L. Sones, A. C. Peacock, F. Johann, E. Soergel, R. W. Eason, M. N. Zervas, and S. Mailis, "Ultra-smooth lithium niobate photonic micro-structures by surface tension reshaping," *Optics Express*, vol. 18, pp. 11508–11513, May 2010.

[10] J. Yao, D. Leuenberger, M.-C. Lee, and M. Wu, "Silicon microtoroidal resonators with integrated MEMS tunable coupler," *Selected Topics in Quantum Electronics, IEEE Journal of*, vol. 13, pp. 202 –208, March-April 2007.

[11] L. Yang, D. K. Armani, and K. J. Vahala, "Fiber-coupled erbium microlasers on a chip," *Applied Physics Letters*, vol. 83, no. 5, pp. 825–826, 2003.

[12] T. J. Kippenberg, S. M. Spillane, and K. J. Vahala, "Demonstration of ultra-high-Q small mode volume toroid microcavities on a chip," *Applied Physics Letters*, vol. 85, no. 25, pp. 6113–6115, 2004.

[13] M. Borselli, T. Johnson, and O. Painter, "Beyond the rayleigh scattering limit in high-Q silicon microdisks: theory and experiment," *Optics Express*, vol. 13, no. 5, pp. 1515–1530, 2005.

[14] S. Y. Chou and Q. Xia, "Improved nanofabrication through guided transient liquefaction," *Nature Nanotechnology*, vol. 3, no. 5, pp. 295–300, 2008.

[15] S. Y. Chou, C. Keimel, and J. Gu, "Ultrafast and direct imprint of nanostructures in silicon," *Nature*, vol. 417, no. 6891, pp. 835–837, 2002.

[16] M. Borselli, K. Srinivasan, P. E. Barclay, and O. Painter, "Rayleigh scattering, mode coupling, and optical loss in silicon microdisks," *Applied Physics Letters*, vol. 85, no. 17, pp. 3693–3695, 2004.

[17] N. Bloembergen, "Pulsed laser interaction with condensed matter," *Materials Research Society Symposium Proceedings*, vol. 51, pp. 3–13, 1985.

[18] V. Constantoudis, G. P. Patsis, A. Tserepi, and E. Gogolides, “Quantification of line-edge roughness of photoresists. ii. scaling and fractal analysis and the best roughness descriptors,” *Journal of Vacuum Science and Technology B: Microelectronics and Nanometer Structures*, vol. 21, no. 3, pp. 1019–1026, 2003.

[19] F. P. Payne and J. P. R. Lacey, “A theoretical analysis of scattering loss from planar optical waveguides,” *Optical and Quantum Electronics*, vol. 26, no. 10, pp. 977–986, 1994.

[20] D. K. Armani, T. J. Kippenberg, S. M. Spillane, and K. J. Vahala, “Ultra-high-Q toroid microcavity on a chip,” *Nature*, vol. 421, pp. 925–928, Feb. 2003.

[21] W.-K. Rhim and K. Ohsaka, “Thermophysical properties measurement of molten silicon by high-temperature electrostatic levitator: density, volume expansion, specific heat capacity, emissivity, surface tension and viscosity,” *Journal of Crystal Growth*, vol. 208, no. 1-4, pp. 313 – 321, 2000.

[22] H. Fujii, T. Matsumoto, S. Izutani, S. Kiguchi, and K. Nogi, “Surface tension of molten silicon measured by microgravity oscillating drop method and improved sessile drop method,” *Acta Materialia*, vol. 54, no. 5, pp. 1221 – 1225, 2006.

[23] D. Mills and K. W. Kolasinski, “Solidification driven extrusion of spikes during laser melting of silicon pillars,” *Nanotechnology*, vol. 17, no. 11, p. 2741, 2006.

Chapter 7

Z-scan of Lead Chalcogenide Nanocrystals

7.1 Properties of Nanocrystals

First studied in the early 1980s by Louis Brus at Bell Laboratories, nanocrystals (also known as nanoparticles and quantum dots) are nanoscale units of single-crystalline material. In colloidal form, nanocrystals have ligand shells and are generally dispersed in solvents such as chloroform and trichloroethylene. The ligand shells are composed of an organic surfactant such as oleic acid which prevents the nanocrystals from aggregating into larger particle units.

There has been much interest in nanocrystals because of their highly size-dependent properties. Improvements in synthesis techniques have led to the ability to create highly monodisperse solutions of nanocrystals. With the ability to finely tune nanocrystal properties, a host of different applications have appeared ranging from fluorescent markers in biology to nanocrystal displays for cell phones. Our interest in nanocrystals arises from the ability to tune to nonlinear properties to match the resonance of silicon photonic cavities.

A relationship between the polarization density (P) and electric field (ε) that contains the higher order nonlinear terms is:

$$P = \epsilon_0 \chi \varepsilon + 2d\varepsilon^2 + 4\chi^{(3)}\varepsilon^3 + \cdots \tag{7.1}$$

Where ϵ_0 is the permittivity of free space and χ is the electric susceptibility of the material. Because silicon is a centrosymmetric material, it does not possess the second order term in Eqn. 7.1. Silicon does possess third order nonlinearities, $\chi^(3)$. But these nonlinearities are quite weak in silicon. While our eventual goal was to incorporate the strong third order nonlinearities of chalcogenide nanocrystals onto silicon photonic devices, we first needed to characterized the magnitude of these nonlinearites in various nanocrystals.

Lead-chalcogenide semiconductor nanocrystals [1] have been suggested to possess large optical nonlinearities [2, 3, 4] with potential ultrafast response times at telecommunication wavelengths, making them technologically interesting materials. Nonresonant optical nonlinearities can have near-instantaneous response times but the magnitude of these nonlinearities are generally smaller than resonant nonlinearities. Resonant nonlinearities, which occur when the photon energy matches an optical transition, have slower response times due to the slow decay of excitons and free carriers but have susceptibilities scaling as $(a_B/R)^3$ where a_B is the exciton Bohr radius and R is the crystallite radius. [3] In the strong quantum-confinement limit (where $a_B/R \gg 1$), resonant nonlinearities can be very large due to the large density of states and spectral concentration of transition strength. [4] Narrow gap PbS and PbSe nanocrystals have some of the strongest confinement among semiconductor nanocrystals, with exciton Bohr radii of 20 nm and 46 nm, respectively, for crystallite diameters from 2 to 5 nm. This diameter range gives near-infrared emission such as used in single nanocrystal spectroscopy. [7, 5, 6] The intrinsic linewidth broadening affecting the transition strength is also reduced in lead chalcogenide nanocrystals due to the reduced exciton-phonon coupling and resulting near-identical electron and hole wavefunctions achieved in the strong confinement limit. [4]

7.2 Overview of Experiment

High-capacity optical networks and systems require dynamic switching functionalities such as add-drop filters, signal regeneration, and wavelength conversion in the near-infrared C-band. While these functionalities are currently performed through an optical-electronic-optical conversion, all-optical solutions can provide significant increases in capacity with low latencies, with potentially reduced cost, size and power requirements per bit. The design of such devices is embodied in a figure-of-merit[8] (FOM) where the Kerr nonlinearity is compared to a nonlinear absorption (typically two-photon absorption) for a given material at a specific wavelength. This FOM ($n_2/\beta\lambda$ where n_2 and β are the Kerr and two-photon absorption coefficients respectively) is found to be large in chalcogenides [9, 10, 11, 12, 13] at 1.55 μm. Specifically, studies on glasses containing chalcogenides at 1.55 μm have shown FOM greater than 3 and Kerr nonlinearities up to approximately 900 times that of fused silica.

Saturable absorption has been measured in glasses doped with PbS nanocrystals [14, 15] as well as in solutions of PbS nanocrystals. These results showed $\sim$ 5 to 50 ps resonant decay lifetimes[16]. In addition, third-order $\chi^{(3)}$ susceptibilities have been characterized at visible and $\sim$ 1.06 μm wavelengths in nanocrystal-doped nanocomposites;[17, 18, 19, 20] $\chi^{(3)}$

has also been studied recently for the case of colloidal PbSe nanocrystals. [21] However, a direct experimental comparison of nonlinearities for PbS and PbSe lead chalcogenide nanocrystals has not been investigated. In this work, we measure and compare the optical nonlinearities of both colloidal monodispersed PbS and PbSe nanocrystal solutions in the near-infrared. In addition, by using the femtosecond Z-scan technique, we examine the different activation mechanisms for thermal and Kerr nonlinearities in the resonant regimes of PbS and PbSe nanocrystals tuned to near-infrared wavelengths. Finally, we determine the spectrally-dispersive nonlinear refractive index (n_2) and nonlinear absorption (β) for the nanocrystals for wavelengths ranging from 1.0 to 1.6 μm. The electronic contributions for these two nonlinearities are shown to be greater than thermal contributions, thereby allowing their use for ultrafast optical signal processing in high-capacity optical networks and devices.

The highly monodisperse PbSe and PbS nanocrystals were synthesized in a solution-based wet chemical process to obtain a well-controlled size, less than 5% size distribution, and good surface passivation. The nanocrystals are synthesized by the Murray group. [22] The synthesis procedures for PbSe and PbS are similar. First, 2.16 g lead acetate trihydrate and 7.3 ml oleic acid were dissolved in 40 ml squalane for the PbSe nanocrystals. This mixture was heated to 100°C for 1.5 h under vacuum in order to form lead oleate and to drive off the solvent. Then, a lead oleate solution was heated to 178°C and 18 ml 1M solution of TOPSe in TOP was injected in the presence of vigorous stirring. The reaction mixture was kept at 155-160°C for 4-10 min and then promptly cooled to room temperature. The PbSe crude solution was mixed with hexane (1:1 by volume). The nanocrystals were precipitated by adding ethanol and collected by centrifugation. Precipitated nanocrystals were re-dissolved in hexane ($\sim$ 10 ml) and precipitated with ethanol. Finally, the nanocrystals were re-dispersed in chloroform. This method allowed nanocrystal size to be controlled by systematically adjusting the reaction conditions. [22] The properties of the prepared nanocrystals are listed in Table 1. Absorption spectra of nanocrystal solutions were measured using a UV/Vis/NIR spectrometer. Nanocrystal size was estimated by comparing absorption data to that in the literature [22] to be approximately 3.9 nm and 5.1 nm in diameter respectively. The linear absorption at the first exciton peak was approximately

Table 7.1: Properties of lead chalcogenide nanocrystals investigated.

Properties	**Units**	**PbSe**	**PbS**
Lattice constant (bulk)	Å	6.124	5.936
Bulk band gap	eV	0.26	0.37
Measured first exciton peak	nm	1399	1426
Crystallite diameter	nm	3.9	5.1
Est. exciton Bohr radius	nm	46	20
Bulk index at 1.5 μm		5.0	4.2
Concentration	mg/mL	18.8	4.5
Size distribution	%	< 5	< 5

20 cm^{-1} for both PbS and PbSe nanocrystal solutions. Concentrations were determined by measuring the mass of 100 μL of nanocrystal solution while boiling off the solvent in a thermogravimetric analyzer. These measurements included the mass of the ligands. Both PbSe and PbS were prepared to equal concentrations 52 ± 2 μM and had equivalent absorption peaks at 1410 ± 15 nm.

7.3 The Z-scan Technique

The Z-scan technique, developed by Mansoor Sheik-Bahae in 1989, is a way of measuring the nonlinear refractive index and nonlinear absorption coefficient. The technique is widely used and the orignal papers have received over 3000 citations [23, 24]. While the technique is relatively straight-forward for bulk materials, it can be more complicated for disperse colloidal materials. There are numerous subtle but important details that are sometimes overlooked in nanocrystal Z-scan literature. These details will be discussed below.

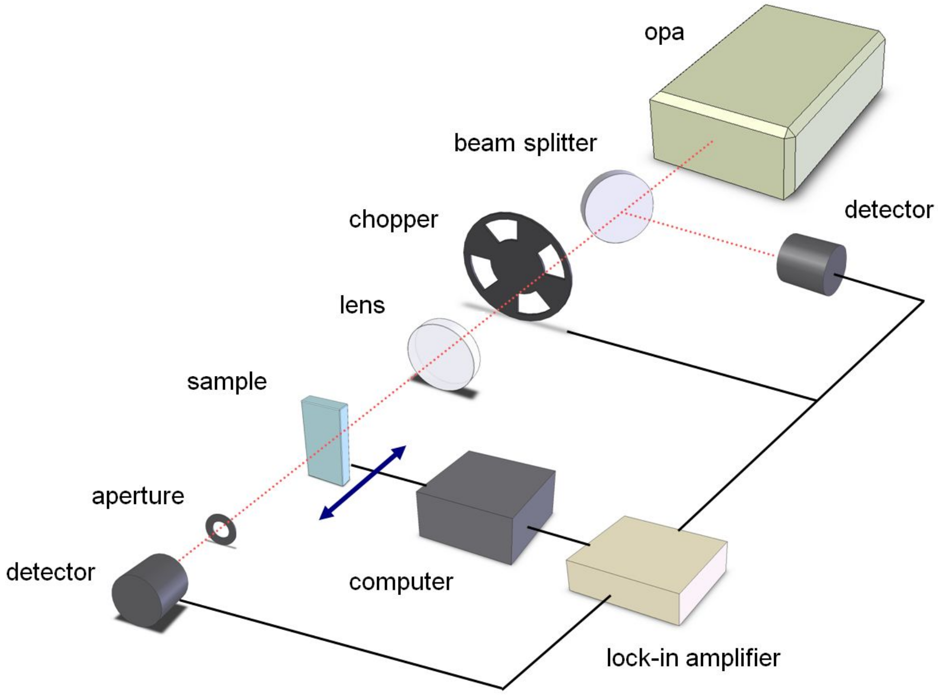

Figure 7.1: Diagram of the Z-scan test setup used in this experiment.

We used the Z-scan technique [23, 24] to determine nonlinear refractive index n_2 and nonlinear absorption β, which correspond to the real (refractive) and imaginary (absorptive) parts of the third-order susceptibility $\chi^{(3)}$. These dispersive measurements were performed from 1000 nm to 1600 nm wavelengths using a high sensitivity single-beam technique. [23] A cuvette containing the nanocrystal solution was moved along the z-axis through the focus of a beam. As the sample was brought towards the focus of the beam from the near-field, nonlinear self-lensing collimated the beam and resulted in increased transmittance through an aperture in the far field. As the sample traveled past the beam focus, self-defocusing resulted in beam divergence, which lowered the transmittance through the aperture. The resulting peak-to-valley self-defocusing transmittance profiles of typical Z-scans are shown in Fig. 7.2(a). Correspondingly, open aperture scans were used to determine the absorptive nonlinear properties (Fig. 7.2 (b)). In order to reduce noise in the collected data, a small portion of the incoming beam was split-off prior to the sample and used as a reference. The path length L of the cuvette was greater than the depth-of-focus z_o of the beam. With a L/z_o ratio of 2.5, we used the thick media analysis [25] for our measurements.

An optical parametric amplifier (OPA) pumped by a regeneratively amplified Ti:Sapphire laser was used to produce 100 fs pulses at a 250 kHz repetition rate at wavelengths ranging from 1.0 to 1.6 μm, corresponding to $\hbar\omega/E_g$ from 1.4 to 0.9, where E_g is the nanocrystal gap. The spectral width of the beam varied from 40 nm at 1550 nm to 20 nm at 1050 nm and the Gaussian beam radius at the focus ω_o was determined to be 10.8 μm using the knife-edge technique. Typical average powers of 2.5 mW and peak intensities of $\sim 2.6\times10^{10}$ W/cm^2 were used. Approximately 8% of the power was lost through Fresnel reflection from the front side of the cuvette. Neither beam-induced sample damage nor inhomogeneities across different positions in the cuvette were observed. Time-resolved photoluminescence was also used to determine the exciton radiative lifetime (T_1) of the $1S_e$-$1S_h$ transition for the chalcogenide nanocrystals, in the range of 900 ns, as shown in Fig. 7.2 (c).

7.4 Measurements

Figures 7.3 and 7.4 show the dispersive nonlinear refractive index measured for PbS and PbSe nanocrystals respectively, along the linear absorption superimposed. For both PbS and PbSe, the observed n_2 values follow the linear absorption closely. The maximum n_2 value for the PbSe and PbS nanocrystal solutions were of -3.4×10^{-14} cm^2/W and -1.5×10^{-14} cm^2/W, respectively. Hence, the n_2 of PbSe was measured to be approximately twice as large as that of PbS. This is because of the stronger quantum confinement in PbSe (with its larger exciton Bohr radius-to-crystallite radius ratio) while maintaining similar nanocrystal transition lifetimes. [4, 26] This measurement supports the feasibility of achieving larger $\chi^{(3)}$ susceptibility in PbSe nanocrystals. Although the measured nonlinear refractive index is observed to be of the same order as nonlinear bulk chalcogenide glasses ($\sim 6.0\times10^{-14}$ to 0.2×10^{-14} cm^2/W) [11] and bulk silicon ($\sim 4.5\times10^{-14}$ cm^2/W), [27, 28] the nonlinearity of the colloidal nanocrystal media scales considerably with concentration.

Nonlinear absorption was also observed for both nanocrystals through open aperture Z-scans. These measurements showed nonlinear absorption saturation in the range from 1200-1500 nm. The magnitude of n_2 and linear absorption curves for both nanocrystals followed a similar trend, reaching a value of approximately -8×10^{-11} cm^2/W near the first exciton peak. Due to the absorption saturation, two-photon absorption in this region was masked. Farther from the resonance, two-photon absorption was observed by Z-scans in the range of approximately 1000-1250 nm for the PbS nanocrystal with a resulting figure-of-merit of 2.3 at 1240 nm.

7.5 Thermal Effects

In Z-scan measurements it is important to ensure that thermal effects are not obscuring the results; we note that thermal lensing is negligible in our measurements. Thermal lensing occurs when a laser pulse creates temperature and density gradients in a solution, resulting in a refractive index variation that approximately follows the spatial beam profile. Absorption of heat from the laser pulse causes the solution to expand causing acoustic density changes. [29] These changes have a time scale of $t_{ad} = \omega_o/V_s$, where ω_o is the beam radius

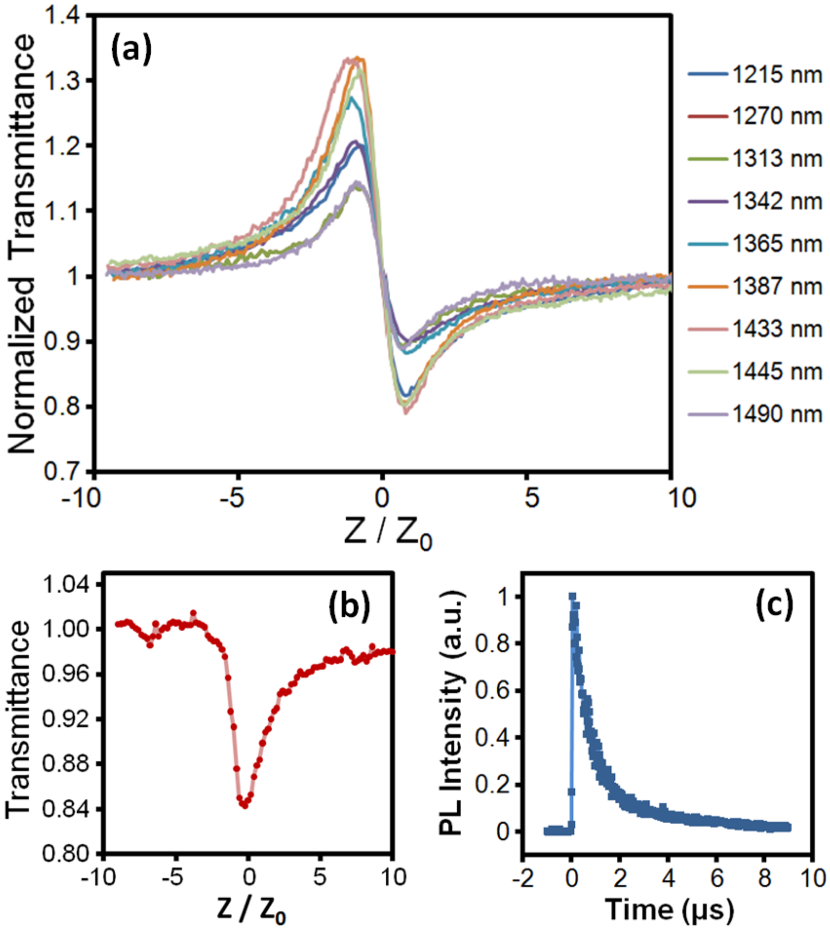

Figure 7.2: (a) Closed aperture Z-scans of colloidal PbS nanocrystal solution. (b) Open aperture z-scan of colloidal PbS nanocrystal solution at 1240 nm. (c) Time-resolved photoluminescence used to determine the $\sim$ 930 ns radiative lifetime (T_1) for the colloidal PbS nanocrystals.

and V_s is the speed of sound in chloroform at 979 m/s. For our experimental setup, t_{ad} = 10 ns which is much longer than our 100 fs pulse duration and therefore thermal lensing due to acoustic density changes can be ruled out. Another cause of thermal lensing is thermal accumulation. This will occur if heat generated from absorption does not diffuse away from the illuminated region at a fast enough rate so as to prevent a temperature rise. The time scale for thermal diffusion to occur is $t_D = \omega_0^2 /4D$, where ω_o is the beam radius and D is the thermal diffusivity of our host matrix ($D = 0.81\times10^{-7}$ m^2/s for chloroform [30]). Hence $t_D = 0.3$ ms for our system. Since our input pulses were chopped at 1 kHz with a 50% duty cycle, this gives an excitation window of 0.5 ms for the arrival of successive pulses. This time is longer than the thermal diffusion time scale t_D thereby preventing thermal accumulation. Notice that our pulse repetition rate of 250 kHz avoids thermal accumulation more readily than for the usual 82 MHz of most Ti:Sapphire lasers. [21] Thus in the experiment described in ref. 21 thermal nonlinearities may play a role in the measurement since the chopped excitation window period of 1.25 ms in that case is shorter than the 12 ms thermal diffusion time scale. Note also that our repetition rate is sufficient to show that an excited dot having a $\sim$ 930 ns lifetime will decay before a second pulse re-excites the dot, i.e. the repetition rate is slower than the $\sim$ 1 to 3 MHz exciton radiative lifetimes of the $1S_e$-$1S_h$ transition [31] thus allowing a ground state measurement of the nonlinearities.

In addition, the thermal contribution of the solution to the nonlinear index change, as heated by a single pulse, will exceed the electronic contribution of the nanocrystals if the pulse duration is greater than $n_2\rho_0 C/((dn/dT)\alpha)$ [32], where ρ_o and C are the material density and heat capacity per unit volume, dn/dT the thermo-optic coefficient, and α the linear absorption of the solution. For our setup, a pulse duration of greater than 10 ps is needed in order for thermal contributions to the refractive index change to be significant. Our 100 fs pulses are much shorter, hence the electronic contributions should exceed the thermal contributions.

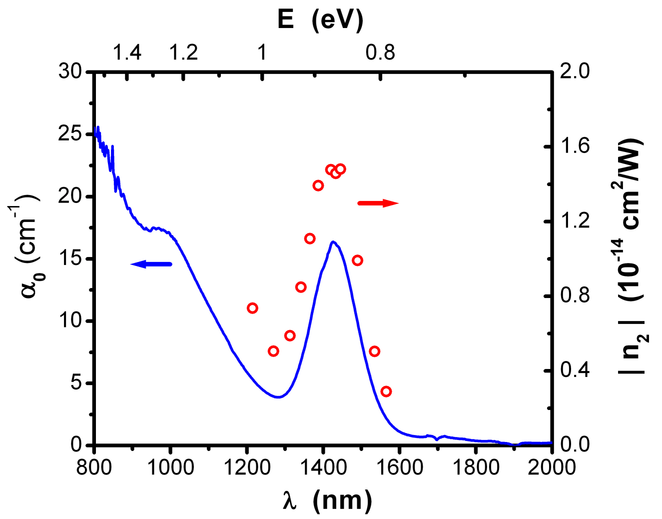

Figure 7.3: Measured linear absorption and nonlinear refractive indices for the colloidal PbS nanocrystals studied.

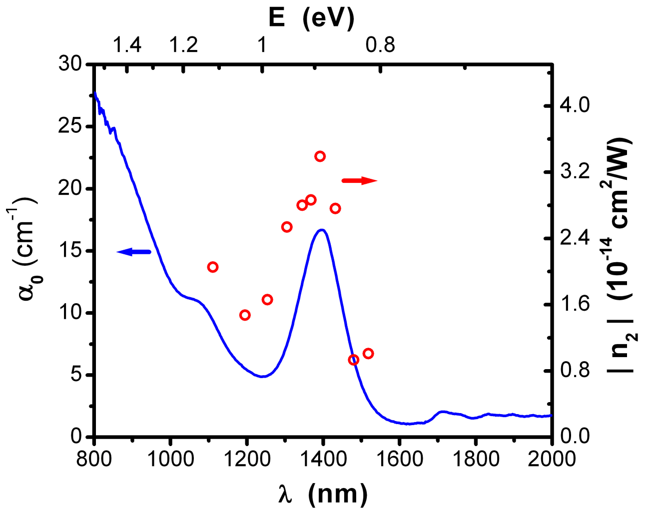

Figure 7.4: Measured linear absorption and nonlinear refractive indices for the colloidal PbSe nanocrystals studied.

7.6 Discussion

In the strong confinement regime, the mechanism responsible for Kerr nonlinearity is generally state-filling. [33] In this phenomena, photoexcitations result in the filling of energy levels thereby blocking further interband transitions since no two electrons can fill the same state (Pauli exclusion), thus saturating the absorption. The observed absorption saturation near the band edge for both kinds of nanocrystals would seem to indicate the role of state-filling. The effect, however, should be accompanied by a blue shift of the peak n_2 value. Our data does not show this blue-shift. Hence it is possible that the dominant mechanism for our observed nonlinearity is a mechanism such as free carriers. Free carrier nonlinearity is a fifth-order nonlinearity that becomes dominant over band-filling at higher intensities. [34]

7.7 Conclusions

In summary, we study and compare resonant optical nonlinearities in strongly quantum-confined PbSe and PbS nanocrystals. These nanocrystals have many interesting technological applications thus motivating this study. In addition, the size-tunable properties of nanocrystals makes them more versatile than bulk materials for optical applications. On resonance with the exciton peak, the nanocrystals show a strong saturable absorption and nonlinear refractive index that follows the linear absorption spectra. We attribute our observed optical nonlinearites to be more likely from free carriers instead of state-filling. Given the similarities in the measured n_2 of PbSe and PbS in the regime we studied, the more technologically practical nanocrystal would be PbSe due to its larger size which would offer more reliable tunability. In other regimes and other nonlinear mechanisms the comparison between PbSe and PbS could be very different. The ultrafast large nonlinearities, absorption saturation, and large off-resonance figure-of-merits observed in these near-infrared lead chalcogenide nanocrystals are promising for chip-scale ultrafast switching and all-optical signal processing.

7.8 Acknowledgements

The Z-scan experiment was performed using the Ti:Sapphire femtosecond laser in the laboratory of Prof. Osgood in the Electrical Engineering department. Jerry Dadap, a research scientist in Prof. Osgood's group, provided generous help with the project. The radiative lifetime measurements were taken by Ranojoy Bose, a member of our group. The lead chalcogenide nanocrystals were synthesized by Jeffrey Urban in Christopher Murray's group (Nanoscale Materials and Devices Group) at IBM Research in Yorktown Heights, New York. We also used nanocrystals from Evident Technologies of Troy, New York.

Bibliography

[1] V. I. Klimov, "Optical nonlinearities and ultrafast carrier dynamics in semiconductor nanocrystals", Journal of Physical Chemistry B **104,** 6112 (2000).

[2] L. Brus, "Quantum crystallites and nonlinear optics", Applied Physics A: Mater. Sci. and Process. **53,** 465 (1991).

[3] L. Banyai, Y. Z. Hu, M. Lindberg, and S. W. Koch, "Third-order optical nonlinearities in semiconductor microstructures", Phys. Rev. B **38,** 8142 (1988).

[4] F. W. Wise, "Lead salt quantum dots: the limit of strong quantum confinement", Accounts of Chemical Research **33,** 773 (2000).

[5] R. Bose, J. Gao, J. F. McMillan, A. D. Williams, and C. W. Wong, Optics Express **17**, 22474 (2009).

[6] M. T. Rakher, R. Bose, C. W. Wong, and K. Srinivasan, Optics Express **19**, 1786 (2011).

[7] R. Bose, X. Yang, R. Chatterjee, J. Gao, and C. W. Wong, "Weak coupling interactions of colloidal lead sulphide nanocrystals with silicon photonic crystal nanocavities near 1.55 μm at room temperature", Applied Physics Letters **90,** 111117 (2007).

[8] V. Mizrahi, K. W. DeLong, G. I. Stegeman, M. A. Saifi, and M. J. Andrejco, "Two-photon absorption as a limitation to all-optical switching", Optics Letters **14,** 1140 (1989).

[9] J. M. Harbold, F. O. Ilday, F. W. Wise, and B. G. Aitken, "Highly nonlinear Ge-As-Se and Ge-As-S-Se glasses for all-optical switching", IEEE Photonics Technology Letters **14,** 822 (2002).

[10] G. Lenz, J. Zimmermann, T. Katsufuji, M. E. Lines, H. Y. Hwang, S. Spälter, R. E. Slusher, S.-W. Cheong, J.S. Sanghera and I. D. Aggarwal, "Large Kerr effect in bulk Se-based chalcogenide glasses", Optics Letters **25,** 254 (2000).

[11] J. T. Gopinath, M. Soljačić, E. P. Ippen, V. N. Fuflyigin, W. A. King and M. Shurgalin, "Third order nonlinearities in Ge-As-Se-based glasses for telecommunications applications", Journal of Applied Physics **96,** 6931 (2004).

[12] C. Quemard, F. Smektala, V. Couderc, A. Barthelemy, and J. Lucas, "Chalcogenide glasses with high nonlinear optical properties for telecommunications", Journal of Physics and Chemistry of Solids **62,** 1435 (2001).

[13] T. Cardinal, "Non-linear optical properties of chalcogenide glasses in the system As-S-Se", Journal of Non-Crystalline Solids **256,** 353 (1999).

[14] K. Wundke, S. Pötting, J. Auxier, A. Schülzgen, N. Peyghambarian, and N. F. Borrelli, "PbS quantum-dot-doped glasses for ultrashort-pulse generation", Applied Physics Letters **76,** 10 (2000).

[15] A. Martucci, J. Fick, J. Schell, G. Battaglin, and M. Guglielmi, "Microstructural and nonlinear optical properties of silica-titania sol-gel film doped with PbS quantum dots", Journal of Applied Physics **86,** 79 (1999).

[16] F. Yoshino, A. A. Major, L. Levina, and E. M. Sargent, "Nonlinear refractive properties in lead sulfide (PbS) nanocrystals from 1200 to 1550 nm", presented at the International Quantum Electronics Conference, San Francisco, CA (2004).

[17] S. W. Lu, U. Sohling, M. Mennig, and H. Schmidt, "Nonlinear optical properties of lead sulfide nanocrystals in polymeric coatings", Nanotechnology **13,** 669 (2002).

[18] H. P. Li, B. Liu, C. H. Kam, Y. L. Lam, W. X. Que, L. M. Gan, C. H. Chew, and G. Q. Xu, "Femtosecond Z-scan investigation of nonlinear refraction in surface modified PbS nanoparticles", Optical Materials **14,** 321 (2000).

[19] B. Liu, H. Li, C. H. Chew, W. Que, Y. L. Lam, C. H. Kam, L. M. Gan, and G. Q. Xu, "PbS-polymer nanocomposite with third-order nonlinear optical response in femtosecond regime", Materials Letters **51,** 461 (2001).

[20] B. Yu, C. Zhu, H. Xia, H. Chen, and F. Gan, "Optical non-linearities of PbSe microcrystallites doped in glass", Materials Science Letters **16,** 2001 (1997).

[21] I. Moreels, Z. Hens, P. Kockaert, J. Loicq, and D. Van Thourhout, "Spectroscopy of the nonlinear refractive index of colloidal PbSe nanocrystals", Applied Physics Letters **89,** 193106 (2006).

[22] C. B. Murray, S. Sun, W. Gaschler, H. Doyle, T. A. Betley, and C. R. Kagan, "Colloidal synthesis of nanocrystals and nanocrystal superlattices", IBM Journal of Research and Development **45,** 47 (2001).

[23] M. Sheik-bahae, A. A. Said, and E. W. V. Stryland, "High-sensitivity, single-beam n_2 measurements", Optics Letters **14,** 955 (1989).

[24] M. Sheik-Bahae, A. A. Said, T. Wei, D. J. Hagan, and E. W. van Stryland, "Sensitive measurement of optical nonlinearities using a single beam", IEEE Journal of Quantum Electron. **26,** 760 (1990).

[25] E. W. V. Stryland and M. Sheik-Bahae, "Z-Scan Measurements of Optical Nonlinearities in Characterization Techniques and Tabulations for Organic Nonlinear Materials", M. G. Kuzyk and C. W. Dirk, Eds. (Marcel Dekker, Inc., 1998).

[26] Y. V. Vandyshev, V. S. Dneprovskii, and V. I. Klimov, Soviet Physics JETP **74,** 144 (1992).

[27] M. Dinu, F. Quochi, and H. Garcia, "Third-order nonlinearities in silicon at telecom wavelengths", Applied Physics Letters **82,** 2954 (2003).

[28] J. F. McMillan, M. Yu, D. -L.Kwong, and C. W. Wong, Optics Express **18,** 15484 (2010).

[29] J. N. Hayes, "Thermal blooming of laser beams in fluids", Applied Optics **11,** 455 (1972).

[30] H. Cabrera, A. Marcano, and Y. Castellanos, Condensed Matter Physics **9,** 385 (2006).

[31] R. Bose, J. F. McMillan, J. Gao, C. J. Chen, D. V. Talapin, C. B. Murray, K. M. Rickey, and C. W. Wong, Nano Lett. **8,** 2006 (2008).

[32] R. W. Boyd, Nonlinear Optics (Academic Press, San Diego, CA, 2003).

[33] Y. Li, M. Ohata, S. Sasaki, and A. Nakamura, "Size-Dependent Enhancement of Third-order Optical Nonlinearity in $\mathrm{CuBr}_x\mathrm{Cl}_{1-x}$ Nanocrystals Embedded in Glass", Japanese Journal of Applied Physics **37,** L33 (1998).

[34] S. Y. Auyang and P. A. Wolff, "Free-carrier-induced third-order optical nonlinearities in semiconductors", Journal of the Optical Society of America B **6,** 595 (1989).

[35] G. Aleksejenko, V. Pačebutas, and A. Krotkus, "Optical nonlinearities in PbSe nanocrystals", presented at the 12th International Symposium UFPS, Vilnius, Lithuania (2004).

[36] I. L. Bolotin, D. J. Asunskis, A. M. Jawaid, Y. Liu, P. T. Snee, and L. Hanley, "Effects of surface chemistry on nonlinear absorption, scattering, and refraction of PbSe and PbS nanocrystals", Journal of Physical Chemistry C **114,** 16257 (2010).

Chapter 8

Conclusions

In this thesis we have investigated fabrication-related solutions to key issues in advancing the field of silicon photonics from the laboratory to commercial applications. While this work focused primarily on fabrication issues, we note that more fabrication-tolerant device designs will also play a major role in future advancements.

We proposed and investigated two different techniques for precisely tuning the resonance of high-Q/V$_m$ silicon photonic crystal nanocavities. One was a global technique for tuning an entire wafer while the other was a highly localized technique for tuning individual nanocavities. The atomic layer deposition technique allows for deposition hafnium oxide thin films with monolayer control and hence resonance tuning in discrete redshifted steps of 122±18 pm. Nearly linear tuning was demonstrated over a 17 nm tuning range. The cavity had an initial Q of $>$ 49,000 which was fairly well maintained during the tuning. The local oxidation technique was applied to ultra-high Q photonic crystal heterostructures. Unlike the highly linear ALD technique, this tuning technique blueshifted the resonance according to the parabolic rate law associated with silicon oxidation. A tuning range of $\sim$ 10 nm was demonstrated. Initial Q values of $>$ 300,000 were fairly well maintained. In these nanoscale studies we discovered tuning anomalies that occur during the initial tuning. These are attributed to interfacial layers, surface chemistry and other material related phenomena.

In addition to nanocavities, these techniques can be applied to other structures such as waveguides. We investigated the use of atomic layer deposition for tuning the slow-light regime in silicon photonic-crystal waveguides. Here we show that the high group-index regime can be deterministically controlled, redshifted by 140±10 pm per atomic layer, without affecting the group-velocity dispersion and third-order dispersion.

Another important issue in the practical realization of silicon photonics is improving the sidewall roughness of devices. Here we investigated two different techniques: hydrogen annealing and excimer laser-assisted melting. While our hydrogen annealing studies were limited by equipment issues, some valuable insights were discovered. The presence of thermal stress related crystallographic defects such as dislocations may be the cause of the poor performance of hydrogen annealed silicon photonic devices. Excimer laser irradiation was investigated as a way to improve the performance of devices such as microdisks and microrings.

The final chapter discusses our investigations into the nonlinear properties of colloidal lead chalcogenide nanocrystals in the near-infrared spectrum with the intention of incorporating these materials into silicon photonic devices. A number of other investigations were also pursued but not discussed in this thesis due to the nature of the projects and the relevance of the results to this thesis.

Appendices

Appendix A

A.1 List of Publications

(1) C. J. Chen*, J. Zheng*, T. Gu, J. F. McMillan, M. Yu, G.-Q. Lo, D.-L. Kwong, C. W. Wong, Selective Tuning of Silicon Photonic Crystal Cavities via Laser-Assisted Local Oxidation, [*equal contribution; submitted to journal]

(2) C. J. Chen, J. I. Dadap Jr., R. M. Osgood Jr., C.W. Wong, Third-order optical nonlinearities in colloidal lead chalcogenide nanocrystals in the near-infrared, [submitted to journal]

(3) C. J. Chen, C. A. Husko, I. Meric, K. L. Shepard, C. W. Wong, W. M. J. Green, Y. A. Vlasov, and S. Assefa, Deterministic tuning of slow-light in photonic crystal waveguides through the C and L bands by atomic layer deposition, Appl. Phys. Lett. 96, 081107 (2010).

(4) C. J. Chen*, X. Yang*, C. A. Husko, and C. W. Wong, Digital resonance tuning of high-Q/Vm silicon photonic crystal nanocavities by atomic layer deposition, Appl. Phys. Lett. 91, 161114 (2007)[*equal contribution: arxiv:cond-mat.mtrl-sci/0707.2412]

(5) J. Gao, P. Heider, C. J. Chen, X. Yang, C. A. Husko, and C. W. Wong, Observations of whispering gallery modes in asymmetric optical resonators with rational caustics, Appl. Phys. Lett. 91, 181101 (2007); also at: arxiv:physics.optics/0707.2552

(6) R. Bose, J. F. McMillan, J. Gao, C. J. Chen, D. V. Talapin, C. B. Murray, K. M.

Rickey, and C. W. Wong, Temperature-tuning of near-infrared (1.5-um) monodisperse quantum dot solids toward controllable Frster energy transfer, Nano Lett. 8, 2006 (2008).

(7) O. Cherniavskaya, C. J. Chen, E. Heller, E. Sun, J. Provezano, L. Kam, J. Hone, M. P. Sheetz, S. J. Wind, Fabrication and surface chemistry of nanoscale bioarrays designed for the study of cytoskeletal protein binding interactions and their effect on cell motility, J. Vac. Sci. Technol. B 23(6), 2972, Nov 2005.

A.2 List of Conferences

(1) C. J. Chen*, J. Zheng*, J. F. McMillan, M. Yu, G.-Q. Lo, D.-L. Kwong, C. W. Wong, Selective Tuning of Silicon Photonic Crystal Cavities via Laser-Assisted Local Oxidation, Conference on Lasers and Electro-Optics, Baltimore, Maryland, May 2011. [*equal contribution; submitted to CLEO 2011]

(2) C. J. Chen, C. Husko, I. Meric, K. Shepard, C. W. Wong, W. M. J. Green, Yurii A. Vlasov, and S. Assefa, Digital Deterministic Control of Slow Light in Photonic Crystal Waveguide Membranes through Atomic Layer Deposition, Conference on Lasers and Electro-Optics, Baltimore, Maryland, June 2009.

(3) C. J. Chen*, X. Yang*, C. Husko, C. W. Wong, Digital Resonance Tuning of High-Q/Vm Silicon Photonic Crystal Nanocavities by Atomic Layer Deposition, Conference on Lasers and Electro-Optics, San Jose, California, May 2008. [*equal contribution]

(4) C. J. Chen, J. I. Dadap Jr., J. Urban, C. B. Murray, R. M. Osgood Jr., C.W. Wong, Observation of Optical Nonlinearites in Strongly Quantum Confined PbSe Nanocrystals for All-Optical Tunable Nanophotonics, Optics East Conference, Boston, Massachusetts, October 2006.

(5) C. W. Wong, R. Chatterjee, J. Gao, C. J. Chen, J. F. McMillan, X. Yang, R. Bose, and Y.-F. Xiao, Coherent interactions in photonic crystal nanostructures: controlling dispersion and efforts towards quantum information processing, European Materials Research Society Spring 2008 meeting, Strasbourg, France, May 2008 (invited)

(6) C. W. Wong, C. A. Husko, J. F. McMillan. X. Yang, C. J. Chen, R. Bose, and J. Gao, Nonlinearities and non-classical emission in photonic band gap nanostructures, in Proceedings of SIAM Conference on Nonlinear Waves and Coherent Structures, Seattle, Washington, 2006 (invited).

(7) C. W. Wong, R. Chatterjee, K. Liu, C. J. Chen, and C. A. Husko, Negative refraction and nonlinearities in photonic band gap nanostructures, in SPIE Proceedings of Optics and Photonics: Nanophotonics (NP208), San Diego, California, 2006 (invited).